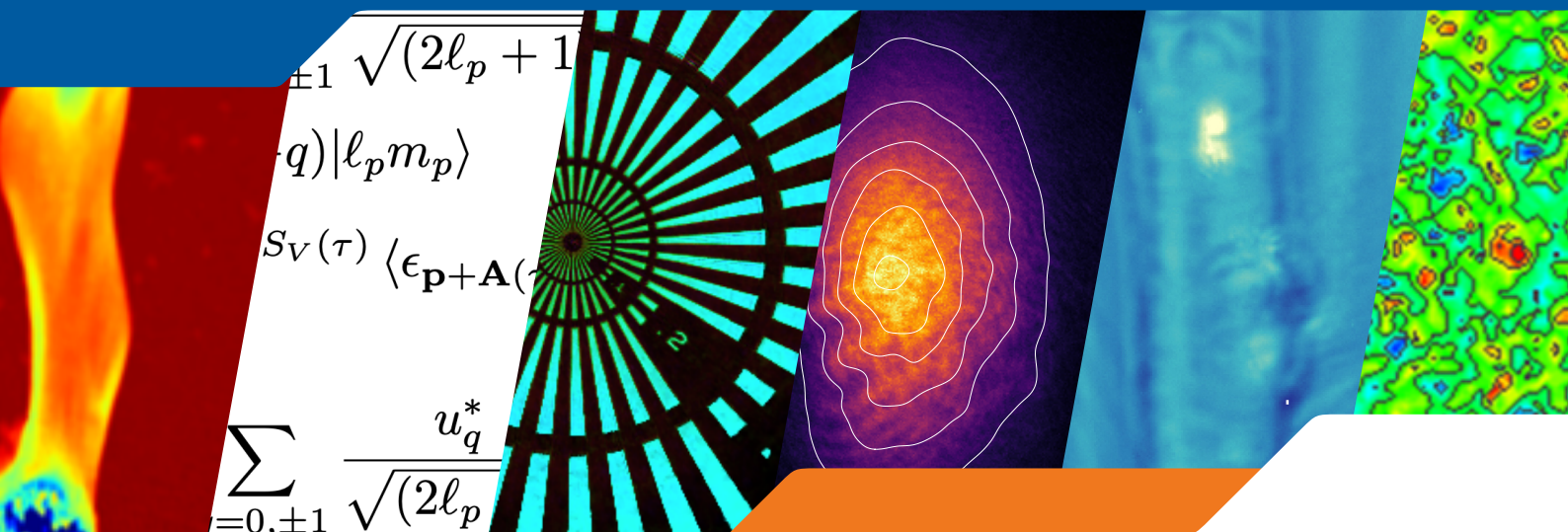


HI JENA

Helmholtz Institute Jena

ANNUAL REPORT 2022



FRIEDRICH-SCHILLER-
UNIVERSITÄT
JENA

HZDR
HELMHOLTZ ZENTRUM
DRESDEN ROSENDORF



HELMHOLTZ INSTITUTE JENA

ANNUAL REPORT 2022

IMPRINT

Publisher: Helmholtz-Institut Jena, Fröbelstieg 3, 07743 Jena, Germany
(<http://www.hi-jena.de>)
@ GSI Helmholtzzentrum für Schwerionenforschung GmbH
Darmstadt, Germany (<http://www.gsi.de>)
GSI is member of the Helmholtz association of national research
centers (<http://www.helmholtz.de>).

Editors: Daniel Seipt and Arno Klenke

DOI: <http://dx.doi.org/10.15120/GSI-2023-00687>

Publication date: August 2023

The Annual Report 2022 of the Helmholtz-Institut Jena is licensed under the Creative Commons Attribution BY 4.0 (CC BY 4.0): <https://creativecommons.org/licenses/by/4.0/>

CONTENTS

FOREWORD	10
Promotion of young researchers at the Helmholtz Institute Jena <i>R. Martin, C. Hahn, G. Weber</i>	13
HIGH POWER LASER DEVELOPMENT	14
Active Stretcher System for the POLARIS Upgrade <i>M. Hornung, G.A. Becker, M. Hellwing, J. Hein, M.B. Schwab, F. Schorcht, and M.C. Kaluza</i>	15
POLARIS Upgrade and Connection to Target Area Fraunhofer <i>M. Hornung, G.A. Becker, M. Hellwing, J. Hein, M.B. Schwab, F. Schorcht, and M.C. Kaluza</i>	16
Laser Beam Control by Intense Ultrasound Waves in Ambient Air <i>Y. Schrödel, C. M. Heyl, and the SOPHIMA consortium</i>	17
Nonlinear post compression at 515 nm and 2 μm wavelength in gas filled multi-pass cells for nonlinear frequency conversion experiments <i>M. Karst, P. Gierschkey, P. Pfaller, C. Grebing, R. Klas, Z. Wang, T. Heuermann, M. Lenski, J. Buldt, M. Müller, M. Gebhardt, J. Rothhardt, and J. Limpert</i>	18
Continuously tunable high photon flux high harmonic source <i>R. Klas, A. Kirsche, M. Gebhardt, L. Eisenbach, W. Eschen, J. Buldt, H. Stark, J. Rothhardt, and J. Limpert</i>	19
A new target chamber for the TAF target area <i>P. Hilz, T. Köhler, M. C. Kaluza, and M. Zepf</i>	20
A common control system for JETi200 and POLARIS at HI Jena <i>D. Hollatz, P. Hilz, A. Kessler, C. Lee, and M. Zepf</i>	21

HELIPORT Progress Report for 2022	
<i>C.-L. Lee and A. Kessler</i>	22
Helmholtz Laser-Plasma Metadata Initiative (HELPMI)	
<i>A. Kessler, M. Kaluza, H. P. Schlenvoigt, F. Pöschel, A. Debus, V. Bagnoud, U. Eisenbart, and J. Hornung</i>	23
LASER PARTICLE ACCELERATION	24
Highly efficient proton acceleration from solid and pre-expanded thin foils	
<i>I. Salaheldin, M. Shi, P. Hitz, A. Sävert, G. Schafer, and M. Zepf</i>	25
Observation of relativistic postsolitons	
<i>A. Sävert, C. Zepter, M. C. Kaluza, and M. Zepf</i>	26
LWFA-Electron Dependence on Pulse Front Tilt	
<i>C. Zepter, A. Seidel, A. Sävert, M. Zepf, and M. C. Kaluza</i>	27
Laser-plasma experiments with microdroplet targets	
<i>G. A. Becker, M. Nolte, M. Beyer, M. B. Schwab, D. Klöpfel, M. Hornung, M. Hellwing, F. Schorcht, and M. C. Kaluza</i>	28
Probing Ultrafast Laser-Induced Solid-to-Overdense Plasma Transitions	
<i>Y. Azamoum, G. A. Becker, S. Keppler, G. Duchateau, S. Skupin, M. Grech, F. Catoire, I. Tamer, M. Hornung, M. Hellwing, A. Kessler, F. Schorcht, and M. C. Kaluza</i>	29
Shadowgraphy of the plasma evolution around water micro-droplets irradiated by high-power laser pulses	
<i>M. Beyer, Y. Azamoum, M. Nolte, G. A. Becker, M. B. Schwab, M. Hornung, M. Hellwing, and M.C. Kaluza</i>	30
Monoenergetic Electron Beams from Controlled Injection in a Multi-Stage Gas Cell	
<i>A. Seidel, Z. Yu, C. Zepter, A. Sävert, D. Seipt, and M. Zepf</i>	31
All-Optical Transverse Emittance Characterization of Laser-Plasma Accelerated Electron Beams	
<i>F. C. Salgado, A. Kozan, D. Hollatz, A. Seidel, G. Schäfer, A. Sävert, D. Ullmann, Y. Zhao, M. Kaluza, and M. Zepf</i>	32
Simulating the Effect of Asymmetric Laser Wakefield Generated by Shock- front Rotation on Betatron X-rays	
<i>H. Harsh, D. Seipt, and M. Zepf</i>	33

PHOTON AND PARTICLE SPECTROSCOPY 34

Full 3-dimensional characterization of laser pulses with orbital angular momentum	
<i>X. Huang, A. Sävert, G. Schäfer, B. Heinemann, and M. Zepf</i>	35
Enhanced Ghost Imaging by Illumination Pattern Optimization	
<i>T. Tian, Z. Sun, S. Oh, and C. Spielmann</i>	36
Single pixel imaging using Hadamard and Fourier pattern	
<i>S. Oh, T. Tian, and C. Spielmann</i>	37
Long Living Hot and Dense Plasma by Intense Laser-Nanowire Interaction	
<i>E. Eftekhari-Zadeh, P. Tavana, R. Loetzsch, I. Uschmann, T. Siefke, T. Käsebier, U. Zeitner, A. Szeghalmi, A. Pukhov, O. Rosmej, D. Kartashov, and C. Spielmann</i>	38
Ellipticity Dependence of High Harmonic Generation in MoS₂ Monolayer	
<i>H. N. Gopalakrishna, R. Hollinger, V. Korolev, A. George, M. Zürich, C. Spielmann, A. Turchanian, and D. Kartashov</i>	39
Revealing the ultra-structure of microorganisms using table-top extreme ultraviolet ptychography	
<i>C. Liu, W. Eschen, J. Limpert, and J. Rothhardt</i>	40
Table-top Nanoscale Material-specific Imaging at 13.5 nm Wavelength	
<i>W. Eschen, C. Liu, D. Molina Penagos, R. Klas, J. Limpert, and J. Rothhardt</i> .	41
Platform for combined heavy-ion high-energy-laser experiments	
<i>Zs. Major, P. Hesselbach, P. Neumayer, B. Zielbauer, X. Yu, K. Weyrich, A. Tauschwitz, D. Varentsov, V. Bagnoud, R. Belikov, B. Winkler, J. Lütgert, D. Kraus, and D. Riley</i>	42
Scanning high-sensitive x-ray polarization microscopy	
<i>B. Marx-Glowna, B. Grabiger, R. Löttsch, I. Uschmann, A.T. Schmitt, K.S. Schulze, A. Last, T. Roth, S. Antipov, H.P. Schlenvoigt, I. Sergeev, O. Leupold, R. Röhlberger, and G.G. Paulus</i>	43
A Novel Compton Telescope for Polarization Measurements up to 1 MeV	
<i>W. Middents, G. Weber, U. Spillmann, T. Krings, and Th. Stöhlker</i>	44
High Resolution X-Ray Studies of Fe Using a Micro-Calorimeter Detector	
<i>M. O. Herdrich, D. Hengstler, A. Fleischmann, C. Enss, T. Morgenroth, S. Trotsenko, G. Weber, R. Schuch, and Th. Stöhlker</i>	45

Simulation of the photopeak efficiency of microcalorimeters equipped with small-volume gold absorbers <i>G. Weber, P. Pfäfflein, F. Kröger, M. O. Herdrich, D. Hengstler, A. Fleischmann, and Th. Stöhlker</i>	46
Improvements in background reduction of metallic magnetic calorimeter data by means of a coincidence scheme <i>Ph. Pfäfflein, M. O. Herdrich, G. Weber, and Th. Stöhlker</i>	47
High-Resolution Microcalorimeter Measurement of N, M \rightarrow L transitions in U⁹⁰⁺ at CRYRING@ESR <i>F.M. Kröger, S. Allgeier, Z. Andelkovic, S. Bernitt, A. Borovik, L. Duval, A. Fleischmann, O. Forstner, M. Friedrich, J. Glorius, A. Gumberidze, Ch. Hahn, F. Herfurth, D. Hengstler, M.O. Herdrich, P.-M. Hillenbrand, A. Kalinin, M. Kiffer, T. Köhler, M. Kubullek, P. Kuntz, M. Lestinsky, B. Löher, E.B. Menz, T. Over, N. Petridis, Ph. Pfäfflein, S. Ringleb, R.S. Sidhu, U. Spillmann, S. Trotsenko, A. Warczak, G. Weber, B. Zhu, C. Enss, and Th. Stöhlker</i>	48
New Regimes of Nuclear Resonance Excitation: First Experiments at the European XFEL <i>R. Röhlsberger</i>	49
Mössbauer Spectroscopic Imaging of Magnetic Domains <i>M. Kobayashi, K. Hayakawa, Y. Ishida, Y. Yoshida, and R. Röhlsberger</i>	50
Ion storage with the new HILITE Penning ion trap <i>S. Ringleb, M. Kiffer, G.G. Paulus, W. Quint, Th. Stöhlker, and M. Vogel</i>	51
Preparation of eutectic alloys for liquid metal ion sources and laser-induced dissociation dynamics of the gold molecular ion <i>F. Machalett, B. Ying, B. Wan, M. Kübel, A. Sommerfeld, S. Lippmann, A. M. Saylor, Th. Stöhlker, and G. G. Paulus</i>	52
Real-Time Observation of Temperature-Induced Nanofaceting on Sapphire Surfaces <i>D. J. Erb, J. Perlich, S. V. Roth, R. Röhlsberger, and K. Schlage</i>	53
Progress Report of the Negative Ions Laser Photodetachment Project <i>O. Forstner, V. Gadelshin, K. Stiebing, and K. Wendt</i>	54
THEORY	56
Optimally chirped laser pulses for increased narrowband photon yield from Inverse Compton Scattering sources <i>M. A. Valialshchikov and D. Seipt</i>	57

Calculations of multipole transitions in Sn II for kilonova analysis <i>A.I. Bondarev, J. H. Gillanders, C. Cheung, M. S. Safronova, and S. Fritzsche</i>	58
Radiative recombination of highly-charged ions with polarized electrons <i>A.V. Maiorova, S. Fritzsche, A. Surzhykov, and Th. Stöhlker</i>	59
Generalized description of the spatio-temporal biphoton state in spontaneous parametric down-conversion <i>B. Baghdasaryan, F. Steinlechner, and S. Fritzsche</i>	60
Analytic formula of the critical intensity for high-order harmonic generation <i>B. Minneker and S. Fritzsche</i>	61
Nondipole strong-field approximation for above threshold ionization in few-cycle pulse <i>D.F. Dar, B. Minneker, and S. Fritzsche</i>	62
Partial-wave representation of the strong-field approximation — length versus velocity gauge <i>F. Liu and S. Fritzsche</i>	63
Accurate molecular ab initio calculations in support of strong-field attosecond physics experiments <i>G. Visentin, B. Ying, G. G. Paulus, and S. Fritzsche</i>	64
Spatiotemporal dynamics of positron-hydrogen scattering in one dimension <i>L. G. Jiao, X. H. Ji, and S. Fritzsche</i>	65
QED approach to valence-hole excitation in closed shell systems <i>R. N. Soguel, A. V. Volotka, and S. Fritzsche</i>	66
Detecting the oscillating magnetic field using the vector twisted light atom interaction <i>S. Ramakrishna, R. P. Schmidt, A. A. Peshkov, A. Surzhykov, and S. Fritzsche</i>	67
p-Wave resonances in exponential cosine screened Coulomb potential <i>Y. C. Wang, L. G. Jiao, and S. Fritzsche</i>	68
Novel signatures of radiation reaction in electron–laser side scattering <i>P. Sikorski and D. Seipt</i>	69
Linear polarization and angular distribution of the Lyman-α_1 line following electron-impact excitation of H-like ions <i>Z. W. Wu, Z. M. He, C. Z. Dong, and S. Fritzsche</i>	70

Improvement of the Locally Constant Field Approximation	
<i>N. Larin and D. Seipt</i>	71
All-optical quantum vacuum signals in two-beam collisions	
<i>H. Gies, F. Karbstein, and L. Klar</i>	72
Direct accessibility of the fundamental constants governing light-by-light scattering	
<i>F. Karbstein, D. Ullmann, E. A. Mosman, and M. Zepf</i>	73
Large N external-field quantum electrodynamics	
<i>F. Karbstein</i>	74
Quantum vacuum processes in the extremely intense light of relativistic plasma mirror sources	
<i>A. Sainte-Marie, L. Fedeli, Neïl Zaïm, F. Karbstein, and H. Vincenti</i>	75
Pauli-Term-Induced Fixed Points in d-dimensional QED	
<i>H. Gies, K. K. K. Tam, and J. Ziebell</i>	76
PUBLICATIONS	77
THESES	90

FOREWORD

Dear friends and members of the Helmholtz Institute Jena,

Since its inception, the Helmholtz Institute has been combining the established scientific expertise of the University and our partners with the strategic mission of GSI. Embedded into the Faculty of Physics and Astronomy of the Friedrich Schiller University Jena, the focus of research at HI Jena is on fundamental and applied research at the borderline of strong-field physics, relativistic light-matter interactions, and fundamental quantum processes.

Despite emerging cost increases due to spiraling energy prices and growing inflation, the year 2022 marks an upswing and milestone, overshadowed by the consequences and suffering from the terrible war in Ukraine. In these politically deeply affected times, research at the Helmholtz Institute has progressed actively during the past year with many ongoing and advanced experiments, as documented by the current annual report.



Figure 1: *On November 3rd, the new research building of the Helmholtz Institute Jena was ceremonially opened after a construction phase of almost 2.5 years. Following a welcome address by Professor Paolo Giubellino, Scientific Managing Director of GSI and FAIR, greetings were delivered during the ceremony by representatives of the State of Thuringia, State Secretary Dr. Katja Böhler for the Thuringia Ministry for Economy, Science and Digital Society, and State Secretary Professor Barbara Schöning for the Thuringia Ministry for Infrastructure and Agriculture, as well as by Ministerialdirigent Dr. Volkmar Dietz for the Federal Ministry of Education and Research. President Professor Walter Rosenthal spoke on behalf of Friedrich Schiller University, and the Helmholtz Association was represented by its President Professor Otmar Wiestler. Professor Thomas Stöhlker, Director of the Helmholtz Institute Jena, gave a closing speech thanking the guests for their celebratory words and their support for the new research building.*

In 2022, a particular highlight was the ceremonial opening of the new research building after a construction phase of 2.5 years and an investment of €8.9 million for the cost of the construction,

fully financed by state funds from the Thuringian Ministry of Infrastructure and Agriculture. The new four-story building provides around 550 square meters of additional floor space including offices and a seminar room on the two top floors, while on the two lower floors mostly research laboratories as well as building technology and supply services are located. The building was constructed on Fraunhofer Street, near the existing institute building on the campus of Friedrich Schiller University, allowing the basement to be connected to the already existing target laboratory. With it, the institute has received a new eye-catching feature during the past year. With its clear structure and large panorama windows, the building forms a striking yet pleasing key-stone to the campus just below the Landgrafen. Last year did not only see the outer white cuboid grow, but also the laboratory setups gaining shape, thanks to the generous support from the local government of Thuringia.

The institute's research infrastructure, which has been additionally improved by the new building, is a guarantee for the cutting-edge research that will take place at the Helmholtz Institute in the future, building on the successful track record since the institute's founding in 2009. Recognition for this research success has resulted in several prizes in late 2022. These include a "Carl Zeiss Foundation Wild Card Grant" awarded to Dr. Christoph Heyl for research into contactless light manipulation using ultrasonic waves in gases, a "Hugo Geiger Award for Young Scientists" awarded to Dr. Robert Klas for his work on the development of compact high-power EUV sources, and the FAIR-GSI Ph.D. Award granted to Johannes Hornung for his outstanding Ph.D. thesis "Study of Preplasma Properties Using Time-Resolved Reflection Spectroscopy". While Dr. Christoph Heyl has established a successful young investigator group at DESY, Robert Klas and Johannes Hornung are recent graduates of the institute's graduate school "Research School of Advanced Photon Science" (RS-APS). Moreover, we are very happy to acknowledge that Dr. Peter Micke has successfully applied for a Helmholtz Young Investigator Group. He will add another facet to the research portfolio of the Institute, namely research in the realm of novel quantum technologies. In 2023, Dr. Micke will start his work on "Quantum Logic Spectroscopy for Frequency Metrology of Heavy and Simple Ions" with a focus on heavy ions at the highest charge states at rest as provided by the trapping facility HITRAP at GSI.

HI Jena also takes an active role in the technology transfer as part of the consortium initiative Digital Innovation Hub Photonics (DIHP). Innovations and business ideas in optics and photonics are selected each year at an "Elevator Pitch" and supported by a research budget for further development. As an example, in 2022 Dr. Günter Weber (HI Jena), Dr. Uwe Spillmann (GSI) and Wilko Middents (HI Jena) received one of the grants for the CompCam project, where they will conduct a feasibility analysis of novel Compton X-ray imaging.

The institute is particularly committed to the education and promotion of young scientists working at the Helmholtz Institute and its associated Helmholtz Centers. The graduate school has been an integral part of the Helmholtz Institute for more than ten years and successfully aims to promote and support young scientists during their Ph.D. studies. Together with its partner school HGS-HIRe for FAIR, a good number of dedicated courses and soft skills series have been offered to early-career scientists through virtual workshop series. In 2022 more than half of the 55 participants supported by RS-APS came from abroad, which indicates the growing internationalization of the research school. Approximately 50% of the Ph.D. students actively involved in RS-APS are 3rd party financed. Due to the influence of the pandemic, a smaller number of students successfully finished their Ph.D. in the past year (five students in total), but we expect a significantly increased number of graduations for the upcoming year 2023.

Being hosted at the campus of the Friedrich Schiller University, the stimulating contact with the research groups from the university as well as from the Helmholtz partner centers becomes prominent in many common activities, not least with the two high-power laser systems POLARIS and JETi200. With this annual report of the Helmholtz Institute Jena for 2022, we wish to give glimpses and insights into the ongoing research projects of the institute.

Enjoy reading.

Promotion of young researchers at the Helmholtz Institute Jena

R. Martin^{*1}, C. Hahn¹, and G. Weber¹

¹Helmholtz Institute Jena, Fröbelstieg 3, 07743 Jena, Germany

One main mission of the Helmholtz Institute Jena is the support and promotion of young researchers. Since the foundation of the Research School of Advanced Photon Science (RS-APS) in 2012 the HI Jena has also its own institution to meet this objective adequately.

RS-APS, which supports the PhD projects of young researchers working at the Helmholtz Institute Jena and its associated Helmholtz Centers, maintains a steady membership of about 50 to 60 PhD students, of which 5 completed their doctoral projects in 2022. Compared to previous years



Figure 1: Students of RS-APS presenting a hands-on model of a particle accelerator at the exhibition “Lange Nacht der Wissenschaft”.

this is a slight downturn in graduations, following the disruptions caused by the COVID-19 pandemic. We therefore expect a significant increase of doctoral students finishing their theses in the upcoming year.

Moreover, the end of the contact restrictions led to a catch-up effect of events, workshops and conferences for the HI Jena science community which also hampered due to the lack of possible time slots the organization of a Lecture Week by RS-APS. An example is the event “Lange Nacht der Wissenschaft”, which took place in Jena in November 2022. This event holds a long tradition and involves many actors from science and industry who open their doors to the general audience and try to fascinate the guests with exciting aspects of their research and development activities. The Helmholtz Institute Jena participated with several exhibitions stands, that were mainly managed by RS-APS students. To be more specific, our students explained to the visitors the principles of a particle cloud chamber and the working scheme of a LINAC accelerator structure in a playful manner (see Figure 1).

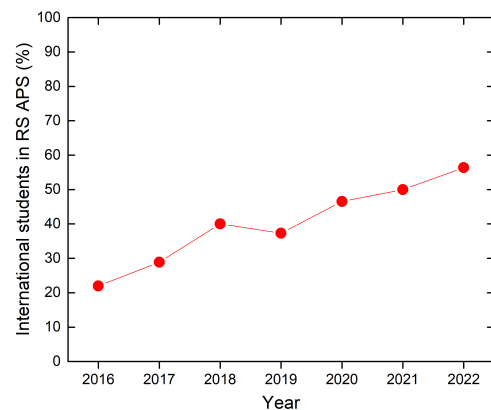


Figure 2: Development of the percentage of international students in the Research School of Advanced Photon Science.

Moreover, in this report we would like to point out the continuous progress of the internationalization of our research school. In the year 2022 the percentage of international students for the first time jumped above 50 % (see Figure 2). Out of 55 PhD students that were supported by RS-APS, 31 students came from abroad (from 16 countries). Considering that the total number of students is stable, this underlines the research school’s focus on internationalization to attract young science talents from all over the world.

^{*}r.maertin@hi-jena.gsi.de

HIGH POWER LASER DEVELOPMENT

Active Stretcher System for the POLARIS Upgrade

M. Hornung^{*1,2}, G.A. Becker², M. Hellwing², J. Hein², M.B. Schwab², F. Schorcht¹, and M.C. Kaluza^{1,2}

¹Helmholtz Institute Jena, Fröbelstieg 3, 07743 Jena, Germany; ²Institute of Optics and Quantum Electronics, Max-Wien Platz 1, 07743 Jena

We report a reconfiguration of POLARIS's active stretcher system to prepare the operation with the currently planned laser upgrade. The stretcher-compressor system's angle of incidence on the diffraction gratings is changed from 60.7° to 54°. Furthermore, enhanced spectral shaping capabilities are installed into the laser chain.

With the recently inaugurated extension building of the HI Jena our novel joint target area Fraunhofer will be equipped and prepared for high-intensity experiments with JETi200 and POLARIS laser pulses. For the connection of the POLARIS laser system a significant change in the pulse compressor's vacuum system is required. Furthermore, a transport beamline with a switchyard to change between the individual target areas has to be designed and installed. Due to optical and geometrical issues it was decided to change the compressor's and hence also the stretcher's angle of incidence from 60.7° [1] to 54°. With this modification the full aperture of the compressed laser pulses could be enlarged from 140 mm to 190 mm while keeping partially the existing pulse compression gratings with a line density of 1480 l/mm. The new construction of the pulse compressor including the required vacuum chambers is described in another contribution of this year's annual report.

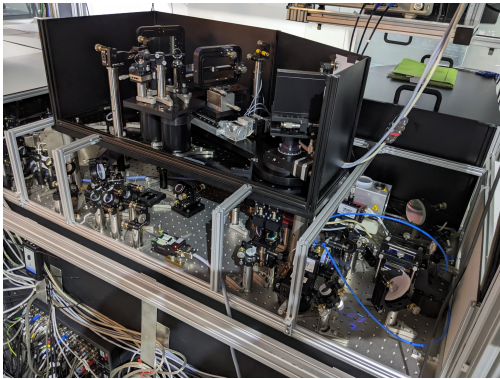


Figure 1: Photography of the active stretcher

In order to fit the spectral dispersion of the pulse compressor with a grating distance of 5.75 m and an angle of incidence on the gratings of 54° we had to reconfigure the active stretcher system [2] which was used as a test bed so far. A photograph of the active stretcher is shown in Figure 1. As far as the main pulse compressor will only be available in the future we have to setup two pulse com-

pressors for test purposes during the commissioning of the active stretcher in 54°-configuration. The first compressor is a 10 mm aperture picosecond compressor to recompress an active stretcher single-pass stretched pulse from 70 ps to the desired sub-100 fs pulse duration. The second is a 1.8 m grating separation compressor to recompress multi-pass stretched pulses from 1.5 ns to sub-100 fs pulse duration. These two compressors are required to investigate and optimize the performance of the active stretcher in different operation modes before the installation of the new vacuum pulse compressor.

Furthermore, we have installed a high-dynamic range DAZZLER HR45-1030 with a maximum programmable delay of 14 ps and a spectral resolution of 0.3 nm in combination with a WIZZLER spectral phase measurement device [3]. Using these devices in feedback operation we were able to recompress the single-pass stretched laser pulses from 70 ps to a transform limited pulse duration of 77 fs (FWHM) as shown in Figure 2. This measurement was still carried out with the 60.7° angle of incidence and indicates the spectral shaping capabilities and the very high temporal quality of the stretched and compressed pulses.

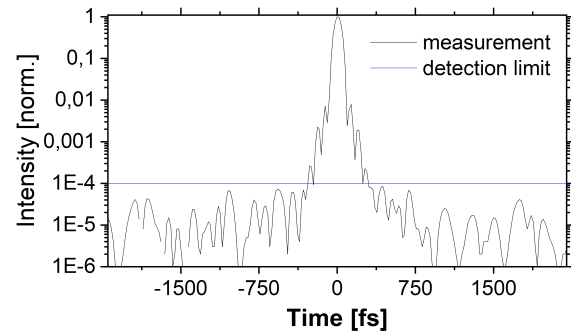


Figure 2: High dynamic range pulse duration measurement of a 77 fs (FWHM) laser pulse.

The finalization of the the stretching and compression of nanosecond pulses with ultra-high temporal contrast in preparation for the major POLARIS upgrade is currently subject of ongoing work.

References

- [1] M. Hornung, Appl. Phys. B **101**, 93-102 (2010).
- [2] M. Hornung, HI Jena annual report, p. 16 (2018).
- [3] <https://fastlite.com/>.

^{*}marco.hornung@uni-jena.de

POLARIS Upgrade and Connection to Target Area Fraunhofer

M. Hornung^{*1,2}, G.A. Becker², M. Hellwing², J. Hein², M.B. Schwab², F. Schorcht¹, and M.C. Kaluza^{1,2}

¹Helmholtz Institute Jena, Fröbelstieg 3, 07743 Jena, Germany; ²Institute of Optics and Quantum Electronics, Max-Wien Platz 1, 07743 Jena

We report on the status of the POLARIS laser upgrade and the plan to connect the laser system to the recently inaugurated extension building of HI Jena. For the newly available target area in the extension building a vacuum beam transport system needs to be designed and installed. In the course of this modification the pulse compressor and some components of the POLARIS laser will be upgraded too.

The output power and the peak intensity of POLARIS are currently limited by the 140 mm circular free aperture of the tiled-grating pulse compressor [1]. A maximum pulse energy of 16.7 J and a peak power of 170 TW could be applied in experiments. On the other hand, the final amplifier A5 already showed pulse amplification of laser pulses up to 54 J [2].

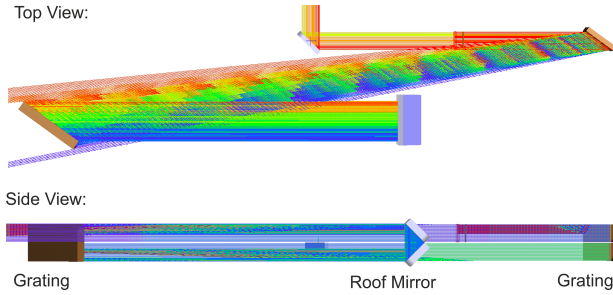


Figure 1: Schematic layout of the Treacy-type pulse compressor with a 54° angle of incidence. Different colours are representing different spectral components of the laser pulse.

In order to use the full potential of POLARIS in experiments, an upgrade of the pulse compressor is currently in preparation. The installation and final assembly of this upgrade will be installed with the required beam transport system to the new target area in the extension building of HI Jena.

A schematic layout of the novel pulse compressor is shown in Fig. 1. In comparison to the existing pulse compressor the angle of incidence on the diffraction gratings will be changed from 60.7° to 54°. The grating separation distance remains unchanged with a value of 5.75 m between the diffraction gratings. As gratings we will use 2 of the existing gold coated gratings with a line density of 1480 lines/mm and one recently delivered gold grating with an area of 700 x 390 mm². The 2 existing gratings with a size of 350 x 190 mm² will serve as the first and last grating

and the new grating will be used for the second and third pass replacing the formerly used tiled grating. With the use of a monolithic grating instead of a tiled grating we will significantly enhance the stability of the compressed laser pulses.

In addition to the optical setup, a significantly enlarged vacuum system is required to support the novel compressor setup. The vacuum system has to support the pulse compressor as well as a switchyard system to send the laser pulses either to the existing POLARIS target area or the new target area Fraunhofer. This vacuum system is currently under construction where two vacuum chambers for turning mirrors have already been ordered and are now being manufactured. The two-existing meter-sized POLARIS compression chambers will be reused as a switchyard and a grating support chamber. One large vacuum chamber (4.5 x 1.5 x 1 m³) is furthermore required for the roof mirror and the 700 mm grating. A sketch of this chamber, which is currently in its design phase, is depicted in Fig. 2.

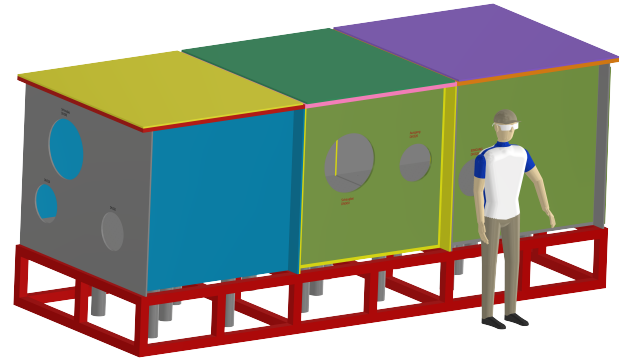


Figure 2: Schematic view of the designed pulse compression chamber (4.5 x 1.5 x 1 m³).

The finalization of the the stretching and compression of nanosecond pulses with ultra-high temporal contrast in preparation for the major POLARIS upgrade is currently subject of ongoing work.

References

- [1] M. Hornung, Appl. Phys. B **101**, 93-102 (2010).
- [2] M. Hornung, Opt. Lett., Vol 41 **22**, 5413-5416 (2016).

^{*}marco.hornung@uni-jena.de

Laser Beam Control by Intense Ultrasound Waves in Ambient Air

Y. Schrödel^{1,2,3}, C. M. Heyl^{1,2,3}, and the SOPHIMA consortium^{1,2,3,4,5}

¹HI Jena, 07743 Jena, Germany; ²GSI Helmholtzzentrum für Schwerionenforschung GmbH, 64291 Darmstadt, Germany; ³Deutsches Elektronen-Synchrotron DESY, 22607 Hamburg, Germany; ⁴Measurement and Sensor Technology, Technische Universität Darmstadt, 64283 Darmstadt, Germany; ⁵Hochschule Aalen, 73430 Aalen, Germany

Controlling coherent light is essential in various scientific fields. Modern laser optics, however, frequently demands parameter regimes where either the wavelength or the optical power restricts control schemes based on the interaction with solid media. We circumvent these constraints using high-intensity ultrasound waves in ambient air to control light. We demonstrate this approach by acousto-optic (AO) modulation (AOM) of ultrashort laser pulses, entirely omitting transmissive solid media, surpassing the peak power limit of current AOM technology by three orders of magnitude.

Optical methods used to shape, guide, and modulate laser light rely almost entirely on the interaction of light with solid media. However, many cutting edge applications employ parameters where either absorption, e.g., in the ultraviolet and infrared spectral regions, or nonlinear optical effects as well as light-induced damage limit this interaction. While the material-dependent refractive index limits applicable wavelength and peak power, the material's internal structure limits the average power of the light it can interact with.

To overcome these constraints, we employ gaseous media, e.g., ambient air [1]. For gases, and in particular noble gases like He, the transmissive windows are considerably wider: They extend both into the ultraviolet down to 50 nm and below 1 nm, corresponding to photon energies above 1 keV, as well as into the near- and mid-infrared. In addition, gases are effectively immune to damage and support peak powers about three orders of magnitude higher than bulk-based AO media.

We overcome the usually weak [2] AO interaction in

gases by employing a high ultrasound pressure in combination with a reflector enabling an enhanced acoustic field. In addition, we increase the interaction length by employing a multi-pass geometry for the optical beam. In this way, the laser beam (which is propagating under a shallow angle relative to the sound field wave fronts) undergoes efficient Bragg-diffraction [3], and after sufficient propagation, it is partially deflected (Fig. 1A).

In our experiments, this method enables relative deflection efficiency of up to 52 % at high peak power (20 GW) while preserving excellent spatial beam properties (Fig. 1B–D). Numerical simulations indicate much higher deflection efficiency upon reaching higher sound pressures.

Our experimental demonstration sets a promising basis for gas-based laser beam steering, splitting and combining as well as ultrafast switching and phase modulation. Prospectively, we expect that similar techniques will enable translation of other light control schemes such as lenses or waveguides to the gas phase, promising new opportunities e.g., for high-power, ultrafast and nonlinear optics.

Funding: DESY Generator program, Claus-Tschira-Boost Foundation and Carl-Zeiss Stiftung. We acknowledge DESY and HI Jena, members of the Helmholtz Association HGF for support and/or the provision of exp. facilities.

References

- [1] Y. Schrödel *et al.*, preprint arXiv:2304.06579 (2023).
- [2] W. Dürr *et al.*, Int. J. Infrared Millim. Waves **7** (1986).
- [3] P. Phariseau, Proc. Indian Acad. Sci. – Sec. A **44** (1956).

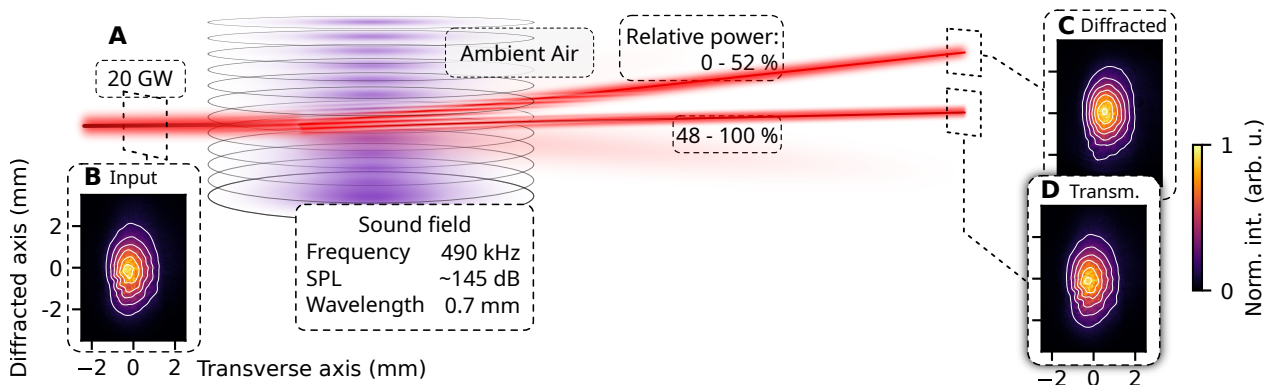


Figure 1: **A** Schematic of acousto-optic modulation in ambient air. A near-infrared laser beam (measured beam profile displayed in **B**) enters a sound field in air, deflecting up to 52 % of the optical power into the first diffraction order. **C** shows the beam profile of the diffracted, **D** of the transmitted beam. Multi-pass geometry not shown.

Nonlinear post compression at 515 nm and 2 μm wavelength in gas filled multipass cells for nonlinear frequency conversion experiments

M. Karst^{*1,2}, P. Gierschke^{†2,3}, P. Pfaller², C. Grebing³, R. Klas^{1,2,3}, Z. Wang², T. Heuermann^{1,2}, M. Lenski², J. Buldt², M. Müller², M. Gebhardt^{1,2}, J. Rothhardt^{1,2,3}, and J. Limpert^{1,2,3}

¹HI Jena, Fröbelstieg 3, 07743 Jena, Germany; ²IAP, FSU Jena Albert-Einstein-Str. 15, 07745 Jena, Germany;

³Fraunhofer Institute for Applied Optics and Precision Engineering IOF, Albert-Einstein-Str. 7, 07745 Jena, Germany

We present the post compression of 515 nm wavelength second harmonic pulses of an Yb:fiber laser from 240 fs to 15.7 fs. Additionally, the output of an ultrafast Tm:fiber laser centered at 2 μm wavelength was post compressed from 138 fs to 35 fs. These sources render ideal platforms to drive efficient high harmonic generation into the XUV and soft X-ray region with excellent power scaling prospects.

Traditionally, waveguides like noble-gas filled capillaries have been utilized for nonlinear pulse post compression. While such systems are capable of producing few-cycle pulses in the millijoule range, their efficiency is fundamentally constrained by capillary propagation loss. In contrast, multipass cells (MPC) have recently gained attention as a viable alternative to fiber-based post-compression methods. MPCs offer several advantages, including high throughput efficiency, compact size, excellent beam quality preservation, and spatially homogenized spectral broadening.

Short driving wavelengths, such as those in the visible spectrum, can provide various benefits for consecutive nonlinear frequency conversion techniques. In particular, the highly efficient generation of coherent 46 nm radiation (26.5 eV) using High-Harmonic Generation (HHG) [1] This scheme has the potential to enable the first Watt-class HHG table-top source at around 30 eV. On the other hand, employing ultrafast short-wavelength infrared driving sources ranging from 1.4 μm to 3.0 μm , is a promising approach to generate coherent soft X-ray radiation (SXR) [2]. These high-energy photons in the so-called water window spectral region ($\approx 280 \text{ eV} - 530 \text{ eV}$) are highly relevant for high-resolution imaging and XUV-spectroscopy of biological specimens.

To generate ultrashort pulses ($< 20 \text{ fs}$) in the visible spectral range, the output of an ytterbium-based fiber laser system was frequency doubled in BBO crystal [3]. At a conversion efficiency of more than 52 % this allowed for 29 W of average power at 515 nm with a pulse energy of 0.58 mJ and duration of 240 fs. The pulses were spectrally broadened in a Herriott-type multipass cell enclosed in a 0.6 bar krypton atmosphere. Utilizing dispersive mirrors, the pulses were recompressed to a duration of 15.7 fs. Overall the presented scheme allowed for generation of pulses in green spectral range at 22 W of average power, corresponding to an efficiency $> 40 \%$ (IR to compressed green pulse). In a preliminary study we demonstrated the

generation of phase-matched high harmonic radiation up to 100 eV utilizing the sub-10 cycle pulses with close to 25 GW of peak power.

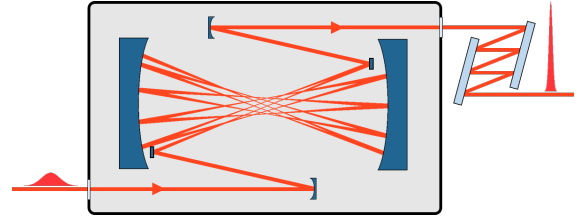


Figure 1: Schematic of a gas filled multipass cell post-compression scheme.

In the second experiment [4] we report on the first nonlinear post-compression of the output of a Tm:fiber laser in a gas-filled MPC. The driving laser system delivers 138 fs pulses (FWHM) and 65 W of average output power at a repetition rate of 300 kHz at a wavelength of 1940 nm. The MPC setup in this case consists of two concave, enhanced silver mirrors suitable for few-cycle pulse generation. The nonlinear medium is krypton gas at 3 bar absolute pressure. The MPC delivers a record average output power of 51 W with pulses as short as 35 fs and 170 μJ pulse energy. The herein presented systems render ideal platforms to drive nonlinear frequency conversion, because they simultaneously delivers high average and high peak powers.

The authors acknowledge funding from TAB (021VF0048 and 2015FGR0094), FhG CAPS, ERC SALT, FISCOV, ErUM-FSP T05, HGF ExNet-0019-Phase 2–3, DeGeDe (2017 FGR 0076, 501100004404)

References

- [1] R. Klas *et al.*, PhotoniX **2**, 4 (2021).
- [2] S. L. Cousin *et al.*, Opt. Lett. **39**, 5383 (2024).
- [3] M. Karst *et al.*, Opt. Lett. **48**, 1300 (2023).
- [4] P. Gierschke *et al.*, Opt. Lett. **47**, 3511 (2022).

*maximilian.karst@uni-jena.de

†philipp.gierschke@uni-jena.de

Continuously tunable high photon flux high harmonic source

R. Klas^{*1,2,3}, A. Kirsche^{1,2}, M. Gebhardt^{1,2}, L. Eisenbach², W. Eschen^{1,2}, J. Buldt², H. Stark^{2,3}, J. Rothhardt^{1,2,3}, and J. Limpert^{1,2,3}

¹HI Jena, Fröbelstieg 3, 07743 Jena, Germany; ²IAP, FSU Jena Albert-Einstein-Str. 15, 07745 Jena, Germany;

³Fraunhofer Institute for Applied Optics and Precision Engineering IOF, Albert-Einstein-Str. 7, 07745 Jena, Germany

A laser-like and high-flux extreme ultraviolet light source on a lab-scale, based on high harmonic generation is presented. In the spectral range between 50 and 120 eV, the source delivers a state-of-the-art photon flux. In contrast to previously reported sources, it allows for continuous and gap-less tuning of the spectral emission lines at this high photon flux level.

High harmonic generation (HHG) is an elegant solution for laser-like radiation in the extreme ultraviolet (XUV) spectral region on a laboratory scale [1]. Nowadays it enables a plethora of applications, that could formerly only be done at large scale facilities like synchrotrons or free-electron lasers. However, the inherent comb-like structure of the emitted spectrum [1] can be detrimental for some applications that precisely require a particular photon energy, e.g., actinic mask inspection for EUV lithography at 13.5 nm (91.8 eV).

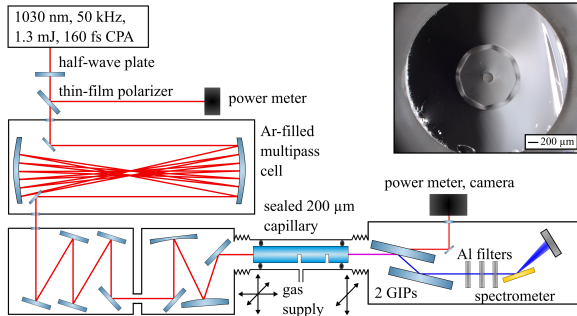


Figure 1: Simplified experimental setup. The inset shows the end facet of HHG-capillary. The core, an inner orthogonal fluorine-doped cladding and an outer fused silica cladding are visible [2].

In this contribution an experimental simple scheme for achieving a seamless tunability of the spectral position of the harmonic comb is demonstrated (Fig. 1) [2]. An Yb-fiber laser system delivering 160 fs, 1.3 mJ pulses at 1030 nm and 50 kHz is used. The pulse energy can be precisely attenuated by a combination of a half-wave-plate and thin-film polarizer. These pulses are spectrally broadened in an argon-filled multi-pass cell and compressed with a chirped mirror compressor having a fixed dispersion of -1400 fs^2 [3]. The entire system is designed in a way, that an attenuation of the initial pulse energy leads to negatively chirped pulses after the compressor, which are used to drive HHG in capillary filled with argon or helium.

* robert.klas@uni-jena.de

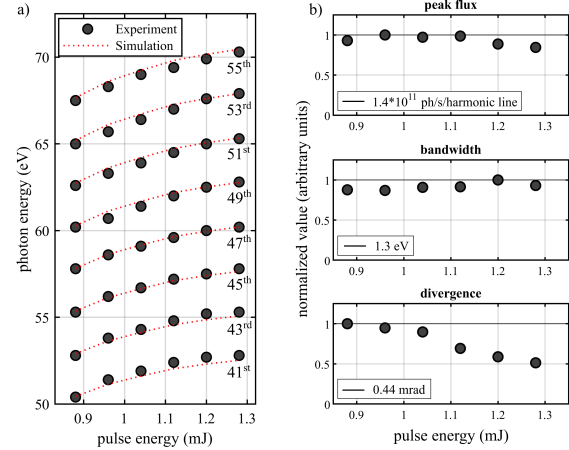


Figure 2: Characterization of tunable harmonic spectrum of argon with the maxima of each harmonic line (a) and its peak flux, bandwidth and divergence (b) [2].

The propagation of the negatively chirped pulses in the capillary results in blue-shifting and self-steepening, which strength depends on the chirp of the initial pulse [4]. This translates to a change in the instantaneous wavelength at the peak of the laser pulse and consequently in spectral shift of the harmonic position. The experimental and theoretical results are shown in Fig. 2, showing an excellent agreement [2].

Overall, this source delivers a state-of-the-art photon flux of $> 10^{11} \text{ ph/s/eV}$ ($> 10^9 \text{ ph/s/eV}$) in the spectral region of 50 to 70 eV (80 to 120 eV) using argon (helium), while the peak flux, bandwidth of a harmonic line and the divergence of the XUV beam are nearly constant over the entire tuning range [2]. This novel source will enhance and facilitate a broad range of applications, e.g. nanoscale imaging and ultrafast spectroscopy [5].

The research was supported by the ERC (835306, SALT); Helmholtz (ECRAPs); Fraunhofer (CAPS); BMBF(13N12082).

References

- [1] Popmintchev *et al.*, Nature Photonics **4**, (2010).
- [2] Kirsche *et al.*, Opt. Express **31**, (2023).
- [3] Grebing *et al.*, Opt. Lett. **45**, 117 (2020).
- [4] Saleh *et al.*, Phys. Rev. Lett. **107**, 117 (2011).
- [5] Loetgering *et al.*, Opt. Express **30**, 117 (2022).

A new target chamber for the TAF target area

P. Hilz^{*1}, T. Köhler², M. C. Kaluza², and M. Zepf^{1,2}

¹HI Jena, Fröbelstieg 3, 07743 Jena, Germany; ²IOQ, FSU Jena

This annual report provides an update on the current status of the main target chamber in the new extension building of the Helmholtz Institute Jena (HIJ). The target chamber is a crucial component of a larger infrastructure project undertaken at the HIJ that aims at the combination of the institute's high-power lasers (POLARIS and JETi200) for future experiments.

A major infrastructure project is currently underway at the Helmholtz Institute Jena (HIJ) to establish a state-of-the-art experimental area in the newly extended building of the Institute. The project involves the integration of two high-power laser systems, namely Polaris and JETi200, to enable combined experiments. These two laser systems, although different in terms of pulse duration, laser energy, and frequency, both have the capability of producing relativistic intensities individually. This unique combination offers an exceptional experimental platform.

The main objective of this endeavor is to create an advanced target area that will allow researchers to conduct groundbreaking experiments. Some of the potential experiments include exploring quantum electrodynamic processes such as Breit Wheeler pair production and implementing advanced multi-modal pump-probe schemes to characterize laser plasma-based processes in real-time.

However, there are several challenges that need to be addressed in order to realize this project. Synchronizing the lasers in time and guiding the beams through the beam-lines into the new target area are crucial tasks. Another key component of the project is the construction of the new main target chamber at Fraunhoferstr. (TAF), where the experiments will take place in the future.

The new target chamber was delivered in 2023 and was designed with a modular approach to facilitate its installation in the new building. It consists of five modules, each measuring 1.2 meters in length and 2.4 meters in width. The combined modules create a vacuum volume of 6 meters by 2.1 meters, with a height of 1.2 meters (see Figure 1). The chamber's side flanges are designed as doors to ensure easy access to the experimental setups.

Within the target chamber, there is a separate decoupled breadboard composed of two modules measuring 2.1 by 3 meters. It is supported by a sturdy welded frame to maintain the stability of the optical setups inside the chamber (see blue structure in Figure 1). The breadboard features multiple holes that allow for the direct placement of alignment-insensitive heavy components, such as radiation shielding or large magnets, onto the chamber floor instead of the breadboard itself (see Figure 2).



Figure 1: Exterior view of the TAF target chamber. The two ISO 500 flanges on the front are the connection ports for the TOR chamber.



Figure 2: Interior view of the TAF target chamber. The holes in the breadboard are the heavy duty ports (see text).

With the installation of the TAF target chamber the next components of the vacuum system can be installed in the near future. Two main components are the so called ‘wedding chamber’, which will combine the Polaris and JETi beam line or the TOR chamber, which is a switch yard and beam manipulation chamber for JETi and Polaris.

^{*}p.hilz@gsi.de

A common control system for JETi200 and POLARIS at HI Jena

D. Hollatz^{*1}, P. Hilz¹, A. Kessler¹, C. Lee¹, and M. Zepf^{1,2}

¹HI Jena, Fröbelstieg 3, 07743 Jena, Germany; ²IOQ, FSU Jena

The extension building of the Helmholtz-Institut Jena offers new opportunities for high intensity laser experiments with JETi200 and POLARIS in the new Target Area Fraunhofer. The scale of those experiments with both lasers along experimental diagnostics and data management requires a common control system, for which we selected Tango Controls. In this annual report we present the current status of the system architecture as well as a selection of applications beyond the control system aspect.

JETi200 and POLARIS are the two high-intensity laser systems at the Helmholtz-Institut Jena, that were operated completely independent from each other since their installation over 10 years ago. With the new extension building completed in late 2022, Target Area Fraunhofer offers the opportunity to perform experiments with both systems at the same time [1, 2]. For this, they need to be united in many aspects, for example the vacuum systems and safety systems as well as spatial and temporal pulse overlap. One often overseen but essential part of this process is the software side of things, specifically laser control and data acquisition. We chose a distributed control system called Tango Controls as a tool to unite JETi200 and POLARIS in a common framework. At the same time, we want to be able to operate both systems independently if needed. With Tango Controls we solve this by creating independent Tango systems with their own databases for JETi200 and POLARIS as well as for the individual target areas as depicted on Fig. 1. The systems communicate with each other using the Common Object Request Broker Architecture (CORBA), a communication standard for systems composed of multiples operating systems, diverse hardware and different programming languages.

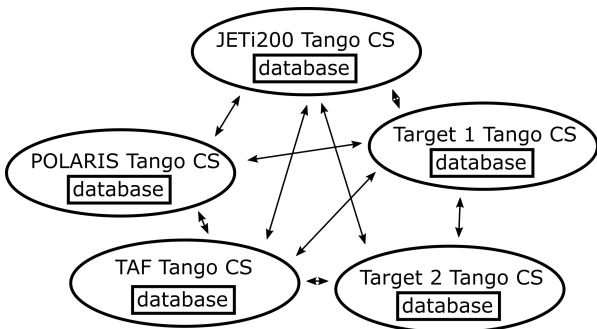


Figure 1: The HIJ control system composed of five independent Tango systems with their own databases.

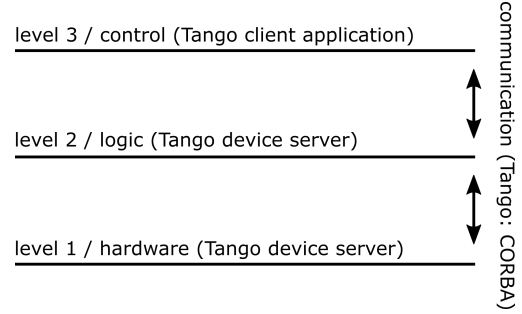


Figure 2: 3 level SCADA architecture of control systems.

Each Tango system is composed of multiple devices, the central concept and building block of Tango controls. Devices are created by device servers and implement a specific device class. A device can control hardware and provide its capabilities to the Tango system, essentially functioning as a hardware driver, or it can be purely logical, for example to provide microservices to the Tango system. Devices can have multiple commands, attributes and properties used to control the device. We use Tango controls to build our control system according to the Supervisory Control And Data Acquisition (SCADA) architecture, which categorizes all services into three levels as shown on Fig. 2. With Tango controls, elements of level 1 and 2 are both implemented as devices while level 3 elements are realized as Tango client applications.

A common control system like Tango controls offers more than just control of hardware but provides a common platform for any application such as data management and feedback loop implementation. One feedback loop that we are working on is an automatic pointing stabilization for JETi200 utilizing an artificial neural network to increase the fraction of usable shots at our experiments [3]. Here we acquire the laser pointing with kHz frequency and train the neural network to predict the deviation of the next shot. A motorized mirror is then used to steer the beam and compensate this deviation. Another application is data management and organization, especially the collection of meta-data, to interface to the Helmholtz Scientific Project Workflow Platform (HELIPORT). Beyond that, Tango controls paves the way for high-level feedback loops such as automated LWFA electron beam optimization.

References

- [1] D. Hollatz *et al.*, HIJ Annual Report 2021.
- [2] P. Hilz *et al.*, HIJ Annual Report 2022.
- [3] A. Sävert *et al.*, HIJ Annual Report 2022.

^{*}dominik.hollatz@uni-jena.de

HELIPORT Progress Report for 2022

Chien-Li, Lee* and Alexander Kessler

HI Jena, Fröbelstieg 3, 07743 Jena, Germany

HELIPORT is a Scientific Project Workflow Platform [1] that aims to make the entire life cycle of a project findable, accessible, interoperable and reusable according to the FAIR principles [2].

Under the scope of Helmholtz Metadata Collaboration (HMC)[3], our task is to connect the HELIPOINT system with the POLARIS database. In 2022 we deployed the HELIPOINT system (see figure 1) to the POLARIS Server (Linux system) which is located in the POLARIS Lab. For our POLARIS database, we installed the SciCat Metadata Catalog system on the server [4] (see figure 2). SciCat provides a Mongo database, a user interface with a powerful searching capability as well as the REST APIs for access to other programs. In order to cater the database in SciCat to the POLARIS experiment, we re-defined the names of some collections in SciCat's Mongo database so that experimental data as well as metadata can be properly stored. By using the generic python library called Pyscat, both writing and reading via REST APIs are implemented. In the writing part, LabView will first collect data and metadata e.g. from experimental diagnostics and then call Pyscat to transfer this data to SciCat's database.

After being stored in the database, the data of a laser shot (as the basic unit) will automatically be provided a PID (persistent identifier) which will be embedded in a URL. This URL can be manually stored within the Heliport Project by the users so that the users can retrieve their experimental data even after many years. With the help of HELIPORT and SciCat, the data are now one step further towards FAIR [2].

Finally, since our experimentalists want to have specific “table-like” displays of the data (see figure 3), we developed a Django user interface as a plug-in app within the HELIPORT system. This plug-in program will collect data from SciCat’s database using Pysiccat and display them in a table where columns are instruments’ values. In this web interface, the users can export the displayed data into Excel and CSV files. Also the features of hide/show columns and alias were added. We are currently working on storing the user’s settings in HELIPORT’s database.

References

- [1] <https://heliport.hzdr.de/>
- [2] <https://heliport.hzdr.de/principles/>
- [3] <https://helmholtz-metadaten.de/de>
- [4] <https://github.com/SciCatProject/documentation>

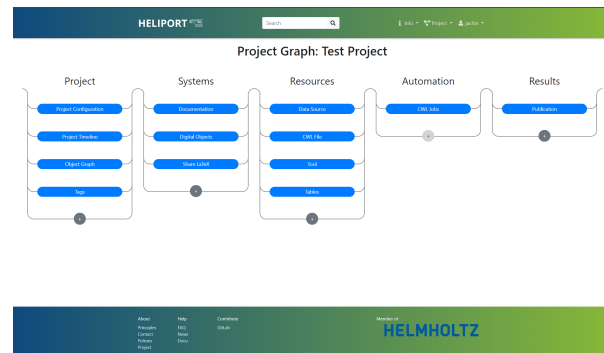


Figure 1: HELIPORT Web UI [1].

[illegible]

Figure 2: SciCat Web UI [4].

The screenshot shows the PyECLAIR web interface. At the top, there's a navigation bar with 'PyECLAIR' logo and links for 'my project' and 'Patterns Elements'. Below this is a 'Tools' section with a 'Tools' button. The main content area displays a table of instrument configurations. The table has 17 columns: Short, Time, E_min [meV], EF_Image, MF_Image, Probe_Z_Image, Probe_X_Image, Transmission_Image, Focus_Axis, Focus-X, Focus-MeasurementMethod, TA_Focus-Cut_Image, MCP-E_max, MCP-Image, PM-x_pos, PM-y_pos, PM-z_pos, and PM-use_calibration. The table lists four configurations for the 2018-05-02 run, with parameters like E_min, E_max, and various image and position values.

Short	Time	E_min [meV]	EF_Image	MF_Image	Probe_Z_Image	Probe_X_Image	Transmission_Image	Focus_Axis	Focus-X	Focus-MeasurementMethod	TA_Focus-Cut_Image	MCP-E_max	MCP-Image	PM-x_pos	PM-y_pos	PM-z_pos	PM-use_calibration
0	2018-05-02 12:00:00.000	0.00	None	None	None	None	None	None	None	None	TA_Focus-Cut_Image_1204C67.jpg	0.7869	None	0.0	0.0	0.0	None
1	2018-05-02 12:00:00.000	0.00	None	None	None	None	None	None	None	None	TA_Focus-Cut_Image_1204C67.jpg	0.7869	None	0.0	0.0	0.0	None
2	2018-05-02 12:00:00.000	0.00	None	None	None	None	None	None	None	None	TA_Focus-Cut_Image_1204C67.jpg	0.7869	None	0.0	0.0	0.0	None
3	2018-05-02 12:00:00.000	0.00	None	None	None	None	None	None	None	None	TA_Focus-Cut_Image_1204C67.jpg	0.7869	None	0.0	0.0	0.0	None

Figure 3: Plug-in UI in Heliport.

* chien-li.lee@uni-jena.de

Helmholtz Laser-Plasma Metadata Initiative (HELPMI)

A. Kessler¹, M. Kaluza¹, H.P. Schlenvoigt², F. Pöschel², A. Debus², V. Bagnoud³, U. Eisenbart³, and J. Hornung³

¹HI-Jena, Fröbelstieg 3, 07743 Jena, Germany; ²HZDR, Bautzner Landstraße 400 01328 Dresden, Germany ; ³GSI, Plankstraße 1, 64291 Darmstadt, Germany

HELPMI project aims at initiating a metadata (MD) standard for High-Intensity-Laser Systems (HIL) and correlated experimental data following the F.A.I.R. principles by defining a vocabulary and an ontology thereof. While for simulation data the OpenPMD standard is already well established, neither an exchange MD nor file format for experimental setups and data are available so far. With HELPMI we will close this gap and define a standard, which will be digitally hosted, machine-readable and extensible by all members of the community.

The tremendous progress enabled by HIL systems opens up new horizons in fundamental research and applications. E.g. relativistic interactions occurring in laser-driven plasmas are widely accepted as one of the most promising next-generation accelerator technologies (LPA: Laser-Plasma-Accelerator) [1]. The physical processes behind are highly non-linear and extremely complex, such that experimental creativity and adaptive studies are required to harness and exploit this technology in the future. In addition, the observations from experimental studies need to be compared against numerical simulations. Sophisticated codes based on the particle-in-cell approach are developed and used by many groups worldwide. In order to compare models and simulation results, benchmark codes and the need for common data postprocessing tools have been the motivation for the development of an open and open-source metadata standard **OpenPMD** [3].

Within the experimental community a similar metadata standard has so far not been established yet, in fact not even been defined, even though there is a wide agreement on the type of relevant data. We consider to use **NeXus** [4] as the starting point. NeXus is a community-driven and well-established MD and file format standard for experiments in the Photon and Neutron (PaN) science community.

OpenPMD and NeXus are structured container formats with keywords, attributes and data, exhibiting structure and data upon reading, similar to an office document with embedded tables, calculations etc. Hence, it is highly likely to find schemes and workflows applicable to HIL experiments, e.g., “beams”, “geometry”, “detectors” etc. but these would still have to be transferred into the HIL context. Meta-standard means that it defines the logical layout of particle-mesh datasets in an implementation-independent manner, while allowing for domain-specific standard extensions like the existing extension for particle-in-cell codes.

To determine the community’s requirements, we will organize workshops during HELPMI’s starting phase and ad-

ditionally include some major labs as project observers. We aim at a wide acceptance of the MD standard, what is of out-most importance for sustainability beyond the time frame of this project.

The task of HI-Jena will be to develop a dictionary and an ontology for the HIL community and to offer an example of a self-describing file containing experiment and laser system data provided with rich metadata according to the F.A.I.R. principles.

The authors acknowledge funding from Helmholtz Metadata Collaboration Platform.

References

- [1] <https://www.helmholtz-ard.de/>
- [2] <https://www.icuill.org/>
- [3] <https://www.openpmd.org/>, <https://zenodo.org/record/1167843>
- [4] <https://www.nexusformat.org/>

LASER PARTICLE ACCELERATION

Highly efficient proton acceleration from solid and pre-expanded thin foils

I. Salaheldin^{*1,2}, M. Shi^{1,2}, P. Hitz¹, A. Sävert^{1,2}, G. Schäfer^{1,2}, and M. Zepf^{1,2}

¹HI Jena, Fröbelstieg 3, 07743 Jena, Germany; ²FSU Jena

We present the preliminary results of proton acceleration from laser irradiated plastic foils of different thicknesses. We consider the effect of circular (CP) and linear (LP) polarization on the proton energy spectra. Further, we study the impacts of pre-expanding the target by introducing a pre-pulse that arrives at the target a few picoseconds before the main pulse. Record peak proton energies per Joule of laser energy are observed.

The experiment was conducted with JETi200 laser at the Helmholtz Institute-Jena. The focal spot diameter was measured to be $1.8 \mu\text{m}$ (FWHM), with 2 J on target and a pulse duration of 25 fs. This leads to a peak intensity of $3 \times 10^{21} \text{ W/cm}^2$. Fig. 1 shows the experimental setup.

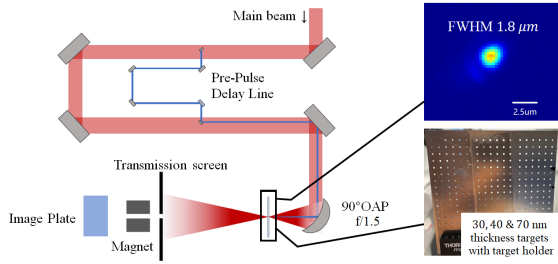


Figure 1: Schematic of the experimental setup.

For CP, a maximum proton energy of $\approx 33 \text{ MeV}$ was observed with a target thickness of (30 – 40) nm. It is interesting to note that the optimal target thickness for radiation pressure acceleration (RPA) is given by $L = \frac{a_0 n_c}{\pi n_0} \lambda$, where n_0 and n_c are the electron and the critical density, respectively. In our case, this corresponds to $L \approx 30 \text{ nm}$, as $n_0 = 230 n_c$ at $\lambda = 800 \text{ nm}$. Such an optimum is absent for the LP scan (cf. Fig. 2).

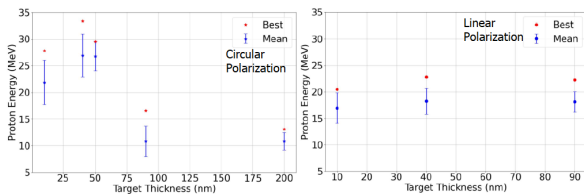


Figure 2: The dependence of the maximum proton energy on target thickness.

High-energy, mono-energetic proton beams can be obtained with thin targets (10 – 50) nm with circular polarization, whereas for thicker targets (90 – 200) nm the mono-energetic feature is lost and the cut-off energy is significantly lower, as shown in Fig. 3.

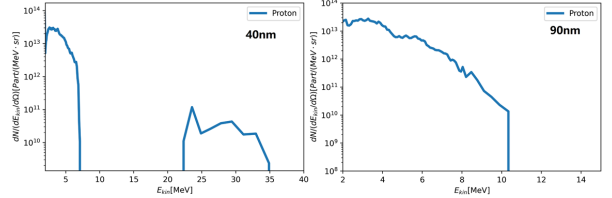


Figure 3: The energy spectra for proton beams from 40 nm and 90 nm targets with CP irradiation.

We have further studied the effect of pre-expansion of the target by introducing a controlled pre-pulse ($I_{pp} = 4 \times 10^{15} \text{ W/cm}^2$) with variable time delays (0 – 20) ps with respect to the main pulse. Depending on the time delay, the target density may drop before the main pulse irradiates the target. Maximal proton energies are slightly lower in expanded foils, and further study is needed to determine if alternative mechanisms scale better than un-expanded foils.

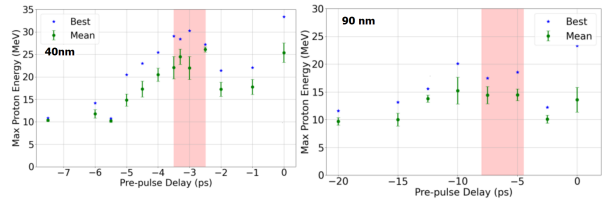


Figure 4: Maximum proton energy dependence on pre-pulse delay for 40 nm and 90 nm targets with CP irradiation. The pink area corresponds to the delay interval where the mono-energetic beams are observed.

In summary, the effect of laser polarization and target thickness on the energy of the protons accelerated from solid foils were investigated. For a circularly polarized laser, a sharp transition to high peak energies and quasi-monoenergetic spectra is observed for targets $> 90 \text{ nm}$. A variable time delay pre-pulse was used to investigate the effect of target pre-expansion on proton cut-off energy. An optimum pre-pulse level was clearly observed, but no improvement over the global optimum at 40 nm without pre-pulse. These results show the most efficient conversion of laser energy into proton kinetic energy to date. In comparison to experiments with similar parameters [2], both cut-off energy and spectrum are significantly improved.

References

- [1] A. Macchi *et al.*, Phys. Rev. Lett. **103**, 085003 (2009).
- [2] F. Dollar *et al.*, Phys. Rev. Lett. **108**, 175005 (2012).

* i.salaheldin@gsi.de

Observation of relativistic postsolitons

A. Sävert^{*1}, C. Zepter², M. C. Kaluza^{1,2}, and M. Zepf^{1,2}

¹Helmholtz Institute Jena, Fröbelstieg 3, 07743 Jena, Germany; ²Institute for Optics and Quantum Electronics, Friedrich Schiller University, Max-Wien-Platz 1, 07743 Jena

Electromagnetic postsolitons have been observed after the interaction of an ultra intense laser pulses with a plasma. They are the remains of an electron-ion plasma sub-cycle soliton, evolving on the ion dynamical time scale. These spherical expanding plasma structures can be used as a model for the supernovae explosions [1]. Hence, astrophysical phenomena like acceleration of charged particles in a shock wave and cosmic ray acceleration can be studied in the laboratory.

Relativistic solitons are formed in the wake of a collapsing ultra intense laser pulse. The high electron density spikes in a strong nonlinear wakefield can trap red shifted light from the laser pulse. The postsoliton is the slowly expanding cavity in the ion and electron densities and can emit coherent synchrotron radiation [2].

We performed the experiment at the JETi-laser at the Institute for Optics and Quantum Electronics in Jena delivering pulses of 750 mJ energy and 35 fs duration. The pulses were focused by an f/13 off-axis parabolic mirror to an elliptical focal spot with dimensions (FWHM) $(8.9 \times 12.8) \mu\text{m}^2$ containing 27% of the energy resulting in FWHM intensities of $I_L = 6 \times 10^{18} \text{ W cm}^{-2}$.

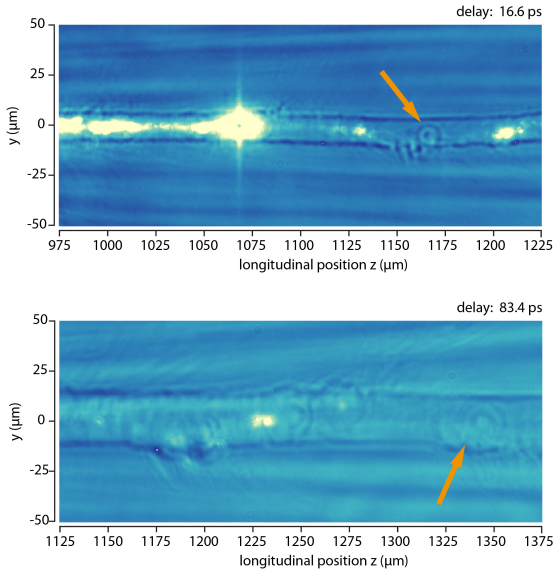


Figure 1: Temporal evolution of a postsoliton

A supersonic gas jet was used, generating a plasma with electron density $n_e = 2.5 \times 10^{19} \text{ cm}^{-3}$. We used a few-cycle microscopy setup consisting of synchronized probe beam, with a pulse duration of $\tau_{\text{probe}} = 6 \text{ fs}$, and a high

resolution imaging system, with $R < 1.5 \mu\text{m}$, to image the interaction on a CCD camera. By varying the delay between pump and probe, different stages of the postsoliton's evolution were recorded. The position in the gas jet $\approx 1.2 \text{ mm}$ was chosen close to the calculated depletion length of the laser pulses.

Exemplary snapshots are shown in Fig. 1. Here, the evolution of a postsoliton at two different time steps, 16.6 ps and 83.4 ps is shown. The sphere has grown in size and reaches a diameter of $6 \mu\text{m}$ after 16.6 ps and $15 \mu\text{m}$ after 83.4 ps. The temporal evolution of this 3D spherical postsoliton is given by Bulanov and Pegoraro analytically [1]. The diameter of the sphere is hereby given by $d(t) = d_0[5.2 \cdot t/t_0]^{1/3}$. The best fit of this function to our measured data shows a good qualitative agreement. $d_0 = 2 \mu\text{m}$ denotes the resulting initial diameter and $t_0 = 0.79 \text{ ps}$ the time of creation. However, using the high temporal resolution of our probe beam we were able to observe the postsoliton directly after its creation. The creation time of 10s of femtosecond is hereby much shorter than the result of the fit.

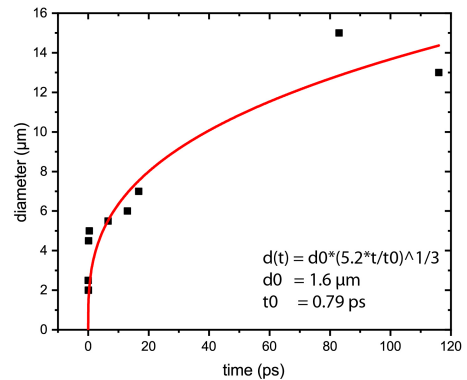


Figure 2: Expansion of postsolitons in spherical geometry.

In summary, using few-cycle microscopy we were able to observe the creation and evolution of postsolitons. The measured expansion rate can be described analytically quite well. In the future, the use of multiple probe beams would allow us to record the evolution of the same postsoliton as well as its motion, as predicted by theory [1].

References

- [1] S.V. Bulanov *et al.*, Phys. Rev. E **65**, 066405 (2002).
- [2] Esirkepov *et al.*, Phys. Rev. Lett **92**, 255001 (2004).
- [3] A. Sävert *et al.*, Phys. Rev. Lett. **115**, 055002 (2015).

* a.saevert@hi-jena.gsi.de

LWFA-Electron Dependence on Pulse Front Tilt

C. Zepter^{*1,2}, A. Seidel^{1,2}, A. Sävert², M. Zepf^{1,2}, and M. C. Kaluza^{1,2}

¹HI Jena, Fröbelstieg 3, 07743 Jena, Germany; ²IOQ, FSU Jena

We report on the influence of spatio-temporal coupling on the electron beam pointing. Laser pulses with a focal spot exhibiting a spatial chirp (SC) were used to accelerate electrons via laser driven wakefield acceleration (LWFA). By changing the laser's group delay dispersion (GDD) and hence the pulse front tilt (PFT) the electron pointing position could be steered reliably by several mrad while the electron beam's divergence and charge density remain unchanged.

In LWFA the acceleration process can be significantly affected by the evolution of the laser pulse during the propagation through the plasma. For numerous applications such as multistaged accelerators or radiation sources the need for a stable and reliable acceleration regime is inevitable [1, 2]. Therefore, a systematic and deeper understanding of both laser and plasma physics is required to achieve this regime and to explore the limits within which this stable acceleration process can occur.

A laser pulse exhibiting spatio-temporal couplings, caused for example by a small misalignment in the compressor of CPA systems, deviates from a perfectly matched laser pulse for LWFA experiments. Consequently, the question arises, how such couplings in the laser change the laser-plasma interaction and consequently the electron acceleration leading to differences in the electron beam properties.

The experiment was performed at the JETi-200 laser system at the Helmholtz Institute in Jena. The laser beam with a FWHM pulse duration of 21 fs measured in the near field and energy of 4.1 J was focused by an f/21 off-axis parabola to a FWHM focal spot diameter of 20 μm reaching an intensity of $3.9 \times 10^{19} \text{ W/cm}^2$. The electrons were accelerated in a 5.3 mm long gas cell target with a helium-nitrogen mixture and an electron density of $5 \times 10^{18} \text{ cm}^{-3}$ reaching energies up to 380 MeV using ionization injection. By changing the laser compressor's alignment the angular chirp in the laser near field in vertical direction and therefore the SC in the focal plane of the laser was changed resulting in a slight increase in the focus' vertical dimension as different spectral components were focused to different transverse positions.

Fig. 1 shows the results for two different SCs. It can be seen in (a) that the electrons' vertical pointing position changes with applied GDD up to 12 mrad showing a direct correlation between a PFT in vertical direction and the electron's steering direction. Furthermore the magnitude of the electron deflection amplitude gets larger with larger SC and therefore larger PFT for the same values of GDD.

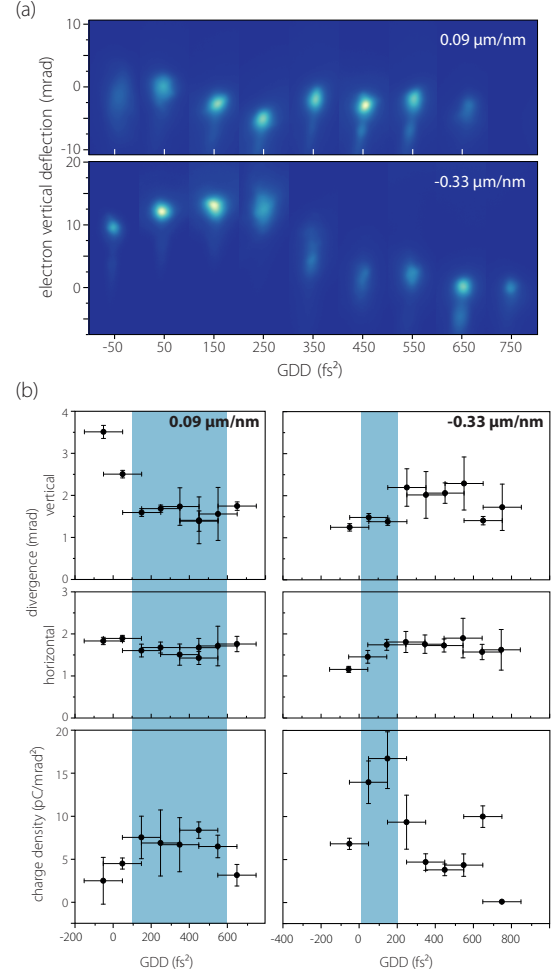


Figure 1: Electron beam properties for different SCs in focus and different GDDs.

In (b) it can be seen that for both SCs acceleration regimes can be found, where the vertical and horizontal divergence are $< 2 \text{ mrad}$, however, with a larger SC a higher charge density could be achieved. This shows that a steering of the electron beam could be achieved without significantly changing the other properties of the electron beam and even reaching higher charge densities for larger SCs.

References

- [1] S. Steinke *et al.*, Nature. **530**, 190-193 (2016).
- [2] M. Labat *et al.*, Nat. Photon. **17**, 150-156 (2023).

* carola.zepter@uni-jena.de

Laser-plasma experiments with microdroplet targets

G. A. Becker^{*1}, M. Nolte¹, M. Beyer², M. B. Schwab¹, D. Klöpfel², M. Hornung², M. Hellwing¹, F. Schorcht², and M. C. Kaluza^{1,2}

¹Institut für Optik und Quantenelektronik, Friedrich-Schiller-Universität Jena, Germany; ²Helmholtz Institute Jena, Fröbelstieg 3, 07743 Jena, Germany

Liquid microdroplets are a very interesting target for laser-plasma experiments due to their limited volume and availability at high repetition rates. A pump-probe experiment was performed to characterize the stability of such a target system and the expansion of a plasma triggered by a millijoule pump laser. Ray tracing simulations were performed to determine the plasma density at a specific region of the captured images. Finally, the target system was implemented in a proton acceleration experiment at the POLARIS laser system. In this experiment, the profiles of proton beams originating from droplets of two different liquids were compared.

Microdroplets originating from nozzles are available at repetition rates of ≈ 1 MHz and have a limited volume. The latter characteristic makes these targets interesting for ion acceleration experiments with high-intensity lasers ($I_L > 10^{18} \text{ Wcm}^{-2}$) since the generated hot electron plasma, responsible for the electric field that accelerates the ions, is confined to the interaction region. The droplet source was characterized in a dedicated laboratory equipped with a vacuum chamber and millijoule laser system delivering pulses with a full-width-at-half-maximum pulse duration of $\tau \approx 130$ fs [1]. A 90:10 beam splitter was used to split the laser into a pump and a probe beam. The pump was frequency doubled to 515 nm and focused onto the droplets to $I_L \lesssim 10^{17} \text{ Wcm}^{-2}$ to generate a plasma. Pre-pulses with similar intensities are used in laser-plasma experiments at high-power laser facilities to generate a pre-plasma prior to the arrival of the main pulse with $I_L > 10^{18} \text{ Wcm}^{-2}$. The pre-plasma affects the coupling of laser energy into the target and has, e.g., a significant influence on the kinetic energies of laser-accelerated protons [2]. The low energy part of the laser, with a spectrum centered around 1030 nm, was used as a probe laser to illuminate the droplets and the plasma expansion which were imaged onto a CCD camera. For water droplets an optimal spatial stability with $\sigma_x \approx 0.7 \mu\text{m}$ and $\sigma_y \approx 0.5 \mu\text{m}$ was measured [3]. Fig. 1a shows the expansion of the irradiated part of the surface of a water droplet 49 ps after the arrival of the pump laser pulse. To better identify regions with a certain plasma density, ray tracing simulations were performed and synthetic shadowgraphic images were created (Fig. 1b). The teal circle marks the droplet with a constant electron plasma density of $220 n_c$. n_c is the critical density of a plasma. The plasma density exponentially decays in the outward direction with a scale length of $0.5 \mu\text{m}$. Lime green marks n_c , while dark green marks $0.005 n_c$. Hence, the black edge of the expanded

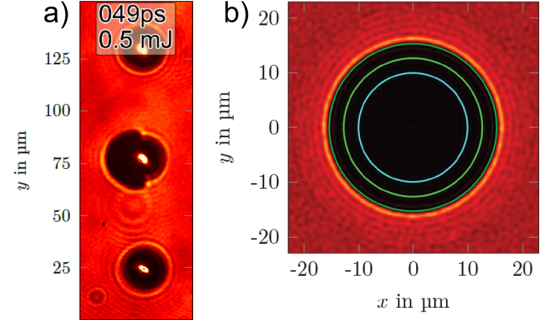


Figure 1: a) shows the plasma expansion of a water droplet and b) shows a simulated shadowgraphic image.

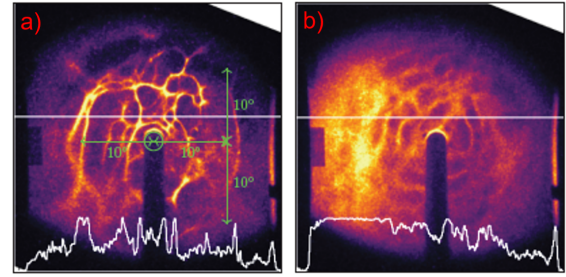


Figure 2: Beam profile of protons accelerated from water micro droplets (a) and ethylene glycol droplets (b).

droplet in Fig. 1a can be identified as plasma with this density. At the POLARIS laser system [4], an ion acceleration experiment was performed, in which droplets of water and ethylene glycol were irradiated by laser pulses having $I_L > 10^{19} \text{ Wcm}^{-2}$, and the resulting proton beam profile was measured (Fig. 2). The beam profile emitted from ethylene glycol droplets is more homogenous (b). This is likely a consequence of the much lower vapour pressure of ethylene glycol compared to water (0.08 mbar vs. 23 mbar). The remaining laser light outside of the focal area ionizes the evaporated liquid around the droplets leading to spatially varying electric fields that deflect the protons leading to modulated patterns [5]. Hence, it could be shown that the use of ethylene glycol leads to smoother proton beam profiles better suited for applications.

References

- [1] G. A. Becker *et al.*, HI Jena Annual Report 2021, p. 30.
- [2] G. A. Becker *et al.*, Sci. Rep. **9**, 17169 (2021).
- [3] M. Nolte, Master's thesis, FSU Jena (2023).
- [4] M. Hornung *et al.*, Opt. Lett. **41**, 5413 (2016).
- [5] L. Obst-Huebl *et al.*, Nat. Commun. **9**, 5292, (2018).

*georg.becker@uni-jena.de

Probing Ultrafast Laser-Induced Solid-to-Overdense Plasma Transitions

Y. Azamoum^{*1,2}, G. A. Becker², S. Keppler^{1,2}, G. Duchateau³, S. Skupin⁴, M. Grech⁵, F. Catoire⁶, I. Tamer^{1,2}, M. Hornung^{1,2}, M. Hellwing², A. Kessler¹, F. Schorcht¹, and M. C. Kaluza^{1,2}

¹Helmholtz Institute Jena, Germany; ²IOQ, FSU Jena, Germany; ³CEA-CESTA, France; ⁴ILM, CNRS, Lyon 1 Univ., France; ⁵LULI, CNRS, CEA, Sorbonne Univ., IP Paris, France; ⁶CELIA, Bordeaux Univ.-CNRS-CEA, France

The knowledge of target dynamics is key for realizing an efficient laser-driven ion acceleration using thin foils, yet it is hardly accessible in experiment or modeling. By capturing the solid-to-plasma transition during the laser's rising edge at intensities $I \sim 10^{15} - 10^{16} \text{ W/cm}^2$, the detailed target evolution is achieved. Single-shot probe transmission measurements and a Two-Step model provide unique insights into the interplay of ionization, collisions and expansion.

Controlling the pre-plasma evolution during the rising edge of an intense laser interacting with nanofoils is highly sought after as it defines the initial conditions of the ion acceleration process. Schemes based on the relativistic induced transparency [1] promise efficient and volumetric electron heating as the peak penetrates a near-critical overdense plasma due the relativistic mass increase of the electrons. Hence, a pre-plasma evolution matched to the rising edge is needed. While the required nm-spatial and fs-temporal resolutions are only achievable on large machines, modeling of the pre-plasma is so far based on approximations. Here we investigate the initial phase of plasma formation during the rising edge which is, to the best of our knowledge, not yet described in the literature. This leads conveniently to detailed pre-plasma properties at the peak arrival. A 5 nm-thick Diamond-Like Carbon (DLC) foil transits from solid state to plasma during the pump laser rising edge depicted in Fig. 1(a) (shaded region) with $I_{\text{peak}} \sim 10^{15} - 10^{16} \text{ W/cm}^2$. The interaction region is longitudinally

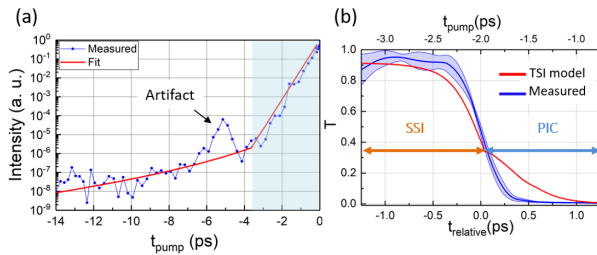


Figure 1: (a) Laser temporal intensity contrast, (b) Measured T (blue) with shaded region being the standard deviation over several shots, and T (red) from TSI model.

illuminated with a broadband chirped probe pulse where, by wavelength conversion into time, the probe transmission dynamics is recorded [2]. The measured transmission T in Fig. 1(b) shows a sub-picosecond transition from a transparent, solid state represented by the plateau to an overdense plasma $T \sim 0$ with $\tau \sim 700 \text{ fs}$ being the time required for

T to drop from 90 % to 10 %. As discussed in [2], $T \sim 0$ can be reached only with a highly overdense (electron density $n_e \gg n_c$ critical density) and expanding plasma due to the large probe tunneling expected for nanofoils. The experimental findings were better described using an original two-step interaction (TSI) model. The transmission in Fig. 1(b) (red line), is computed assuming a probe propagating through the plasma with n_e calculated from the TSI. The Drude Model and a Maxwell solver considering the probe tunneling and its multiple reflections in the foil are used. The TSI starts with a solid state interaction

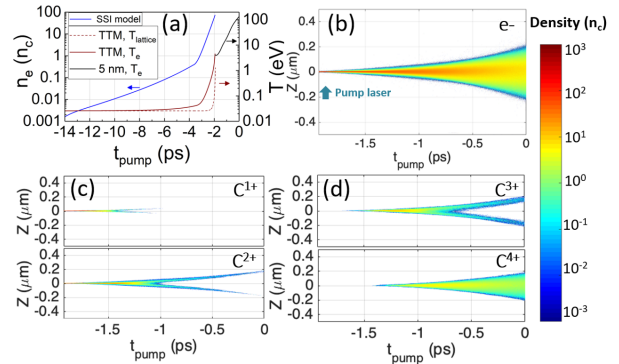


Figure 2: (a) $n_e(t)$ from SSI model and temperatures T_e and T_{lattice} from TTM and the PIC code. (b), (c) and (d) Space-time evolution of n_e and ions' densities in PIC.

(SSI) model which describes the plasma formation from the solid including the MultiPhoton Ionization (MPI) and the DLC band structure [2]. At the DLC melting temperature $T_{\text{lattice}} \sim 0.34 \text{ eV}$, the SSI is bridged to the Particle In Cell (PIC) code with a plasma slab initialized with n_e and carbon ion densities and temperatures obtained using a two-temperature model (TTM) (Fig. 2(a)) [3]. In Fig. 2, n_e and carbon ions density profiles confirm the expected and strong expansion of an overdense plasma. Besides, tunneling ionization does not play a role in the experiment despite being in a suitable intensity range. MPI dominates in SSI whereas collisional ionization governs in PIC [3]. This investigation provides detailed pre-plasma properties at the peak arrival. In the future, this method will be tested to achieve unprecedented pre-plasma description in the relativistic regime.

References

- [1] A. V. Brantov *et al.*, PRL **116**, 085004 (2016).
- [2] Y. Azamoum *et al.*, HI Jena Annual Reports 2019–2021.
- [3] Y. Azamoum *et al.*, to be submitted (2023).

*yasmina.azamoum@uni-jena.de

Shadowgraphy of the plasma evolution around water micro-droplets irradiated by high-power laser pulses

M. Beyer^{*1,2}, Y. Azamoum^{1,2}, M. Nolte¹, G. A. Becker¹, M. B. Schwab^{1,2}, M. Hornung^{1,2}, M. Hellwing¹, and M.C. Kaluza^{1,2}

¹Institute of Optics and Quantum Electronics Jena, Germany; ²Helmholtz Institute Jena, Germany

We present the results of an off-harmonic, optical probe experiment at the POLARIS laser, in which the laser-plasma interaction with water micro-droplets was investigated. In contrast to experiments with thin foils, the limited extension of water droplets facilitates a direct imaging of the plasma expansion process using shadowgraphy. The strong emission of the laser-induced plasma at the fundamental and second harmonic frequency was suppressed by an off-harmonic probe, a polarization and a spatial filter. A detailed analysis of the shadowgraphy images allowed us to estimate the plasma expansion velocity.

The probing system [1] utilizes a single pass non-collinear optical parametric amplifier (NOPA) with a μJ -level probe energy and a broad bandwidth between 750 nm to 950 nm. In the experimental setup, a jet of water is generated by a nozzle that is broken up into droplets with a diameter of 20 μm . The POLARIS main laser pulses (100 TW) are focused onto the water droplets by a 30 cm focal length off-axis parabola to intensities of $4 \times 10^{19} \text{ W cm}^{-2}$. The probe pulses are first sent through a delay stage to adjust the temporal delay between main and probe pulse (c. f. figure 1).

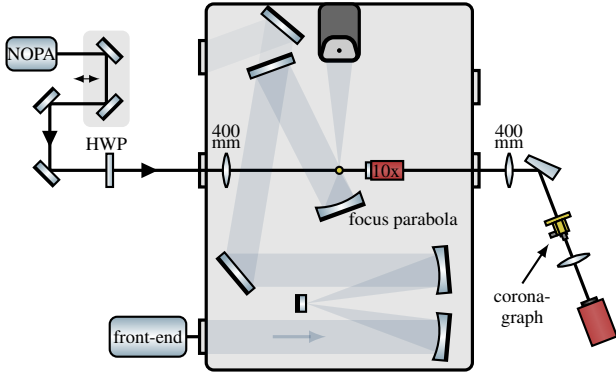


Figure 1: Experimental setup of the laser-matter interaction and the imaging system of the probe [2].

The imaging setup consists of a Mitutoyo NIR10x objective, a glass plate placed under the Brewster angle to suppress scattered light of the main pulse and a spatial filter called *coronagraph*. As the plasma emission is restricted to cross-section of the droplet, the central region can be masked to block out the emission. Therefore, the droplets were first magnified and imaged in an intermediated plane where a small circular mask of diameter $d = 300 \mu\text{m}$ (c. f. figure 2) was positioned. Then the droplets were reimaged onto a camera.

*m.beyer@uni-jena.de

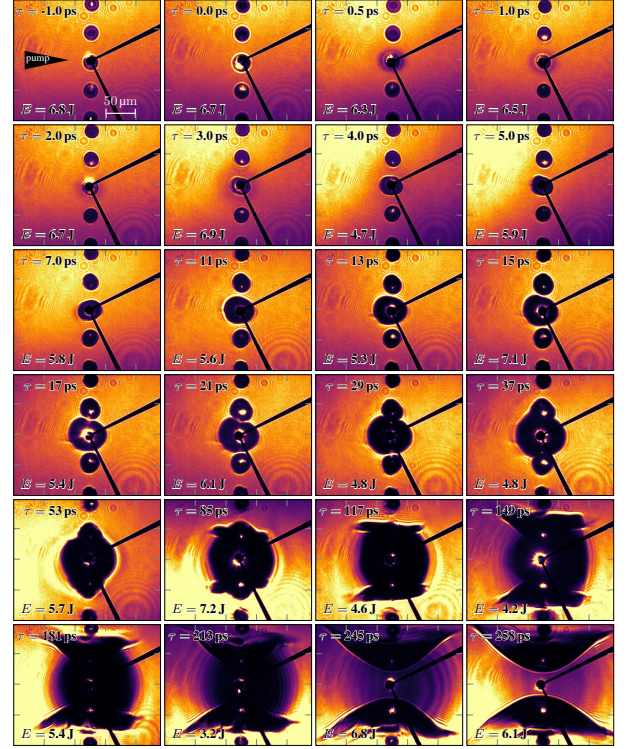


Figure 2: Shadowgraphy images of water droplets with coronagraph for different pump-probe delays τ [2].

When the rising edge of the main pulse arrives, a blackening of the central droplet can be observed, which is explained by ionization and the generation of an overdense plasma. For increased delays between probe and pump pulse, the spatial extend of the overcritical plasma is growing. The expansion of the plasma's critical density is estimated by measuring the size of the shadow. At $\tau = 3 \text{ ps}$ the plasma starts to grow rapidly, where the front side expansion ($v_{\text{front}} = 1.27(6) \mu\text{m/ps}$) is faster than on the rear side ($v_{\text{rear}} = 0.77(5) \mu\text{m/ps}$). For later times, both expansion velocities decrease. These values are much lower than the estimated ion sound speed $c_s = 15 \mu\text{m/ps}$ using the ponderomotive scaling [2, p.9] for hot electrons, which may suggest different intensity scalings of the electron temperature or the existence of a pre-pulse. However, the values agree well with results of similar experiments [3, 4].

References

- [1] I. Tamer *et al.*, Opt. Express **28**, 19034 (2020).
- [2] M. Beyer, Master's thesis (2022).
- [3] G. Becker *et al.*, Scientific Reports **9**, 17169 (2019).
- [4] C. Bernert *et al.*, Scientific Reports **12**, 7287 (2022).

Monoenergetic Electron Beams from Controlled Injection in a Multi-Stage Gas Cell

A. Seidel^{*1,2}, Z. Yu¹, C. Zepter^{1,2}, A. Sävert², D. Seipt^{1,2}, and M. Zepf^{1,2}

¹HI Jena, Fröbelstieg 3, 07743 Jena, Germany; ²IOQ, FSU Jena

We report on the development and experimental results of a multi-stage gas cell for controlled injection to generate high-energy monoenergetic electron pulses paving the way for their advanced application. It shows in first experiments that by choosing different gas-mixtures and partial-densities in the different regions of the multi-stage gas cell, electrons with a monoenergetic feature (energy spread σ_E of 1 %) can be realized.

The field of laser wakefield acceleration (LWFA) has rapidly progressed in the last decade and its basic principles are well understood. To go from the proof-of-principle acceleration process to mature accelerators, reliable plasma targets are needed that produce electrons of excellent quality - small emittance, small energy spread, high energies, high charge density - for advanced applications such as seeding of FELs [1] and conventional rf accelerators [2] or as a source for secondary radiation sources [3]. Simulations [4] show that in order to achieve these quality criteria, a staged gas cell design is well suited, consisting of a short region of high-Z gas for ionization injection, followed by a long region of low-Z gas for postacceleration without additional trapping of electrons, leading to high energy, monoenergetic high charge density electrons (see inset Fig. 1). Based on these considerations, a gas target was designed,

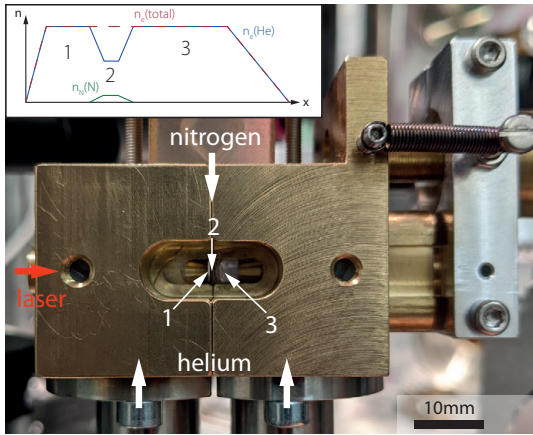


Figure 1: Image of the multi-stage gas cell inside the target chamber. The inset shows the plasma electron density n_e and the nitrogen atomic density (n_N) over the longitudinal position within the target.

which can be seen in Fig. 1. This gas cell consist of three distinct regions. The first region for stable guiding the laser pulse, the second region for controlled ionization using either ionization injection, downramp injection or a combi-

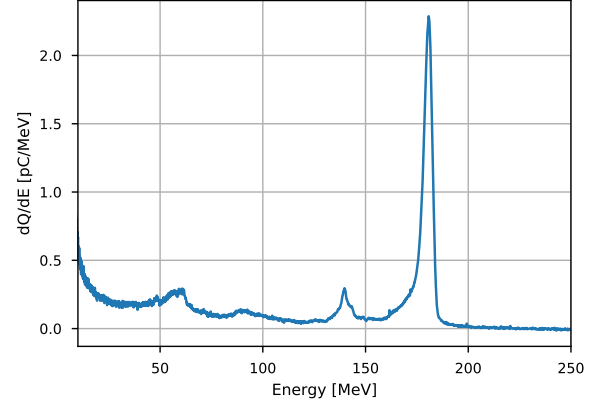


Figure 2: Energy spectrum of an electron bunch using the multi-stage gas cell and a combination of downramp and ionization injection.

nation of both and a third region with variable length for the acceleration of the injected electrons.

CFD simulations with helium in region one and three and nitrogen in region two show, that the width of the nitrogen region remains constant during its flow. However, maintaining a constant static pressure in all three regions is crucial to prevent turbulence and mixing caused by gas flow. First experiments with this staged gas cell were performed at the JETi-200 laser system at the Helmholtz Institute in Jena. The laser beam with a FWHM pulse duration of 23 fs measured in the near field and energy of 2.5 J on target was focused by an f/21 off-axis parabola to a focal spot of 22 μm reaching an intensity of $1.4 \times 10^{19} \text{ W/cm}^2$. The first region of the gas cell was a 1.5 mm long volume filled with helium, followed by a 0.4 mm long volume of nitrogen for injection and a 3 mm long volume of helium for postacceleration. The electron spectra were measured with a magnet spectrometer with an energy resolution of $< 1\%$. In Fig.2 a result of that measurement can be seen. It shows that in the downramp supported ionization injection regime electron bunches with a monoenergetic feature ($\sigma_E = 1\%$) around 180 MeV could be attained.

The authors acknowledge funding from DFG.

References

- [1] M. Labat *et al.*, Nat. Photon. **17**, 150–56 (2023).
- [2] S. Antipov *et al.*, Phys. Rev. Accel. Beams **24**, 111301 (2021).
- [3] N. Powers *et al.*, Nat. Photon. **8**, 28–31 (2014).
- [4] M. Chen *et al.*, Phys. Plasmas **19**, 033101 (2012).

*seidel.andreas@uni-jena.de

All-Optical Transverse Emittance Characterization of Laser-Plasma Accelerated Electron Beams

F. C. Salgado^{*1,2,3}, A. Kozan^{1,2,3}, D. Hollatz^{1,2,3}, A. Seidel^{1,2,3}, G. Schäfer^{1,2,3}, A. Sävert^{1,2,3}, D. Ullmann^{1,2,3}, Y. Zhao^{1,2,3}, M. Kaluza^{1,2,3}, and M. Zepf^{1,2,3}

¹IOQ, Friedrich-Schiller-Universität, Max-Wien-Platz 1, 07743 Jena, Germany; ²Helmholtz-Institut Jena, Fröbelstieg 3, 07743 Jena, Germany; ³GSI Helmholtzzentrum für Schwerionenforschung, 64291 Darmstadt, Germany

Here, we report the characterization of the transverse emittance of laser-plasma accelerated electron beams using conventional pepper-pot masks and compare the results with the novel all-optical method [1]. For our experimental conditions, an averaged normalized emittance of $(0.24 \pm 0.04) \pi$ mm mrad, and a source size of about $(2.4 \pm 0.2) \mu\text{m}$ were obtained.

The emittance determines the volume in phase space occupied by the particles of an accelerated beam, and, consequently, the quality of the beam provided by the accelerator. For example, a low emittance value corresponds to a high-quality particle beam, since the electrons are better confined in a smaller volume leading to a high beam brilliance.

Different diagnostic methods have been used in experiments to evaluate the emittance of electron beams. In particular, pepper-pot (PP) mask diagnostics have been widely used to characterize electron beams generated through laser-wakefield accelerators (LWFA). Recently, a new method was proposed by Ref. [1] which is capable of characterizing the ultra-low emittance of high-energy electron beams using laser interference (LI) patterns. In this work, we compare the emittance measurements using the conventional PP method with the novel LI method.

The setup of the experiment assembled in the JETi200 laser system at the Helmholtz-Institute Jena can be seen in Fig. 1. The main laser was split into two beams: a central beam of 60 mm diameter, and, a ring beam with an outer diameter of 120 mm and an inner diameter of 60 mm. The central laser beam is focused by an off-axis parabolic mirror (f-number = 16.7) to a spot with a normalized intensity of $a_0 \approx 1.8$. The focused laser impinged into a gas mixture of 95% H_2 and 5% N_2 which was used on the plasma accelerator with a density of approximately $1.1 \times 10^{19} \text{ cm}^{-3}$. With these parameters, electron beams with a root-mean-squared (RMS) divergence $\theta_{rms}^{PP} \approx (1.5 \pm 0.2)$ mrad for PP, $\theta_{rms}^{LI} \approx (2.1 \pm 0.3)$ mrad for LI measurements, and a weighted mean energy of (72.5 ± 5.7) MeV (Lorentz-factor $\gamma \approx 143$) were generated.

At first, we characterized the transverse emittance using a pepper-pot mask diagnostic using a 200 μm thick tungsten mask with holes of 50 μm diameter (pitch $\approx 120 \mu\text{m}$). After the electron beam propagated through the pepper-pot mask, beamlets are formed which are detected on a YAG:Ce (50 μm thickness) which was imaged by a high-resolution camera (Andor Marana, model 4.2B.6). An ex-

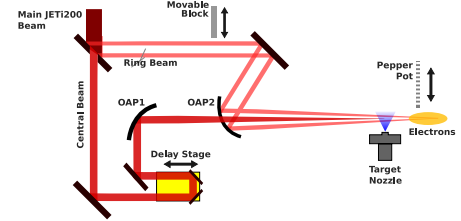


Figure 1: Sketch of the experimental layout. This setup allows the measurement of the emittance of electron beams using the PP or the LI methods.

ample of a shot of the imaged beamlets is seen in Fig. 2 (a). Using the method described by Zhang [2], we evaluated an average emittance of $\epsilon_n^{PP} = (2.0 \pm 0.4) \pi$ mm mrad, and an upper limit for the source size $\sigma_{PP} = \epsilon_n^{PP} / (\gamma \theta_{rms}^{PP}) \approx (29.0 \pm 6.4) \mu\text{m}$, demonstrating that the resolution of PP method is limited to resolve small source sizes.

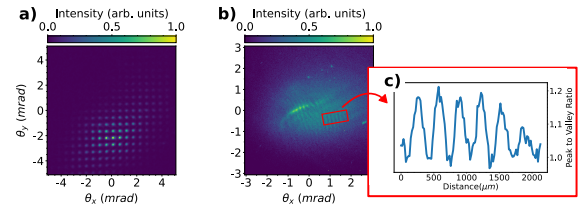


Figure 2: Example of shots for the emittance evaluation using (a) PP and (b) LI methods. (c) shows the peak-to-valley ratio (background subtracted) used to determine the emittance and source size from the LI result.

By removing the PP mask from the beam path and allowing the probe laser beam in the setup in Fig. 1 to interact with the electron beam, the emittance can be measured all-optically. Here, the modulated electron beam is then imaged again using the YAG:Ce screen as seen in Fig. 2 (b). The analysis resulted in an average source size of $\sigma_{LI} \approx (2.4 \pm 0.2) \mu\text{m}$, and normalized emittance of $\epsilon_n^{LI} = (0.24 \pm 0.04) \pi$ mm mrad, showing an improvement of an order of magnitude with respect to the PP method, and comparable to measurements using quadrupole scans [3].

This research was funded by the Federal Ministry of Education and Research of Germany (BMBF) in the Verbundforschungsframework (Project No. 05K19SJA).

References

- [1] A. Seidel *et al.*, Phys. Rev. Accel. Beams **24**, 012803 (2021).
- [2] M. Zhang, Fermi National Accelerator Lab. (FNAL), (1996).
- [3] R. Weingartner *et al.*, PRSTAB **15**, 111302 (2012).

*felipe.salgado@uni-jena.de

Simulating the Effect of Asymmetric Laser Wakefield Generated by Shock-front Rotation on Betatron X-rays

Harsh Harsh^{*1}, D. Seipt¹, and M. Zepf^{1,2}

¹HI Jena, Fröbelstieg 3, 07743 Jena, Germany; ²FSU Jena, Germany

A longitudinal density downramp as an injector for ultra-high intensity laser wakefield acceleration has been shown to produce quasi-mono-energetic electron beams [1, 2]. Rotating this sharp gradient is expected to cause an injection asymmetry resulting in more significant transverse betatron oscillations of the electron beam. An experiment to study the impact of asymmetric injection on betatron yield was conducted at JeTi200 [3]. Here we report on the PIC simulations done in support of the experimentally observed x-ray spectra.

In the simulation, performed using the particle-in-cell (PIC) code SMILEI [4] in the 2D geometry, a laser beam ($\lambda_0 = 800$ nm, $a_0 = 3$) is focused on the density profiles with a straight/rotated downramp shown in Fig. 1. The total plasma length was 4 mm with a ramp profile having a peak density twice the density in the acceleration section ($8.5 \times 10^{17} \text{ cm}^{-3}$).

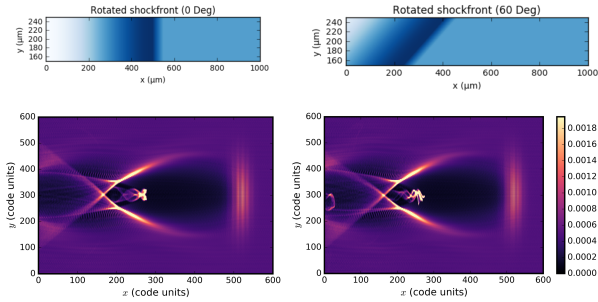


Figure 1: Upper: The simulated density profile for straight edge (left) and rotated edge (right). Lower: The corresponding simulated LWFA bubbles show axis-symmetric (left) and asymmetric injection (right).

The asymmetry in the injected beam stemming from asymmetric downramp injection can be seen clearly in the rotated shock front case's lower right panel of Fig. 1. As can be seen in Fig. 2, the magnitude of the mean transverse momentum $\langle p_y \rangle$ is clearly larger for larger shock rotation angles, showing higher beam asymmetries for larger shock rotation angles. However, the variance Δp_y^2 was similar in all the cases, indicating that the shock rotation excites collective betatron oscillations. Moreover, there was about ~ 15 % more beam charge with 10 % lower beam energy for the maximum rotation angle compared to zero rotation.

Finally, we calculated the emitted betatron radiation spectrum using SMILEI, shown in Fig. 3. Although there was an increase in $\langle p_y \rangle$ and the total injected charge for the rotated shock case, the decrement in dominating factor,

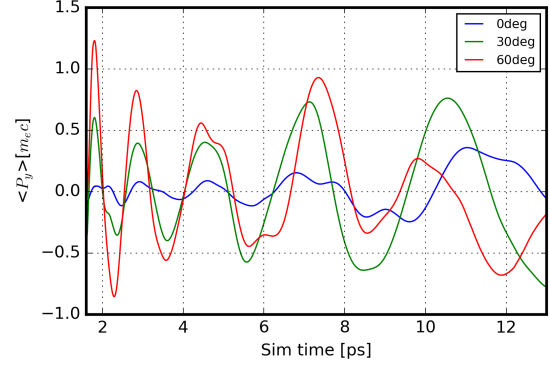


Figure 2: Temporal evolution of the mean transverse momentum $\langle p_y \rangle$ for different shock angles.

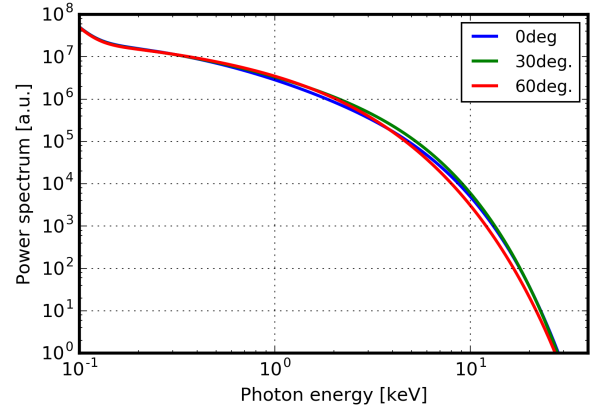


Figure 3: Spectrum of betatron radiation for three different shock angles having critical energy ≈ 6 keV.

γ (beam energy), lead to no significant change in betatron properties (as also seen in the experiment [3]). Further target optimization is required to keep the beam energy high when rotating the shocks, which will then produce brighter betatron x-rays.

The authors acknowledge funding from ESF, EU, TAB-FGR0074, and Freistaat Thüringen.

References

- [1] E. Esarey *et al.*, Phys. Rev. E **65**, 056505 (2002)
- [2] K. Ta Phuoc *et al.*, Phys. Plas. **15**, 063102 (2008).
- [3] H. Harsh *et al.*, HI Jena Annual Report 2021.
- [4] J. Derouillat *et al.*, Comput. Phys. Commun. **222**, 351 (2018).

^{*}harsh.harsh@uni-jena.de

PHOTON AND PARTICLE SPECTROSCOPY

Full 3-dimensional characterization of laser pulses with orbital angular momentum

Xinhe Huang^{1,2,3}, Alexander Sävert¹, Georg Schäfer¹, Beate Heinemann^{2,3}, and Matt Zepf^{1,4}

¹Helmholtz Institute Jena, Germany; ²DESY, Hamburg, Germany; ³Universität Freiburg, Germany; ⁴Friedrich-Schiller-Universität Jena, Germany

Laguerre-Gaussian laser beams with orbital angular momentum (OAM) are of interest for many experiments, e.g. the structured laser wakefields acceleration (LWFA) for positrons [1]. To confirm the far-field intensity distribution during the interaction with the target, we measure the electric field of the laser using the device INSIGHT[2]. Then the electric field can be fully reconstructed in three dimensions. The quality of the focal spot heavily depends on higher-order wavefront aberrations. Using a deformable mirror we can correct the wavefront distortions and achieve a flat wavefront. To finely tune the intensity distribution of the donut-shape focal spot, the influence of various wavefront aberrations was studied.

A laser pulse with OAM is generated using a helical-shaped wavefront achieved through a spiral phase plate (SPP). The SPP introduces an azimuthal dependence, $l\varphi$, to the electric field, resulting in a donut-shaped far-field intensity profile. Here, l denotes the azimuthal index and φ represents the azimuthal angle. The following Fig.1 depicts the configuration of an SPP and the resultant focal spot shape.

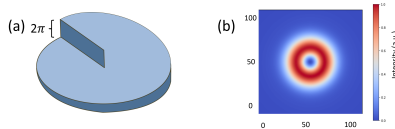


Figure 1: (a) The sketch of a spiral phase plate with a phase gap of 2π ($l = 1$). (b) The far-field intensity profile of a beam with OAM is in the shape of a donut.

However, the SPP is designed for a single wavelength, λ_0 , resulting in small variations in l for different wavelengths of an ultrashort laser pulse. This leads to an inhomogeneous intensity distribution in the focal spot. Moreover, the near-field intensity distribution and the position of the singularity point of the SPP along the laser transversal plane are crucial factors as well affecting the quality of the resulting focal spot. In our approach, we first optimize the laser focal spot using a wavefront sensor in a closed loop with a deformable mirror without the SPP to minimize the wavefront aberration down to an RMS value of 0.04λ . Then we finely tune the wavefront by applying higher-order Zernike terms upon inserting the SPP. Fig.2 shows the results on the focal spot using an F/21 focus geometry.

INSIGHT[2] is a three-dimensional reconstruction technique that combines spatially-resolved Fourier-transform spectroscopy and an alternate-projection phase-retrieval algorithm to obtain the electric field $E(x,y,\omega)$ of an ultrashort

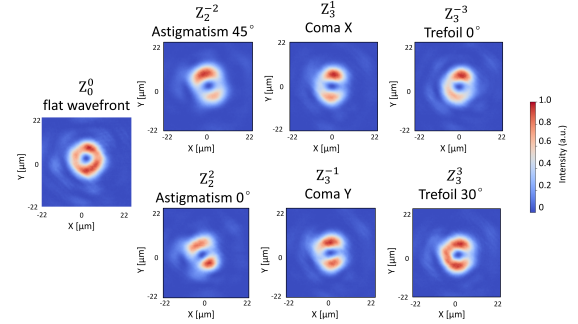


Figure 2: The figures demonstrate the influence of different aberrations, each characterized by a Zernike term with an amplitude of 0.5λ , on the shape of the focal spot.

laser pulse. It reconstructs both the phase and amplitude of the laser beam using a Michelson interferometer, where one path serves as the reference while the other path scans the delay with a piezo-driven mirror. Fig.3 presents the 3D reconstruction of the focal spot intensity $I(x, y, \lambda)$ for the pulse with OAM. The deviation from the expected donut shape is due to remaining aberrations and experimental imperfections, emphasizing the importance of future optimization and characterization.

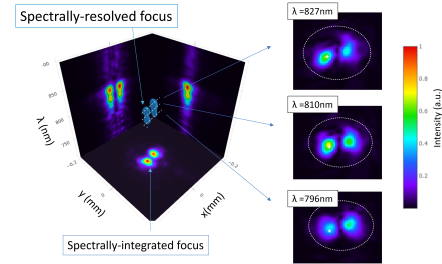


Figure 3: Spectrally resolved focal spot and the slice-out for individual wavelengths.

In conclusion, the feasibility of the optimization and 3D characterization of the laser pulse with OAM is demonstrated. Laser pulses with OAM can be applied to generate a structured wakefield suitable for positron acceleration. Additional diagnostics like few-cycle shadowgraphy and an exit mode diagnostic will be used to characterize the laser pulse at full energy.

References

- [1] J. Vieira and J. T. Mendonça, Phys. Rev. Lett. **112**, 215001 (2014).
- [2] A. Borot and F. Quéré, Opt. Express **26**, 26444-26461 (2018).

Enhanced Ghost Imaging by Illumination Pattern Optimization

T. Tian^{*1,2}, Z. Sun³, S. Oh^{1,2}, and C. Spielmann^{1,2}

¹HI Jena, Fröbelstieg 3, 07743 Jena, Germany; ²Institute of Optics and Quantum Electronics, Max Wien Platz 1, 07743 Jena, Germany; ³School of Artificial Intelligence, Optics and ElectroNics (iOPEN), Northwestern Polytechnical University, Xi'an 710072, P.R. China

Ghost imaging has great potential for a wide range of imaging scenarios. The quality of imaging results is strongly influenced by the speckle pattern used in the imaging process. Through the careful combination of patterns with different characteristics, we have optimized ghost imaging to enhance the quality of images and expand its potential applications to imaging in turbulent and turbid water.

Ghost imaging, also known as single-pixel imaging, is a revolutionary imaging technique that utilizes a single-pixel detector to generate images. This unique characteristic gives ghost imaging enormous potential in terms of imaging efficiency and resilience in harsh environments [1]. In single-pixel imaging, illumination patterns play a crucial role in generating high-quality images.

Contrast-to-noise rate (CNR) and resolution are used as criteria to evaluate the performance of ghost imaging. CNR is calculated from the signal and background intensity, then normalized to the noise [2].

Typically, an increase in pattern speckle size leads to an increase in CNR but a decrease in resolution. This led us to explore the potential benefits of combining different speckle sizes in ghost imaging. Through experimentation, we found that by combining speckles of varying sizes, we could achieve improved imaging performance in terms of both CNR and resolution. This novel approach to ghost imaging not only enhances image quality but also paves the way for ghost imaging microscopy.

By designing sophisticated illuminating patterns, we also explored the possibility of applying ghost imaging in harsh environment, particularly in the challenging scenario of underwater imaging. Turbidity and turbulence in water can pose significant challenges to traditional imaging techniques, making it difficult to capture clear and accurate images. To address this challenge, we developed a set of illuminating patterns that combine a Bessel beam with a random speckle pattern. The Bessel beam is non-diffractive and self-curable, which makes it ideal for use in challenging environments. By taking advantage of the shape of the Bessel beam and combining it with a random speckle pattern, we were able to achieve better ghost imaging results with an increased CNR. On average, this approach resulted in a 50% increase in CNR compared to using a random speckle pattern alone. Our experimental results demonstrated that this approach has significant potential for improving imaging performance in underwater imaging.

In summary, ghost imaging / single-pixel imaging has a

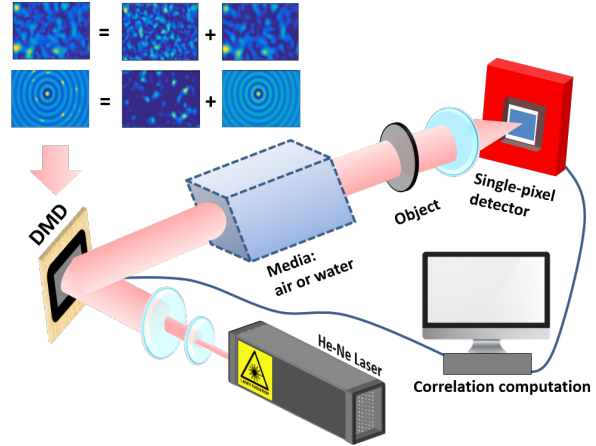


Figure 1: Experimental setup. Final ghost imaging results are obtained by the correlation computation of digital micromirror device (DMD) loaded patterns and values from single-pixel detector. Two sets of illumination patterns were used: one combining speckles of varying sizes with air as the medium between the DMD and the object, and the other using a Bessel pattern with water as the medium.

great expectation in various of imaging scenarios. Speckle pattern is the essential factor that determines the quality of imaging results. To explore and take advantage of the speckle pattern, we investigated the law of speckle pattern combination of different sizes and also the combination of Bessel beam ring. After experimental validation, it can be concluded that the proposed methods are capable of enhancing the final imaging results. The researches gave deep insight into ghost imaging and greatly expand the usage of ghost imaging techniques.

References

- [1] B. I. Erkmen *et al.*, Adv. Opt. Photon **2**, 405-450 (2010).
- [2] Z. Sun *et al.*, Opt. Express **27**, 33652-33661 (2019).

*tong.tian@uni-jena.de

Single pixel imaging using Hadamard and Fourier pattern

Sukyoon Oh^{*1,2}, Tong Tian^{1,2}, and Christian Spielmann^{1,2}

¹Institute of Optics and Quantum Electronics, Friedrich Schiller University Jena, D-07743 Jena, Germany; ²Helmholtz Institute Jena, Fröbelstieg 3, D-07743 Jena, Germany

Single pixel imaging (SPI) is a novel technique in imaging science that has garnered significant attention in recent years. Unlike traditional imaging methods, SPI captures information from an object with a single sensor. In this report, we will introduce different methods of SPI, which use differential Hadamard patterns and Fourier patterns.

Differential Hadamard Patterns: Hadamard patterns are a type of binary pattern that exhibit useful properties for SPI. Differential Hadamard patterns are generated by taking the difference between two Hadamard patterns, resulting in a new pattern with positive and negative intensity values. These patterns are used to sequentially illuminate the scene, and the transmitted light is measured using a single detector. The original image can be reconstructed using inverse Hadamard transformation. [1].

Fourier Patterns: Fourier patterns are another type of pattern used in SPI. They are based on the principles of Fourier transform, which is a mathematical technique used to analyze signals and images in the frequency domain. Fourier patterns are generated by modulating the intensity of a light source with sinusoidal functions of different frequencies and phases. The transmitted light is measured using a single detector, and the resulting data is analyzed to reconstruct the original image using inverse Fourier transformation. [2].

Experimental result and outlook: Our experiments are based on a computational ghost imaging setup using digital micromirror device (DMD), as shown in Figure 1. Figure 2 shows the reconstructed image using differential Hadamard pattern and Fourier pattern for a simple 2D material. The upper figure shows the SPI with differential Hadamard pattern. All values corresponding to the Hadamard spectrum of the original image are measured, and the original image is reconstructed using inverse Hadamard transformation. The lower figure shows the SPI with Fourier pattern. All values corresponding to the Fourier spectrum of the original image are measured, and the original image is reconstructed using inverse Fourier transform. SPI with differential Hadamard patterns and Fourier patterns offer several advantages over traditional imaging techniques. The main advantages of SPI is that the sequential illumination and measurement process allows for robust imaging in low-light conditions or lens-less imaging, making it suitable for applications in remote sensing, biomedical imaging, and imaging in challenging environments.

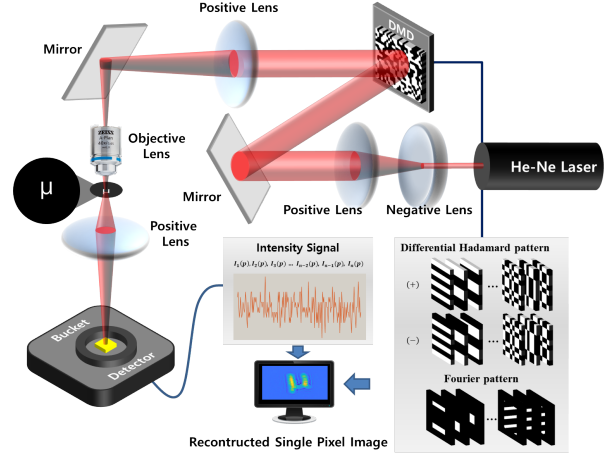


Figure 1: Conceptual diagram of the SPI system. A He-Ne laser beam is effectively collimated using a dual-lens system to generate different illumination patterns with the DMD. The transmitted intensity through the object is measured with a single pixel detector for different illumination patterns. The object is reconstructed by the correlation of the intensity signals and the sequenced patterns.

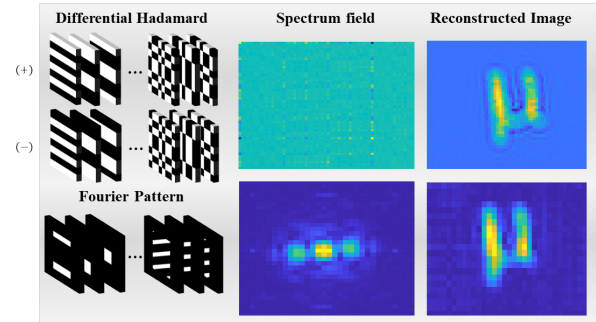


Figure 2: In the top row, SPI with differential Hadamard pattern is shown. The spectrum field displays the corresponding values of the original image of the object. Using inverse Hadamard transformation, the original image (character μ) is reconstructed with 512 measurements. In the bottom row, SPI with Fourier pattern is shown. The Fourier spectrum field is measured using Fourier pattern, and the original image is reconstructed using inverse Fourier transformation with 256 measurements.

References

- [1] F. Ferri *et al.*, Phys. Rev. Lett. **104**, 25 (2010).
- [2] Zhang, Zibang *et al.*, Optics Express **25**, 16 (2017).

*sukyoon.oh@uni-jena.de

Long Living Hot and Dense Plasma by Intense Laser-Nanowire Interaction

E. Eftekhari-Zadeh ^{*1,2}, P. Tavana^{1,3,4}, R. Loetzsch^{1,2}, I. Uschmann^{1,2}, T. Siefke⁵, T. Käsebier⁵, U. Zeitner⁵, A. Szeghalmi^{5,6}, A. Pukhov⁷, O. Rosmej^{3,4}, D. Kartashov¹, and C. Spielmann^{1,2}

¹IOQ, Friedrich Schiller University Jena; ²HI Jena, Fröbelstieg 3, 07743 Jena; ³GSI, Planckstr. 1, Darmstadt, Germany; ⁴IAP, Goethe University Frankfurt am Main; ⁵IAP, Friedrich Schiller University Jena; ⁶IOF, Albert-Einstein-Str. 7, 07745 Jena, Germany; ⁷ITP, Heinrich Heine University Düsseldorf,

Experimental results on relativistic laser-nanowire interaction suggest keV temperature and near solid density plasma existing on nanosecond time scale after the interaction. We assume that development of pinch and accompanying giant magnetic fields in nanowire array targets (NWs) significantly enhances Weibel instability, resulting in generation of magnetic fields with amplitudes above 100 T capable to trap very hot and dense plasma on many nanosecond time scale [1].

In the experiments, 0.7 J, 30 fs laser pulses at the 0.8 μm wavelength were frequency doubled, to enhance the temporal contrast, with the efficiency about 20% and focused normal to the target, reaching the intensities $\geq 3 \times 10^{19} \text{ W/cm}^2$. The targets were arrays of composite NWs with 100 nm Si core and 50 nm TiO_2 cladding, fabricated on a 50 μm thick Si membrane. As a reference, 25 nm thick layer of TiO_2 , deposited on a 50 μm thick Si membrane, was used. Energy spectra of protons, ejected from the front side of the targets, as well as the spectra of electrons from both, front and rear sides of the target, were measured with magnetic spectrometers. Two crystal spectrometers were used to measure X-ray spectra, generated in the target. A flat KAP crystal was used to measure the spectral intensities of different Si ions (up to H-like Si^{+13}) and a toroidal GaAs crystal was used to measure emission lines of Ti ions (up to H-like Ti^{+21}) and for 1D imaging of the emission source. Preliminary results of experimental campaign were reported in [1] and in Helmholtz Institute Jena Annual Report 2022.

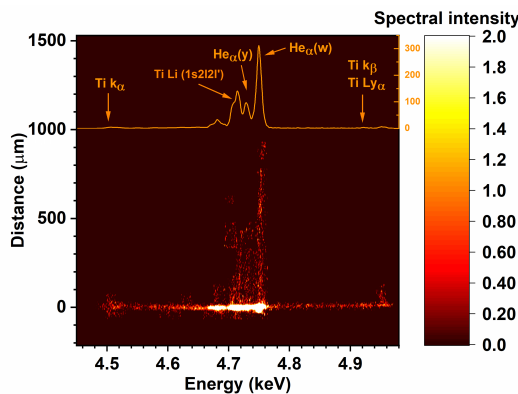


Figure 1: CCD X-ray image for nanowires providing 1D spatial imaging of the Ti X-ray source. Inset: spatially integrated X-ray spectrum

We observe significant (>3 times) increase in the energy

* e.eftekhari-zadeh@uni-jena.de

and the number of high energy protons generated at the front side of the target for NW morphology in comparison to the reference flat target. Moreover, our spectral imaging diagnostic shows that the source of $\text{K}\alpha$ emission lines from He-like Ti^{+20} ions, generated in NW arrays, has a shape of a jet extended up to 1 mm from the target surface (Figure 1). The comparison of the intensity of the He-like Ti ion emission at the target surface and in the jet, supported by the analysis of this emission using FLYCHK radiative kinetic code, suggests keV-level temperature and near solid density plasma in the jet. Corresponding estimates, based on the ionic speed of sound for plasma expansion into vacuum, suggest that such hot and dense plasma is sustained at several nanosecond time scale after the interaction with the laser pulse.

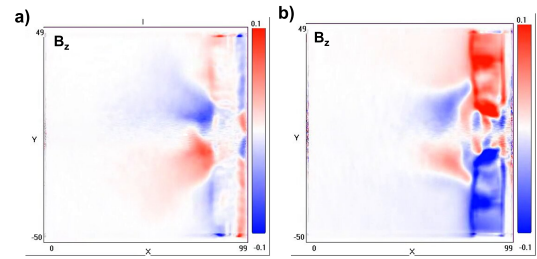


Figure 2: B-field pattern of flat (a) and NWs (b) generated 780 fs after the interaction of main pulse simulated by 2D particle-in-cell.

To get insight into the origin of the hot and dense plasma jet formation, 2D particle-in-cell (PIC) simulations for laser-target interaction were conducted. The simulations predict drastically different spatial structure of the magnetic field, generated in the plasma of a flat and NWs (Figure 2). Whereas for the flat target the magnetic field is concentrated on the plasma surface, for NWs the magnetic field fills the plasma volume. Therefore, we suggest that long living hot and dense plasma jets are formed due to strong (>100 T) magnetic fields, generated by Weibel instability. The instability is significantly enhanced for NW morphology due to the pinch effect [2] that leads to generation of giant magnetic fields and strong anisotropy at the early stage of plasma expansion.

References

- [1] E. Eftekhari-Zadeh *et al.*, Compact EUV & X-ray Light Sources. Optica Publishing Group, JTh6A.1 (2022).
- [2] V. Kaymak *et al.*, Phys. Rev. Lett. **117**, 035004 (2016).

Ellipticity Dependence of High Harmonic Generation in MoS₂ Monolayer

H.N. Gopalakrishna^{*1,2}, R. Hollinger¹, V. Korolev¹, A. George⁴, M. Zürch³, C. Spielmann^{1,2}, A. Turchanian⁴, and D. Kartashov¹

¹Institute of Optics and Quantum Electronics, Friedrich Schiller University, Max-Wien-Platz 1, 07743, Jena, Germany; ²Helmholtz-Institut Jena, Helmholtzweg 4, 07743 Jena, Germany; ³Department of Chemistry, University of California Berkeley, 237B Hildebrand Hall, Berkeley, CA 94720, USA; ⁴Friedrich Schiller University Jena, Institute of Physical Chemistry, 07743, Jena, Germany

We report on the results of experimental investigation on high-order harmonic generation in a MoS₂ monolayer when changing the laser polarization from circular to linear for different orientation of the polarization in respect to the symmetry axes of the crystal. Polarization analysis of harmonic emission reveals ellipticity and helicity dependent enhancement of even order harmonic intensity that is strongly asymmetric near the symmetry directions of the crystal.

The study of strong field-driven nonlinear responses from high harmonic generation (HHG) in two dimension (2D) materials has been recognised as a valuable tool for probing ultrafast electron dynamics in the condensed matter systems. The HHG in 2D-transition metal dichalcogenides (2D-TMDs) materials is an exciting and rapidly developing field of research that has the potential to revolutionise photonics and electronics. Recent advances in HHG from 2D-TMDs have demonstrated the ability to generate even and odd order harmonics through specific crystal orientations and laser polarizations [1, 2]. In this contribution we experimentally demonstrate that the polarization dependence of HHG in single layer TMD materials strongly depends on the orientation of the polarization ellipse in respect to the symmetry axes of the crystal and distinctly different for even and odd orders of harmonics.

The Harmonics were generated by 120 fs, 3.5 μm wavelength laser pulses with the intensity up to 1.3 TW/cm² in a monolayer of MoS₂. The laser polarization was controlled by broadband $\lambda/4$ and $\lambda/2$ waveplates, allowing for orientation of the polarization ellipse in respect to the crystal axes. The polarization components of the harmonic emission, parallel and orthogonal to the major axis of the laser polarization, were analyzed using a wire grid polarizer placed in front of the spectrometer.

We investigate the dependence of the polarization components in harmonics emission parallel and orthogonal to the pump polarization for different orientations of the polarization ellipse in respect to the symmetry axes of the crystal. The exemplary results for 10th order harmonic are shown in Fig.1. For even harmonics (6th, 8th and 10th) we observe that the parallel component of the harmonic field shows helicity independent intensity enhancement for the pump ellipticity ± 0.2 along the zigzag symmetry direction of the crystal (30° rotation angle in Fig.1a). Rotation of the crystal towards armchair direction results in helicity de-

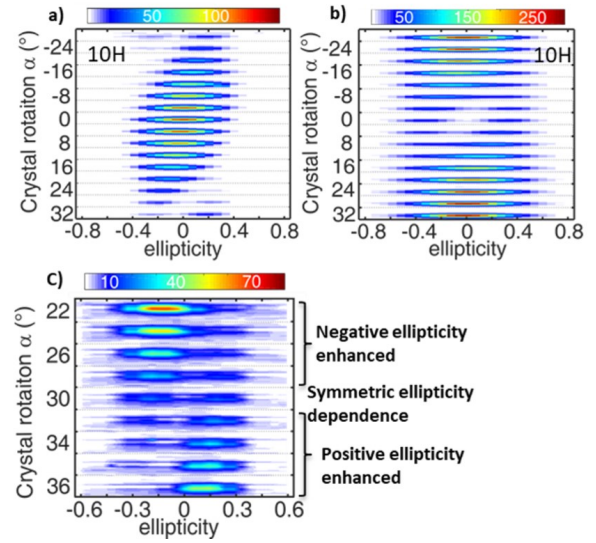


Figure 1: Figure 1. Ellipticity and orientation dependent intensity of 10th harmonic in the component, polarized a) parallel and b) orthogonal to the laser polarization. c) Zoomed region from a) around 30° crystal orientation angle (zigzag direction), showing transition from symmetric to strongly asymmetric ellipticity dependence

pendent enhancement with the maximum of the asymmetry between the negative and positive ellipticities for the crystal orientation $\approx 8^\circ$ from the zigzag direction (Fig.1c). The orthogonal component of the harmonic field shows similar behavior but with the symmetric enhancement for the armchair crystal orientation and maximum of the asymmetry $\approx 8^\circ$ from the armchair direction. Also, we observe that the helicity dependence in 8th harmonic has opposite sign to the helicity dependence of the 10th harmonic. Finally, odd order harmonics show no ellipticity enhancement for any orientation of the polarization ellipse in respect to the crystal symmetry axes.

References

- [1] H. Liu *et al.*, Nat. Phys., 262-265 **13**, 262-269 (2017).
- [2] N. Yoshikawa *et al.*, Nat. commun. **10**, 3709 (2019).

*harshitha.nandiga.gopalakrishna@uni-jena.de

Revealing the ultra-structure of microorganisms using table-top extreme ultraviolet ptychography

C. Liu^{*1,2}, W. Eschen^{1,2}, J. Limpert^{1,2,3}, and J. Rothhardt^{1,2,3}

¹HI Jena, Fröbelstieg 3, 07743 Jena, Germany; ²IAP, FSU Jena, Albert-Einstein-straße 15, 07745 Jena, Germany;

³IOF Jena, Albert-Einstein-Str. 7, 07745, Jena, Germany

We demonstrate position-correlated ptychographic EUV imaging of unstained, dried cells at 13.5 nm wavelength, which offers sufficient penetration depths for identifying intracellular features. By combining infrared and XUV illumination, we achieve a millimeter-squared field of view and sub-60 nm spatial resolution on selected regions of interest. The strong element contrast at 13.5 nm wavelength enables the identification of nanoscale material composition within specimens.

XUV microscopy offers unused potential in high-resolution imaging of biological tissues, complementing electron microscopy and fluorescence microscopy [1]. It combines such as nanometer-scale resolution, high absorption- and phase contrast, and penetration depths in the μm -scale range. Furthermore, atomic resonances across the periodic table in the XUV spectral region enable excellent material specificity, allowing investigation of cellular and sub-cellular features in microorganisms.

Here we demonstrate tabletop XUV ptychographic imaging of microorganisms at a wavelength of 13.5 nm (92 eV photon energy). The detailed setup and performance of this microscope have been previously described in a published article [2]. We investigated dried and unstained germinating conidia of the filamentous fungus *Aspergillus nidulans* as a model eukaryote system in a vacuum environment [3]. To locate interesting areas on the sample membrane, a fast ptychographic scan using the fundamental IR laser beam was performed to acquire an overview image of the entire membrane. This provided a large field of view (FOV) of 1 mm but with a relatively low resolution of 1.2 μm (Fig. 1 a, center graph). Selected regions of interest (ROIs) were then imaged using XUV ptychography, which provided complex transmission images of fungus clusters and single hyphen with a half-period spatial resolution of 58 nm (Fig. 1 a, XUV micrographs). The XUV images exhibited high absorption and phase contrast due to the large penetration depths at this wavelength. The reconstructed amplitude (Fig. 1 b) and unwrapped phase (Fig. 1 c) of the single hypha were used for calculating the scattering quotient (Fig. 1 d). The dominating components of sub-cellular units can therefore be recognized by referring to the scattering quotients calculated from tabulated atomic data [4].

In conclusion, we have developed a high-performance tabletop format XUV ptychographic microscope that provides unique capabilities for high-resolution, chemical-sensitive biological imaging. In the future, it appears feasible to combine the presented XUV ptychographic setup

with other microscopy techniques, such as light fluorescence microscopy, to provide information from multiple imaging modalities and uncover the overall chemical information and specific functional information of sub-cellular features in a single tabletop device. Our work advances XUV imaging applications and expands possibilities in life science.

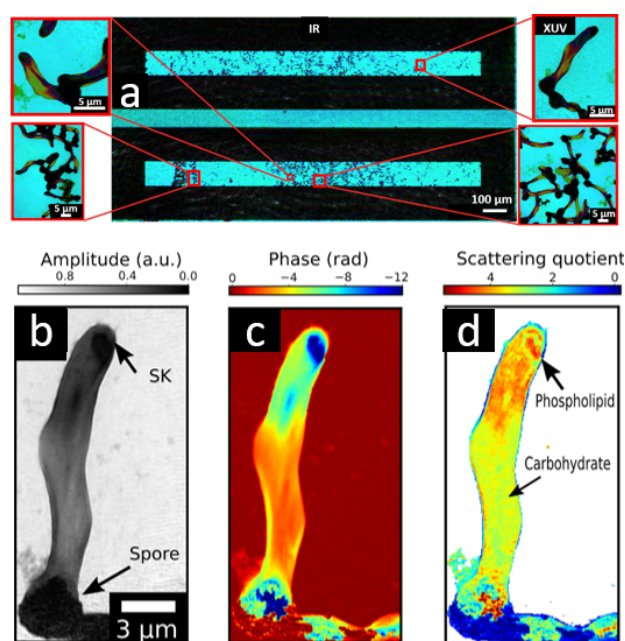


Figure 1: a. Reconstructed *A. nidulans* on a Si3N4 membrane using the fundamental IR beam (center) and XUV beam (micrographs). b, c, and d show the reconstructed amplitude, unwrapped phase, and scattering quotient map of a single fungi hypha respectively.

The research was supported by the Innovation Pool of the Research Field Matter of the Helmholtz Association of German Research Centers (project FISCOV), the Thüringer Ministerium für Bildung, Wissenschaft und Kultur (2018 FGR 0080), the Helmholtz Association (incubator project Ptychography 4.0), and the Fraunhofer-Gesellschaft (Cluster of Excellence Advanced Photon Sources)

References

- [1] J. Rothhardt *et al.*, J. Opt. **20**, 11 (2018).
- [2] W. Eschen *et al.*, Light Sci. Appl. **11**, 117 (2022).
- [3] C. Liu *et al.*, Photonix **4**, 6 (2023).
- [4] B. L. Henke *et al.*, At Data Nucl Data Table **54** 2 (1993).

* cliu@hi-jena.gsi.de

Table-top Nanoscale Material-specific Imaging at 13.5 nm Wavelength

W. Eschen^{*1,2}, C. Liu^{1,2}, D. Molina Penagos^{1,2}, R. Klas^{1,2,3}, J. Limpert^{1,2,3}, and J. Rothhardt^{1,2,3}

¹HI Jena, Fröbelstieg 3, 07743 Jena, Germany; ²IAP, FSU Jena Albert-Einstein-Str. 15, 07745 Jena, Germany;

³Fraunhofer Institute for Applied Optics and Precision Engineering IOF, Albert-Einstein-Str. 7, 07745 Jena, Germany

We demonstrate high-resolution extreme ultraviolet imaging with material-specific capabilities using a high-order harmonic source. A half-pitch resolution of 16 nm is demonstrated on a resolution test chart. Furthermore, the complex transmission of an integrated circuit is reconstructed. Specific materials like Silicon nitride and Silicon oxide are identified by analysis of the amplitude and phase images.

In recent years, advances in high-power and ultra-short laser technology have enabled bright EUV sources utilizing high-harmonic generation (HHG). When combined with modern coherent imaging modalities, such as ptychography, these sources facilitate the development of compact, high-resolution EUV microscopes that were previously limited to large-scale facilities. In this study, we demonstrate high-resolution, material-specific ptychographic imaging using a high-order harmonic source. The microscope is based on a high-power ytterbium-doped fiber laser system, which generates few-cycle pulses with 0.4 mJ pulse energy. These pulses are focused onto an Argon gas jet, generating a broad EUV continuum. To image the HHG source onto the sample, a Schiefspiegler telescope configuration consisting of three ML mirrors, which also select a wavelength of 13.5 nm from the broadband EUV continuum, is employed. For additional information on the ptychography setup utilized in this study, we direct the reader to our recent publication [1, 2].

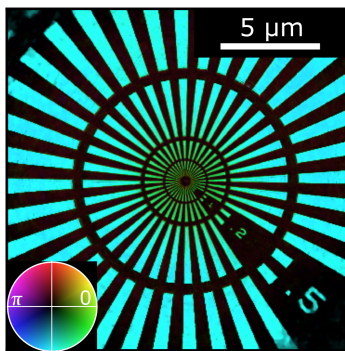


Figure 1: Reconstructed Siemens star. The brightness and hue correspond to the reconstructed amplitude and phase.

To demonstrate the advantages of our microscope two samples were investigated. In the first step, the resolution of the EUV microscope was characterized using a resolution test chart (Siemens star), which was scanned for 101 scan positions. At each position, the diffraction pattern was

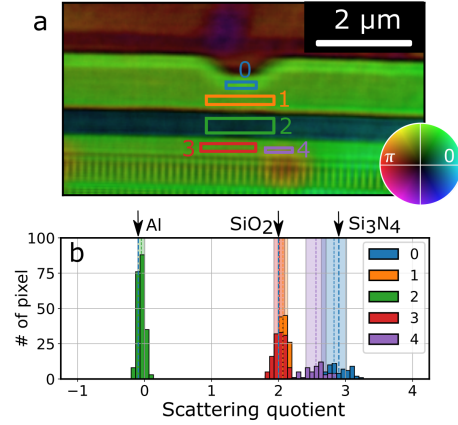


Figure 2: **a** Reconstructed complex transmission of an integrated circuit **b** Scattering quotient extracted from the regions indicated in **a**.

measured with an exposure time of 48 s. The resulting reconstruction of the sample is shown in Figure 1 and demonstrates a diffraction-limited resolution of 16 nm.

Next, we extracted a thin lamella from a commercially available solid-state drive and placed it in the EUV microscope. The resulting reconstruction (Figure 2 a) depicts the integrated circuitry of the memory module. A wide range of amplitude and phase values are evident, which can be attributed to the different materials used for the fabrication. To determine the materials present, the scattering quotient was calculated from the reconstructed phase and amplitude values [3]. Figure 2 b shows a histogram of the obtained scattering quotient for the regions indicated in Figure 2 a, which enables the identification of typical materials used in integrated circuits, such as Si_3N_4 , Al and SiO_2 , by comparison with known scattering quotient values.

In conclusion, high-resolution material-specific imaging was demonstrated for the first time on a lab-based setup. This promises metrology applications for a broad range of fields ranging from microbiology to material sciences.

The research was supported by the Helmholtz Association (FISCOV, Ptychography 4.0), the Thüringer Ministerium für Wissenschaft, Bildung und Kultur (2018 FGR 0080), and the Fraunhofer-Gesellschaft (CAPS).

References

- [1] R. Klas *et al.*, Opt. Express **28**, 6188 (2020).
- [2] W. Eschen *et al.*, Light Sci. Appl. **11**, 117 (2022).
- [3] M. Jones *et al.*, Sci. Rep. **4**, 1-4 (2014).

*wilhelm.eschen@uni-jena.de

Platform for combined heavy-ion high-energy-laser experiments

Zs. Major^{*1,2}, P. Hesselbach^{1,3}, P. Neumayer^{1,3}, B. Zielbauer¹, X. Yu¹, K. Weyrich¹, A. Tauschwitz¹, D. Varentsov¹, V. Bagnoud^{1,4}, R. Belikov³, B. Winkler³, J. Lütgert⁵, D. Kraus⁵, and D. Riley⁶

¹GSI, Darmstadt, Germany; ²Helmholtz-Institut Jena, Germany; ³Goethe Universität Frankfurt, Germany; ⁴TU Darmstadt, Germany; ⁵Universität Rostock, Germany; ⁶Queen's University Belfast, UK

Understanding the behaviour of warm dense matter (WDM), i.e. matter at temperatures of 1-10 eV and at pressures of 1-100 Mbar, is essential for planet modelling, as such conditions prevail in the interiors of many astrophysical objects. Such states of matter can be created in the laboratory using powerful drivers, albeit, their behaviour can be influenced by the kind of driver used to generate them. In contrast to shock-driven WDM, generated by high-energy nanosecond lasers, at GSI, Darmstadt, heavy ions represent an alternative type of powerful driver with the prospect of allowing for large volumes of WDM to be generated in uniform physical conditions in local thermal equilibrium on relatively long time scales [1]. Following previous studies at the HHT experimental area at GSI [2], we have recently equipped this experiment station with a beamline for the high-energy nanosecond laser pulse of PHELIX, allowing for laser-driven X-ray diagnostics on matter heated by the heavy-ion beam.

Laser-driven X-ray diagnostic methods are particularly suited for studying heavy-ion heated WDM, as they provide bulk information on changes in the structure of the sample (e.g. X-ray diffraction) and/or information on the temperature (e.g. X-ray Thomson Scattering or X-ray absorption spectroscopy). Fig. 1 shows the experimental

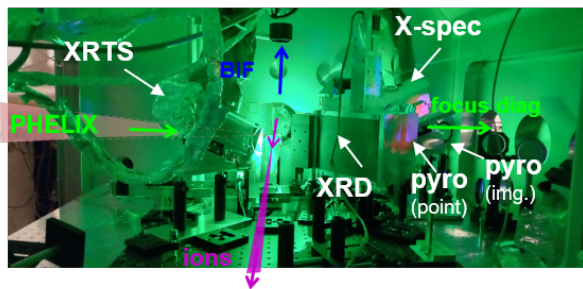


Figure 1: Experimental setup in the HHT target chamber.

setup in the HHT target chamber of our recent commissioning experiment. A suite of diagnostics was used for the investigation of heavy-ion-heated states of matter. The ion number and temporal shape of the ion pulse were recorded by using a fast current transformer (not shown in picture). The spatial size at the best focussing condition was determined by using beam-induced fluorescence (BIF) in Ar gas and optical transition radiation in an Al foil (not shown here). Two different pyrometry setups were used for temperature measurement. A multi-channel setup gives precise

temperature information from one point on the target, while the other provides spatial resolution by imaging the thermal emission in two spectral channels. PHELIX delivered 2-ns-long pulses with 200 J of energy at 527 nm, focussed with an F/13 lens for the X-ray generation. These pulses impinging on Ti and Cr backlighter foils resulted in He- α line emission at 4.75 keV and 5.68 keV, respectively. In an elaborate target assembly the X-rays then propagated to the target that was heated by the heavy-ion beam, where they were scattered and diffracted. The generated X-ray spectrum (X-spec), the X-ray Thomson scattering (XRTS), and X-ray diffraction (XRD) signals were recorded.

In this first experiment using both the heavy-ion beam and the PHELIX laser pulses, we investigated the effect of heavy-ion heating on diamond and iron. While the detailed analysis is still ongoing, Fig. 2 shows XRD and XRTS data demonstrating that we are clearly able to resolve diffraction/scattering signals above the background mainly caused by the heavy-ion beam itself, thereby demonstrating the capability to obtain structural and temperature information.

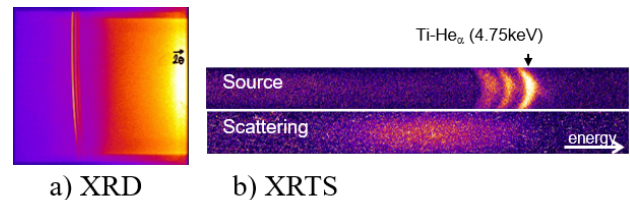


Figure 2: Preliminary X-ray diffraction and X-ray Thomson scattering images using Ti as backlighter and diamond as the target.

In conclusion, our diagnostic suite at HHT now includes laser-driven X-ray capabilities that have been successfully applied in a first proof-of-principle combined heavy-ion high-energy laser experiment. While the methods themselves were proven to work, the limitation in available heavy-ion intensity has so far prevented us from entering the interesting WDM regime. This limitation is expected to be overcome by the upcoming FAIR facility, where we will apply the diagnostic methods that we have developed during the ongoing FAIR phase-0 programme.

This research was supported by BMBF ErUM-FSP APPA. The presented results are based on the FAIR phase-0 experiment S489.

References

- [1] K. Schoenberg *et al.*, Phys. Plasmas. **27**, 043103 (2020).
- [2] D. Varentsov *et al.*, Nucl. Instrum. Methods Phys. Res. A **577**, 262 (2007).

*z.slattery-major@gsi.de

Scanning high-sensitive x-ray polarization microscopy

B. Marx-Glowna^{*1,2}, B. Grabiger³, R. Löttsch³, I. Uschmann^{1,2,3}, A.T. Schmitt³, K.S. Schulze^{1,2}, A. Last⁴, T. Roth⁵, S. Antipov⁶, H.P. Schlenvoigt⁷, I. Sergeev⁸, O. Leupold⁸, R. Röhlberger^{1,2,8}, and G.G. Paulus^{1,2,3}

¹Helmholtz Institute Jena, Fröbelstieg 3, 07743 Jena, Germany; ²Helmholtz Centre for Heavy Ion Research (GSI), Planckstr. 1, 64291 Darmstadt, Germany; ³Institute of Optics and Quantum Electronics, Friedrich Schiller University Jena, Max-Wien-Platz 1, 07743 Jena, Germany; ⁴Institute of Microstructure Technology, Karlsruhe Institute of Technology, Hermann-von-Helmholtz-Platz 1, 76344 Eggenstein-Leopoldshafen, Germany; ⁵European Synchrotron Radiation Facility, B. P. 220, 38043 Grenoble Cedex, France; ⁶Euclid TechLabs LLC, Bolingbrook, 60440 IL, United States of America; ⁷Helmholtz-Zentrum Dresden-Rossendorf, Bautzner Landstr. 400, 01328 Dresden, Germany; ⁸DESY Photon Science, Notkestr. 85, 22607 Hamburg, Germany

Polarization microscopy is one of the most fundamental and important examination methods in the visible range for structural investigations. For the first time, we have succeeded in realizing this methodology in the hard X-ray range. We could achieve a suppression of the π -polarization component by 11 orders of magnitude, allowing outstandingly sensitive polarization measurements. We have found the first X-ray lenses that do not influence polarization and have shown that conventional x-ray lenses cannot be used for high-precision polarimetry.

For the realisation of an X-ray polarization microscope we combined X-ray polarimetry with scanning microscopy. High precision X-ray polarimeters are based on Bragg reflections close to 45° . For these angles, the polarization component parallel to the diffraction plane (π -component) is suppressed. In order to improve the suppression of the π -component further, a channel is cut into the crystal to realise multiple reflections at 45° (see Fig. 1, polariser). Such a channel-cut crystal enables a suppression of the π -component versus the σ -component of up to 11 orders of magnitude [1]. As the magnitude of the polarization purity depends on the divergence of the X-ray source, an X-ray polarization microscope requires close to perfect recollimation after focusing the X-ray beam. Both, focusing and recollimation, must take place between polarizer and analyzer crystal. Therefore, it is important that the focusing optical elements do not impair polarization. We used compound refractive lenses (CRLs) as focussing and collimation elements. They are based on the refraction of X-rays. There are several refractive lens materials available. Their manufacturing process and material properties differ, which influences the achievable focal sizes and thus the spatial resolution of the polarisation microscope.

The X-ray polarization microscope was realized at beamline P01 of the synchrotron PETRA III (DESY) in Hamburg. Fig. 1 shows the experimental setup of the polarization microscope: Four different lens materials were evaluated for the suitability for polarization microscopy: Single-crystal diamond lenses, polycrystalline beryllium lenses, amorphous polymer lenses (SU-8), and glassy car-

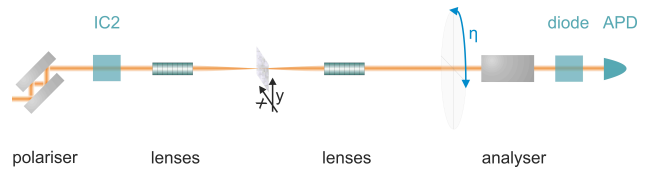


Figure 1: Experimental setup of the x-ray polarisation microscope. Silicon channel-cut crystals are used to polarise and analyse the beam. Two lens stacks are placed in between the crystals to focus and collimate the beam. Ionization chambers (IC), a diode and avalanche photodiodes (APD's) are used for detection.

bon lenses. We succeeded in realizing a highly sensitive polarization microscope with the polymer lenses. With a polarisation purity of 10^{-11} of the incoming beam, no change of the polarisation purity was measurable. The achieved focus size was $(7 \times 28) \mu\text{m}$. The performance of the polarimeter was demonstrated by scanning a beryllium foil of $500 \mu\text{m}$ thickness through the focus of the polarized beam. The result shows intensity changes of 2.5 orders of magnitude. The range of intensity change correlates with the crystallite size of the sample material, indicating that the polarization change is caused by Bragg reflections of the crystallites. Compared to X-ray polarimetry alone, polarization microscopy makes it possible to observe polarization changes with high spatial resolution. Knowing the spatial extension of polarisation-changing materials can strongly facilitate conclusions about their origin.

The successful combination of highly sensitive X-ray polarimeters with polarisation-preserving X-ray lenses is a new method that makes polarisation changes visible on the μm -scale and has the potential to result in new insight in many disciplines.

References

- [1] B. Marx-Glowna *et al.*, New. J. Phys. **24**, 053051 (2022).

*B.Marx-Glowna@hi-jena.gsi.de

A Novel Compton Telescope for Polarization Measurements up to 1 MeV

W. Middents^{*1,2,3}, G. Weber^{1,2}, U. Spillmann², T. Krings⁴, and Th. Stöhlker^{1,2,3}

¹HI Jena, Fröbelstieg 3, 07743 Jena, Germany; ²GSI Darmstadt, Planckstr. 1, 64291 Darmstadt, Germany; ³IOQ, FSU Jena, 07743 Jena, Germany; ⁴FZ Jülich, 52425 Jülich, Germany

In the hard x-ray regime from several 10 keV up to a few MeV, a characterization of the (linear) polarization of a photon beam can be performed via Compton polarimetry. Within the SPARC collaboration a precise Compton polarimeter based on a double-sided segmented planar Si(Li) detector was designed which is optimized for polarimetry experiments in the energy range of 60-200 keV. A double-sided segmented HPGe detector added in a telescope configuration to the existing Si(Li) detector will allow to extend the energy range to 1 MeV. In this Compton telescope configuration the Si(Li) detector will be used as scatterer and the HPGe detector as absorber detector.

The applied method to characterize the photon polarization highly depends on the energy regime. For photon energies in the hard x-ray regime, i.e. for several 10 keV up to a few MeV, polarization measurements rely on the anisotropy of the Compton scattering distribution with respect to the polarization direction of the incident radiation. This method is described in more detail in [2].

Recently, a detector was developed and commissioned within the SPARC collaboration with an spectral resolution of about 1 keV FWHM at a photon energy of 60 keV [3]. This setup is optimized for polarimetry in an energy range of about 50–200 keV. This detector consists of a lithium diffused silicon (Si(Li)) crystal (see Figure 1, left side) with a thickness of about 9 mm. Both the front and back contact of the detector are segmented into 32 strips with a width of 1 mm each. The strips of the front and back contact are oriented perpendicular to each other and are each connected to individual readout electronics, thus generating a grid with a 1024 quasi pixel structure on the active area of 32 mm × 32 mm. The crystal is cooled with LN₂ in operation. For an improved energy resolution, the first stage of the preamplifiers (FETs) are also mounted in the cryogenic environment on the crystal holder. This ensures both a short connection from the detector segments to the FETs and a reduced operating temperature of the FETs. The described setup was used as Compton polarimeter in multiple experiments at storage ring and at synchrotron facilities (e.g. in [4]).

In a second stage, this detector is currently being equipped with an additional segmented high-purity Germanium (HPGe) crystal (see Figure 1, right side). This HPGe crystal will be mounted behind the already existing Si(Li) crystal in a telescope structure. A design sketch of this detector setup can be found in Figure 2. The HPGe crystal has a thickness of about 15 mm and is segmented similar to the

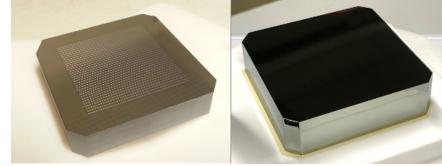


Figure 1: The used semiconductor crystals in the Compton telescope. Left: Si(Li) crystal. Right: HPGe crystal.

Si(Li) crystal into a strip structure on the front and back contact into 32 strips each, generating a structure of 1024 quasi pixels. Each of these strips has a width of 1.4 mm and a length of 44.8 mm. Similar to the Si(Li) crystal, the first stages of the preamplifiers for the HPGe crystal will be mounted on the crystal holder.

In this detector setup, the Si(Li) crystal serves as a scatterer and the HPGe crystal as an absorber of the Compton scattered photons. This setup will extend the energy range of the existing Si(Li) Compton polarimeter to allow for polarization measurements up to about 1 MeV. Additionally, exploiting the additional spatial information, this detector can serve as a Compton imaging system.

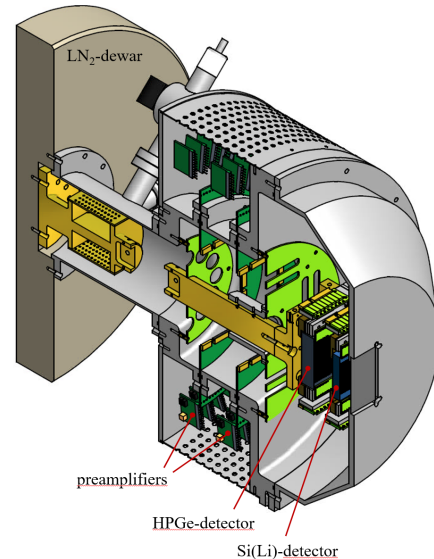


Figure 2: Design of the Compton telescope [3].

References

- [1] F. Lei *et al.*, Space Sci. Rev. **78**, 309 (1997)
- [2] M. Vockert *et al.*, NIM B **408**, 313(2017)
- [3] W. Middents *et al.*, Ann. Phys. **534**, 2100285 (2022)
- [4] M. Vockert *et al.*, PRA **99**, 052702 (2019)

*w.middents@hi-jena.gsi.de

High Resolution X-Ray Studies of Fe Using a Micro-Calorimeter Detector

M.O. Herdrich^{*1,2,3}, D. Hengstler⁴, A. Fleischmann⁴, C. Enss⁴, T. Morgenroth³, S. Trotsenko³, G. Weber³, R. Schuch⁵, and Th. Stöhlker^{1,2,3}

¹HIJ, Jena; ²IOQ, FSU Jena; ³GSI, Darmstadt; ⁴KIP, RKU Heidelberg; ⁵MSI, University Stockholm, Sweden

We report on first results of a high precision measurement conducted at the S-EBIT-I electron-beam ion-trap at GSI involving the interaction of an Fe ion-cloud with an electron-beam at 10 keV beam-energy. The resulting characteristic x-ray radiation from different charge states of Fe was recorded using a cryogenic calorimeter detector. The individual lines were identified and their intensity was determined to estimate the charge state distribution of Fe-ions in the trap.

Due to their unique working principle metallic-magnetic calorimeters (MMCs), like the *maXs*-series detectors developed within the SPARC collaboration, combine several advantages over conventional x-ray spectrometers (see for example [1]). With a high energy resolution in a broad spectral range they are expected to become a valuable tool for spectroscopy experiments involving highly charged ions. Therefore, in the recent years several *maXs*-detectors have been deployed at different storage ring and ion-trap facilities of GSI/FAIR, in order to test the feasibility of using MMCs for high-precision measurements in atomic physics. Following, we will present first results of one such experiment [2].

The experiment was conducted at the cryogenic *S-EBIT-I* electron-beam ion-trap (EBIT). Chemically bound iron-atoms in form of gaseous *Ferrocene* were injected into the trap volume where they were collided with a focussed electron beam at 10 keV beam-energy and up to 25 mA current. The x-ray radiation resulting from the continuous interaction of electrons with Fe-ions was recorded through the 90°-Port of the EBIT using a *maXs*-30 spectrometer detector. For the calibration of the energy-axis of the yielded spectra, an ²⁴¹Am source was positioned opposite of the micro-calorimeter (radiating through the EBIT).

K-shell vacancy production by Coulomb excitation and ionization in the Fe-ions lead to the subsequent transitions of L-shell electrons accompanied by the emission of $K\alpha$ x-ray photons. Due to shielding effects of the nuclear charge by remaining electrons, the observed transition energy thereby depends on the charge state of the involved Fe-ion ranging from 6.4 keV for neutral Fe up to 7.0 keV for H-like Fe. In parallel, radiative recombination (RR) of electrons from the electron beam competes with the electron loss through ionization resulting in a beam-energy, -current, and trapping-time dependant charge state equilibrium. Fitting the recorded spectrum to a model containing all identified transition lines, one can estimate the charge state distribution of Fe-ions in the trap by comparing the obtained peak intensities (see Fig. 1).

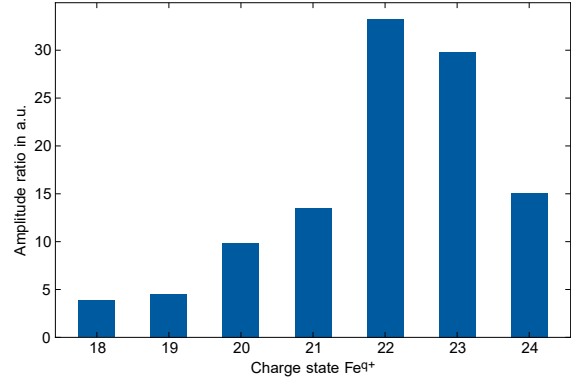


Figure 1: The figure shows an estimation of the charge state distributions of Fe-ions in the S-EBIT-I after a long trapping time.

While the L-shell ionization cross-section is slightly larger than for the L-RR-process (for the selected experiment parameters) – resulting in a slow accumulation of highly charged Fe-ions over time – the K-shell ionization cross-section is orders of magnitude lower. Thus, almost no radiation from charge states above Fe²⁴⁺ is expected. However, because of high voltage spikes in the EBIT the timing control of the trap stopped working and the trap remained closed for a long period of time. This not only explains the shift of the charge state distribution towards high charge states, but also the contamination of the spectra by a multitude of transitions from significantly heavier barium-ions (stemming from the cathode material).

In conclusion, the high energy resolution and broad bandwidth of the used *maXs*-detector made the simultaneous observation of separated transition lines from mixed Fe- and Ba-ions possible. Furthermore, during the experiment, the detector was operated for more than nine months with almost no maintenance or down-time. This is particularly interesting for experiments at beam-lines with limited access like the recently conducted measurement at CRYRING@ESR [3]. Overall, MMCs have proven to be a promising tool for future high-precision experiments in fundamental physics research.

We acknowledge financial support by the European Union and the federal state of Thuringia via Thüringer Aufbaubank within the ESF project (2018 FGR 0080).

References

- [1] J. Geist, Ph.D. Thesis, RKU Heidelberg (2020)
- [2] M.O. Herdrich *et al.*, X-Ray Spectrom. **49**, 184-187 (2020)
- [3] Ph. Pfäfflein *et al.*, Phys. Scr. **97**, 0114005 (2022)

*m.o.herdrich@hi-jena.gsi.de

Simulation of the photopeak efficiency of microcalorimeters equipped with small-volume gold absorbers

G. Weber^{*1,2}, P. Pfäfflein^{1,2,3}, F. Kröger^{1,2,3}, M. O. Herdrich^{1,2,3}, D. Hengstler⁴, A. Fleischmann⁴, and Th. Stöhlker^{1,2,3}

¹Helmholtz Institute Jena, Germany; ²GSI, Darmstadt, Germany; ³IOQ, FSU Jena, Germany; ⁴KIP, Heidelberg University, Germany

Precision spectroscopy of hard x-rays is expected to significantly profit from the development of metallic magnetic microcalorimeters (MMC). Such detectors combine a high spectral resolution, similar to crystal spectrometers, with a broad bandwidth acceptance that is comparable to semiconductor detectors. In general, the necessity for a small heat capacity to achieve the best possible spectral resolution needs to be balanced against an acceptable stopping power for x-rays within the energy range of interest. In the present report we simulate the photopeak efficiency of the maXs-100 detector system that was recently employed for the first time at CRYRING@ESR.

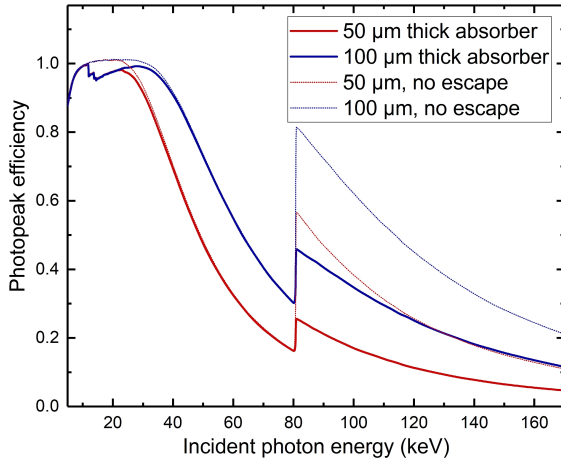


Figure 1: Photopeak efficiency simulated for two different thicknesses of gold absorbers

The full-energy peak efficiency or photopeak efficiency of a detector system is defined as the ratio of the number of counts within a given the photopeak to the number of photons of the same energy impinging on the active area of the detector. Thus, the photopeak efficiency is a measure of the detector's ability to measure the complete energy of an impinging photon. This quantity is determined by the probability of interactions which result in energy deposition by the photon in combination with the probability that a part of this energy is not recorded by the detector.

In the x-ray regime, such losses of energy are usually caused by secondary photons that escape from the detector volume. This can happen either when after an Compton scattering event within the detector, the scattered photon is

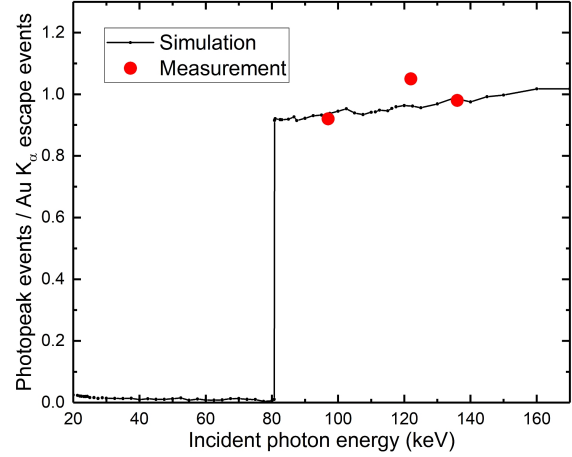


Figure 2: Verification of the simulation for the 50 μm thick absorber using experimental data.

leaving or when, after the creation of inner-shell vacancies, fluorescence photons are escaping. While the former result in a broad spectral feature, referred to as the Compton continuum, the latter results in distinct additional peaks in the spectrum, referred to as escape peaks. Small-volume detectors made of materials with high atomic numbers Z (and therefore high fluorescence yields), such as microcalorimeters, are particular prone to these energy loss processes.

In the present report we simulate the photopeak efficiency of gold absorbers of 50 μm and 100 μm thickness as they are used for the maXs-100 detector, which was recently employed at a first experiment at CRYRING@ESR [1]. The result is presented in figure 1, where for illustrative purposes we turned the effect of escape events on and off. It is found that escape events lead to a significant decrease in the photopeak efficiency as it is expected for such thin absorbers of high- Z materials. To verify the output of the simulation, in figure 2 the fraction of expected photopeak events to events in the corresponding K_{α} escape peaks is plotted for the 50 μm thick absorbers as a function of the incident photon energy and the simulation is compared to experimental data for gamma lines stemming from ^{153}Gd and ^{57}Co . Reasonable agreement is found.

This research was conducted in the framework of the SPARC collaboration. We acknowledge support by ErUM FSP T05 - "Aufbau von APPA bei FAIR" (BMBF grants 05P19SJFAA and 05P19VHFA1).

[1] P. Pfäfflein *et al.*, Phys. Scr. **97**, 114005 (2022).

*g.weber@gsi.de

Improvements in background reduction of metallic magnetic calorimeter data by means of a coincidence scheme

Ph. Pfäfflein^{*1,2,3}, M. O. Herdrich^{1,2,3}, G. Weber^{1,2}, and Th. Stöhlker^{1,2,3}

¹HI Jena, Fröbelstieg 3, 07743 Jena, Germany; ²GSI, Darmstadt; ³IOQ, FSU Jena

Recently, a first X-ray spectroscopy study using novel magnetic metallic calorimeters (MMC) has been performed at CRYRING@ESR. Besides the spectral information we are also interested in the time information provided by the detectors. The latter can be utilized to suppress background radiation via a coincidence measurement scheme. However, this was never demonstrated with MMC detectors. During the last year, the performance of two different trigger filter algorithms for the detector pulses has been studied. Here we present the achieved progress in the analysis of the detectors timing capabilities and the resulting background suppression. This study revealed opportunities to further improve the efficiency of the technique for future measurements using MMC detectors.

In 2021 two MMCs [1] have been used to study the X-ray emission of He-like Uranium at the electron cooler of CRYRING@ESR. A detailed description of the experimental study can be found in [2]. Following last year's effort of demonstrating a coincidence measurement using MMCs, this year we studied the background suppression performance in detail. Two challenges had to be overcome: The data acquisition scheme necessitated a software based trigger scheme and the slow signal rise time of MMC signals – compared to semiconductor detectors – needed to be taken into account. This was achieved by the implementation of a software trigger based on the concept of a constant fraction discriminator (CFD) [3]. Emphasis will be given to a comparison with the previously used trigger algorithm, a leading edge discriminator (LED) with an adaptive threshold. The extensive analysis can be found in [4]. The originally implemented LED was used to identify and suppress multi-photon events in a single signal trace. It is a very robust method for this purpose. A severe disadvantage of said trigger is the strong dependence of its timing result on the signal height which it analyses. As the expected photon energies span more than one order of magnitude, i.e. 5 keV to 100 keV, this will lead to non-optimal background suppression. For that reason the CFD was implemented as its timing dependency on the signal height is minimal by design.

The resulting background reduction for each trigger algorithm is displayed in figure 1. For the LED a 5 μ s wide coincidence condition had to be chosen in order to include the entire spectrum resulting in a background reduction by a factor of 12. In contrast the CFD allowed for a much narrower coincidence window of just 800 ns. With this even an 80-fold reduction in background photons can be

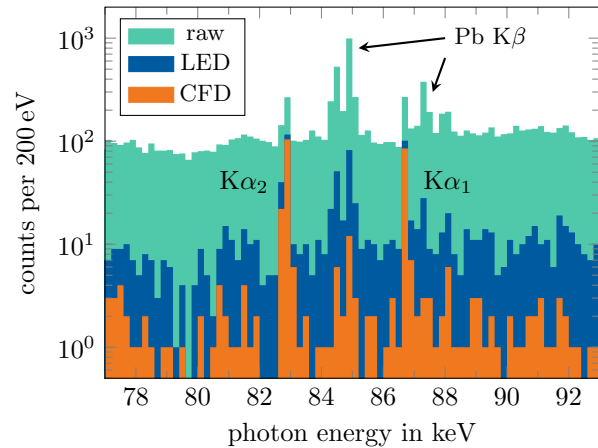


Figure 1: Spectra of the recorded X-ray emission from the CRYRING electron cooler. Raw: all events recorded from the accelerator; LED: with coincidence condition applied according to the previously common leading edge trigger; CFD: with coincidence condition applied according to the constant fraction trigger.

observed. However, Focusing on the signal to noise ratio as max peak height in the spectrum compared to average background height, the improvement is around a factor of 30. This leads to the conclusion that more than half of the photons of interest are also suppressed by the coincidence condition. Judging from a TOF spectrum an improvement in the signal height is not expected by choosing a wider window. As the photons are present in the raw spectrum, a suboptimal efficiency of the particle detector is likely the cause for the signal loss. This challenge is currently addressed by colleagues from GSI.

This research has been conducted in the framework of the SPARC collaboration, experiment E138 of FAIR Phase-0 supported by GSI.

References

- [1] D. Hengstler *et al.*, Phys. Scr. **T166**, 014054 (2015).
- [2] Ph. Pfäfflein *et al.*, Phys. Scr. **97**, 114005 (2022).
- [3] D. A. Gedcke *et al.*, Nucl. Instr. and Meth. **55**, 377-380 (1967).
- [4] Ph. Pfäfflein *et al.*, Atoms **2023**, 11, 5 (2022).

*p.pfaefflein@hi-jena.gsi.de

High-Resolution Microcalorimeter Measurement of N, M \rightarrow L transitions in U^{90+} at CRYRING@ESR

F.M. Kröger^{*1,2,3}, S. Allgeier⁴, Z. Andelkovic¹, S. Bernitt^{3,2,1}, A. Borovik⁶, L. Duval⁷, A. Fleischmann⁴, O. Forstner^{1,2,3}, M. Friedrich⁴, J. Glorius¹, A. Gumberidze¹, Ch. Hahn^{1,2}, F. Herfurth¹, D. Hengstler⁴, M.O. Herdrich^{1,2,3}, P.-M. Hillenbrand¹, A. Kalinin¹, M. Kiffer^{1,2,3}, T. Köhler³, M. Kubullek³, P. Kuntz⁴, M. Lestinsky¹, B. Löher¹, E.B. Menz^{1,2,3}, T. Over^{1,2,3}, N. Petridis¹, Ph. Pfäfflein^{1,2,3}, S. Ringleb^{1,2,3}, R.S. Sidhu⁴, U. Spillmann¹, S. Trotsenko^{1,2}, A. Warczak⁵, G. Weber^{1,2}, B. Zhu^{1,2,3}, C. Enss⁴, and Th. Stöhlker^{1,2,3}

¹GSI, Darmstadt, Germany; ²HI Jena, Germany; ³IOQ, FSU Jena, Germany; ⁴KIP, Heidelberg Univ., Germany;

⁵Jagiellonian Univ., Krakow, Poland; ⁶I.PI, Gießen Univ., Germany; ⁷LKB, Univ. Paris Sorbonne, Paris, France

Precision x-ray spectroscopy of highly-charged heavy ions is often limited by the spectral resolution achievable by the established detection technology, i.e. semiconductor detectors. While crystal spectrometers can overcome this limitation, their applicability is usually limited to a narrow window of photon energies for which the specific spectrometer was designed and in addition these instruments suffer from a high sensitivity to uncertainties in the geometry of the experimental setup. To achieve an excellent spectral resolution over a broad range of x-ray energies, novel microcalorimeter detectors were recently developed within the SPARC collaboration. Two of such detectors were used in a first experiment at the CRYRING@ESR, which allowed to measure x-ray spectra of transitions in U^{90+} with unprecedented resolution.

The experiment was conducted at the electron cooler of the CRYRING@ESR at GSI, in Darmstadt [1]. Here U^{91+} ions stored at a beam energy of 10.225 MeV/u captured cooler electrons into excited states, followed by rapid radiative decay cascades towards the ground state. The photon emission from the electron cooler region was recorded under 0° and 180°, using two novel metallic magnetic calorimeter (MMC) detector systems [2]. In addition, behind the dipole magnet downstream from the electron cooler a particle counter was placed in the beam line, so that ions which had recombined with cooler electrons and thus changed their charge state were detected. Combining the timing information from the particle detector and the MMC detectors for the first time allowed to set a coincidence condition for background suppression of spectral data recorded with MMC detectors [3].

This newly available detector setup together with the recently commissioned storage ring CRYRING@ESR successfully allowed to measure x-ray spectra with a resolution below 100 eV FWHM at 100 keV incident photon energy, comparable with the resolution of the FOCAL transmission crystal spectrometer [4]. Figure 1 displays a comparison of a resulting spectrum to a similar spectrum obtained with a Ge(i) x-ray detector at the electron cooler of the ESR at an ion beam energy of 43.59 MeV/u [5]. This result together with the broad spectral acceptance down to

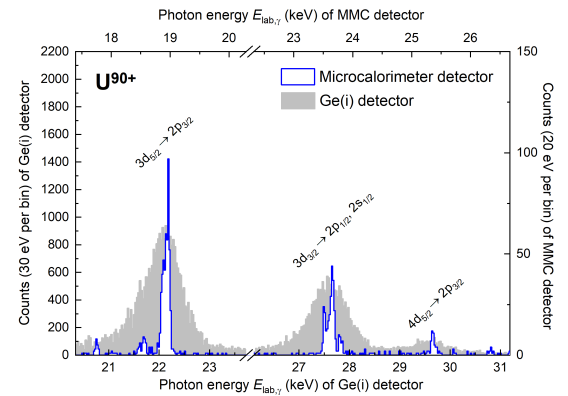


Figure 1: N, M \rightarrow L transitions in U^{90+} recorded with a MMC detector at the CRYRING@ESR electron cooler in comparison to data previously recorded by a Ge(i) detector at the ESR electron cooler [5].

a few keV of the MMC detectors does not only allow to determine the Doppler shift from the spectra itself [6], but will also enable us to deduce for the first time for such a highly-charged heavy system information on the relative population of the states in the L, M and N shells during the cascading of electrons into the ground-state. These two tasks will be subject of a detailed analysis.

This research was conducted in the framework of the SPARC collaboration, experiment E138 of FAIR Phase-0 supported by GSI. We acknowledge support by the ERC under the European Union's Horizon 2020 research, by the innovation program (grants 824109 'EMP') as well as by ErUM FSP T05 - "Aufbau von APPA bei FAIR" (BMBF grants 05P19SJFAA and 05P19VHFA1).

References

- [1] P. Pfäfflein *et al.*, Phys. Scr. **97**, 114005 (2022).
- [2] D. Hengstler *et al.*, Phys. Scr. **T166**, 014054 (2015).
- [3] P. Pfäfflein *et al.*, Atoms 2023, **11**, 5 (2022).
- [4] T. Gassner *et al.*, New J. Phys. **20**, 073033 (2018).
- [5] A. Gumberidze *et al.*, J. Phys.: Conf. Ser. **58**, 87 (2007).
- [6] F. M. Kröger *et al.*, Atoms 2023, **11**, 22 (2023).

*felix.kroeger@uni-jena.de

New Regimes of Nuclear Resonance Excitation: First Experiments at the European XFEL

Ralf Röhlsberger^{1,2,3,*}

¹DESY, Hamburg, Germany; ²Helmholtz Institute Jena, Jena, Germany; ³Friedrich-Schiller-Universität Jena, Germany; *for the Multiphoton Collective Lamb Shift collaboration and the ⁴⁵Sc collaboration

The nuclear resonances of Mössbauer isotopes provide extremely narrow energy references for high-resolution spectroscopy. This qualifies them for applications in condensed matter physics as well as for studies in fundamental physics and extreme metrology. Since the pioneering experiment by E. Gerdau *et al.* [1] at the storage ring DORIS (DESY, Hamburg), the technique of nuclear resonance scattering has found widespread applications at hard X-ray synchrotron radiation sources worldwide. Its implementation and use at hard X-ray laser sources started with one experiment performed at SACLA in Japan reported so far [2].

In 2022 we could perform the first experiments on nuclear resonance scattering at the European XFEL. One study was conducted at the 14.4 keV resonance of ⁵⁷Fe aiming at applications in x-ray quantum optics in a collaboration with researchers from Friedrich-Schiller-Universität Jena, the Max Planck Institute of Nuclear Physics in Heidelberg, the University of Freiburg and DESY. The other experiment, initiated by researchers from Argonne National Laboratory and Texas A&M University in College Station, USA, succeeded to achieve the first photonic excitation of the ultranarrow 12.4 keV resonance of ⁴⁵Sc for future applications in extreme metrology.

Employing the 14.4 keV nuclear resonance of ⁵⁷Fe we aimed at the realization of multiphoton excitation in forward scattering from an ensemble of Mössbauer nuclei. Due to the radiative coupling between the nuclei in the ensemble, an enhanced decay rate (superradiance, SR) and collective energy shifts (collective Lamb shift, CLS) appear as characteristic signatures in the scattered light. So far, SR and CLS have been extensively studied in the single-photon excitation regime at synchrotrons. Here we were aiming to reveal the spectral properties of the nuclear exciton under multiphoton excitation conditions, especially with the goal to determine the CLS as function of the number of photons that resonantly excite the nuclear ensemble. So far, the spectral properties under multiphoton excitation conditions have neither been approached theoretically nor experimentally. Our experiment in 2022 was mainly devoted to reliably detect the nuclear forward scattering signal in the presence of the extremely intense radiation pulses of the European XFEL.

The 12.4 keV resonance of ⁴⁵Sc is one of the narrowest nuclear resonances known with a half width of 1.4 femto-eV. In several aspects this isotope is superior to the 8.3 eV

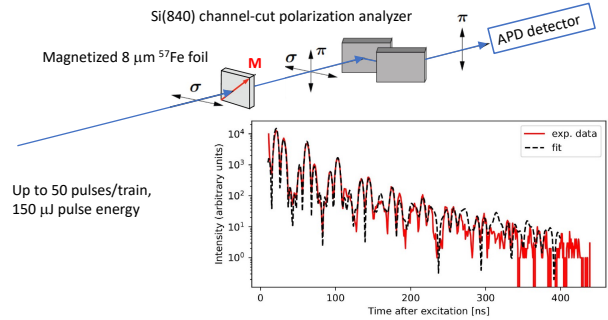


Figure 1: Experimental setup and first nuclear resonance scattering data recorded at the European XFEL.

^{229m}Th isomer for extreme metrology applications. The scientific potential of the ⁴⁵Sc resonance together with the possibility to resonantly excite it by photons from modern accelerator-based hard x-ray sources was identified more than 30 years ago [3]. However, it escaped detection until now, mostly due to the lack of hard x-ray sources with sufficient spectral flux. In this experiment the nuclear resonance of ⁴⁵Sc was successfully observed by irradiation of a Sc metal foil with 12.4-keV x-ray pulses of sub-millisecond duration and detection of the 4 keV delayed K-fluorescence that followed internal nuclear conversion. The resonance energy, which was known before the experiment to an uncertainty of ± 50 eV only was determined with sub-eV accuracy. Our results set the stage for further studies of this isotope with promising applications in fundamental physics and extreme metrology.

Both experiments greatly benefitted from the high pulse repetition rate in conjunction with hard x-ray self-seeding (HXRSS) at the respective nuclear resonance energies, providing the spectral flux for efficient nuclear resonance excitation. A unique pulse pattern will be extremely beneficial for future studies at the ⁴⁵Sc resonance, in particular for the analysis of hyperfine interactions via nuclear forward scattering.

References

- [1] E. Gerdau *et al.*, Phys. Rev. Lett. **54**, 835 (1985)
- [2] A. I. Chumakov *et al.*, Nature Physics **14**, 261 (2018)
- [3] Yu. V. Shvyd'ko and G. V. Smirnov, Nucl. Instrum. Methods Phys. Res. B **51**, 452 (1990)

Mössbauer Spectroscopic Imaging of Magnetic Domains

M. Kobayashi¹, K. Hayakawa¹, Y. Ishida¹, Y. Yoshida^{*1,2}, and R. Röhlberger²

¹Shizuoka Institute of Science and technology, Japan; ²HI Jena, Fröbelstieg 3, 07743 Jena, Germany

A new laboratory for Mössbauer Spectroscopic Imaging has been opened at the Helmholtz Institute Jena. This technique allows to study inhomogeneous materials, containing complex microstructures such as point defects, dislocations, ion tracks, and crystal grains, and furthermore, magnetic domains, all of which are often accompanied by strain fields. Such complex systems appear to be difficult to investigate by conventional spectroscopic imaging techniques, which are nowadays available at a synchrotron facility with an intensity in beams of eV bandwidth that could damage sensitive samples. Our technique can access such complex system without disturbing their atomic structure, because it is based on the Mössbauer effect with its ultranarrow energy bandwidth. The spatial resolution could reach down to the sub-micrometre scale separately for different Mössbauer components.

Recently, we have developed a Mössbauer Spectroscopic Microscope [1], directly based on the Mössbauer effect, i.e., the recoil-free absorption and emission of γ -radiation. We applied this technique for studies of Fe impurities in Si-solar cells [1] and magnetic domains in a ^{57}Fe foil [2]. In the year 2022, we have transferred the set-up from Shizuoka, Japan, to Jena, and have brought it successfully into operation. In this report, we show first this microscopic technique, and as an example, present the magnetic domain structure of a ferromagnetic ^{57}Fe foil without and with an external magnetic field [2].

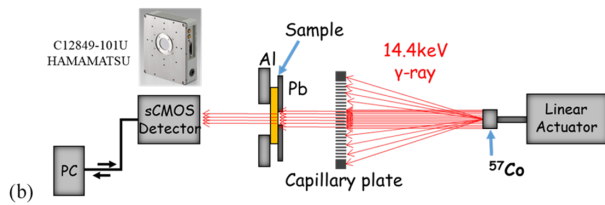


Figure 1: Mössbauer spectroscopic imaging setup [1, 2].

The setup is based on an X-ray CMOS camera (HAMAMATSU). To get a parallel γ -ray beam from a 3.7 GBq - ^{57}Co source, we use a lead-glass capillary plate with a thickness of 1 mm acting as a collimator where each capillary hole has a size of 6 μm . The scintillator at the camera's entrance converts the transmitted 14.4 keV γ -rays and the 6.4 keV nuclear fluorescence X-rays from a 2 μm -thick - ^{57}Fe foil into visible light. The CMOS camera consists of

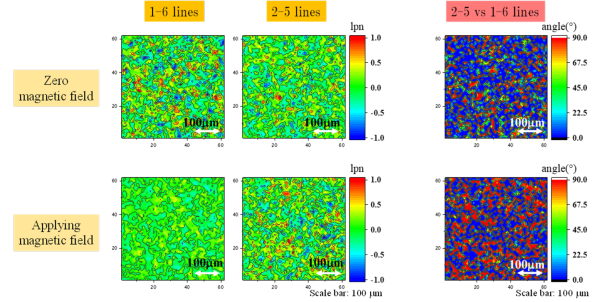


Figure 2: Contour images measured under resonance conditions for (A) the hyperfine lines 1 and 6 and (B) the lines 2 and 5. The upper and lower three pictures were obtained without/with external magnetic field of 0.35 T parallel to surface, respectively. (C) displays the angular orientations between γ -rays and the magnetization direction, which were obtained by eq. 1 [2].

4×10^6 pixels and achieves a spatial resolution of 5 μm .

In Fig. 2, we show magnetic domains in the Fe foil revealed by the Mössbauer spectroscopic microscope. The spectrum of ferromagnetic Fe is a sextet due to the magnetic dipole interaction with an area intensity ratio, I_{2-5}/I_{1-6} , between the lines 1 and 6 and the lines 2 and 5 that is given by:

$$\frac{I_{2-5}}{I_{1-6}} = \frac{4 \sin^2 \theta}{3(1 + \cos^2 \theta)} \quad (1)$$

yielding the angle θ between the directions of magnetisation and incoming γ -rays. $\theta = 90^\circ$ means the magnetisation is oriented parallel to the surface, while $\theta = 0^\circ$ is a perpendicular orientation. As shown in Fig. 2, which could provide a “photograph” every hour in the light of the respective Mössbauer spectral components. In the latest experiment performed in Jena, the spatial resolution has been further improved which will be reported soon.

References

- [1] Modern Mössbauer Spectroscopy: New Challenges Based on Cutting-Edge Techniques, in Topics in Applied Physics, Eds. Y. Yoshida and G. Langouche, Vol **137**, Springer, Singapore (2021).
- [2] M. Kobayashi, K. Hayakawa, Y. Yoshida, R. Röhlberger, Hyperfine Interactions **243**, **9** (2022). <https://doi.org/10.1007/s10751-022-01796-0>.

*y.yoshida@hi-jena.gsi.de

Ion storage with the new HILITE Penning ion trap

S. Ringleb¹, M. Kiffer¹, G.G. Paulus^{1,2}, W. Quint^{3,4}, Th. Stöhlker^{1,2,3}, and M. Vogel³

¹Intitut für Optik und Quantenelektronik, 07743 Jena, Germany; ²Helmholtzinstitut Jena, Fröbelstieg 3, 07743 Jena, Germany; ³GSI Helmholtzzentrum für Schwerionenforschung, 64291 Darmstadt, Germany; ⁴Physikalisches Institut, Ruprecht Karls-Universität Heidelberg, 69120 Heidelberg, Germany

The HILITE Penning trap setup is designed to prepare well-defined ion targets for light-matter interaction experiments at high intensities and / or high photon energies. We have recently put into operation a novel trap that is optimised for dynamic capture and storage of highly energetic ions.

In March 2022 we have moved the HILITE setup [1, 2] to Jena and have set it up successfully. In the course of this effort, the overall setup has been revised as described in last year's annual report, and recently we have put into operation a novel 7-pole cylindrical open-endcap trap that is optimised for dynamic capture and storage of highly energetic ions injected from an attached EBIT ion source.

We have non-destructively detected the ions inside the Penning trap with a normal-conducting axial resonator connected to one electrode of the trap. The centre frequency matches the Ar^{7+} ions injected from the ion source to within 2%, even at the given high ion energy. From the width of the peak (see figure 1) we deduce an energy spread of much less than 1 eV/q of the ions which is an ideal situation for the envisaged resistive ion cooling.

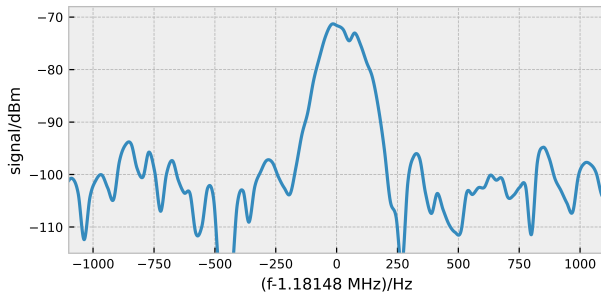


Figure 1: Ion signal of a stored Ar^{7+} ion bunch. The ions were detected non-destructively using an axial resonant circuit. The frequency is the axial frequency of the ions and the frequency distribution is caused by the ions' energy distribution.

In addition, we have developed and operated a four-fold segmented charge-counter device which is based on the experiences we have acquired before with a single-electrode device [3]. It consists of four electrodes with individual electronic processing of the signals induced by passing ion bunches. The detector is divided into two pairs of electrodes, one pair is used to detect the ion position in the horizontal direction, the other one determines the position in the vertical direction. The setup is shown in figure 2a. From the acquired signals (see figure 2b) we can reconstruct the ion bunch position with respect to the detector

axis. As both electrode pairs are also separated in the axial direction, from the temporal distance of the ion signals we can calculate the velocity and hence the kinetic energy of the ions directly.

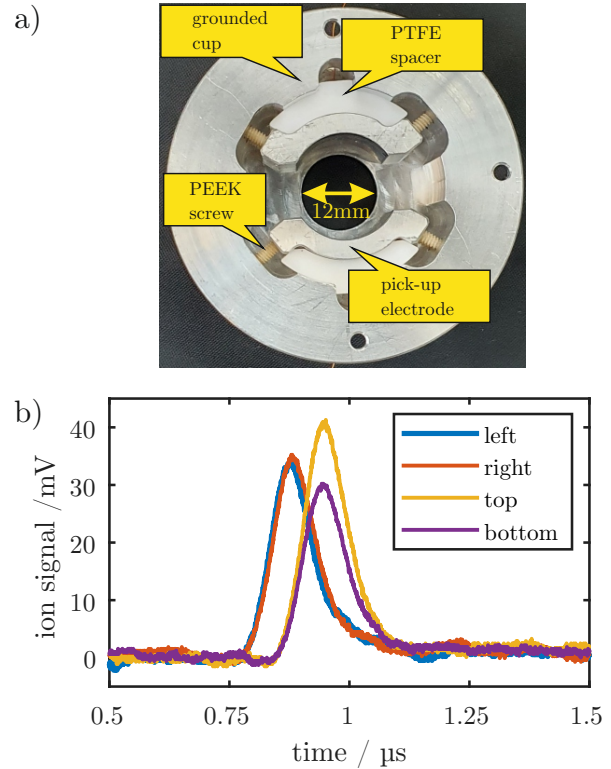


Figure 2: a) Mechanical setup of one electrode pair. The opposite electrodes are hold in place by a polytetrafluorethylene (PTFE) spacers and is attached by four PEEK screws each. b) Time signals of an ion bunch acquired simultaneously by all four electrodes.

References

- [1] S. Ringleb *et al.*, J. Phys. Conf. Ser. **635**, 092124 (2015).
- [2] N. Stallkamp *et al.*, X-Ray Spectrometry **49**, 188 (2019).
- [3] M.Kiffer *et al.*, Rev. Sci. Inst. **90**, 113301 (2019).

Preparation of eutectic alloys for liquid metal ion sources and laser-induced dissociation dynamics of the gold molecular ion

F. Machalett^{*1,2,3}, B. Ying^{1,2}, B. Wang², M. Kübel^{1,2}, A. Sommerfeld², S. Lippmann⁴, A. M. Sayler⁵, Th. Stöhlker^{1,2,3}, and G. G. Paulus^{1,2}

¹Helmholtz Institute Jena, Fröbelstieg 3, 07743 Jena, Germany; ²Institute of Optics and Quantum Electronics, Friedrich Schiller University Jena, 07743 Jena, Germany; ³GSI Helmholtz-Zentrum für Schwerionenforschung, 64291 Darmstadt, Germany; ⁴Otto Schott Institute of Materials Research, Friedrich Schiller University Jena, 07743 Jena, Germany; ⁵Benedictine College, Atchison, KS, USA

We report significant improvements in the preparation of alloys and ion emitters for high-brightness liquid metal ion sources (LMIS). LMIS were used for novel studies of the interaction of heavy metal and metalloid ions with intense femtosecond laser pulses, which allow the investigation of relativistic effects in multi-electron systems. First time-resolved measurements of the dissociation dynamics of the gold dimer ion were conducted using a pump-probe scheme.

In this work, we have produced ion emitters for LMIS with improved accuracy and reproducibility. The preparation of suitable source feed materials is achieved using vacuum induction furnace to melt the components of alloys (Fig. 1). The substances were placed in a cold-walled crucible. Due to magnetic levitation, the molten metal is contactless at the crucible during the alloying process, which results in particularly pure alloys. Electromagnetic stirring enables effective mixing of the alloy constituents.

We adapted the high-brightness LMIS, originally applied in focused ion beam systems [1], to an ion system for 3D coincidence momentum spectroscopy (Fig. 2). Using a Wien filter in the beamline, different ion species could be selected: Si^+ , Si^{2+} , Au^+ , Au^{2+} , Au_2^+ , Au_3^+ and Au_3^{2+} .

The experiment uses 40-fs laser pulses centered at 1030 nm and their second harmonic at 515 nm, with a variable delay up to several picoseconds. The pump pulse first dissociates Au_2^+ , resulting in Au^+ and Au . After the system evolves freely for some time Δt , the probe pulse arrives and ionizes the dissociated Au to Au^+ . The resulting $\text{Au}^+ + \text{Au}^+$ ion pair coulomb explodes, mapping the internuclear distance onto the KER (Kinetic Energy Release) of the final fragments. By measuring the KER as a function of delay Δt , we obtain an image of the dissociation dynamics (Fig. 3). Due to the relatively slow nuclear motion of Au and Au^+ , we achieve high temporal resolution, even without the use of attosecond laser pulses.

Our results show that LMIS makes accessible a broad range of ion species for experiments in strong-field physics.

The authors acknowledge funding from the Deutsche Forschungsgemeinschaft (Priority program 1840, Quantum Dynamics in Tailored Intense Fields). We thank the IBC at Helmholtz-Zentrum Dresden-Rossendorf e.V. for support during the earlier experiments.

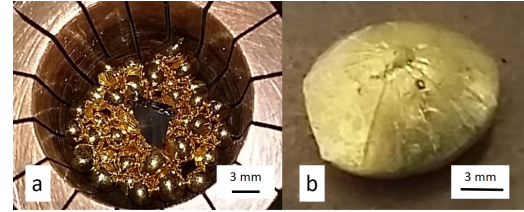


Figure 1: (a) Preparation of low-melting Au-Si eutectic alloys in a vacuum induction furnace and (b) sample of Au-Si source feed material for wetting of the LMIS emitter.

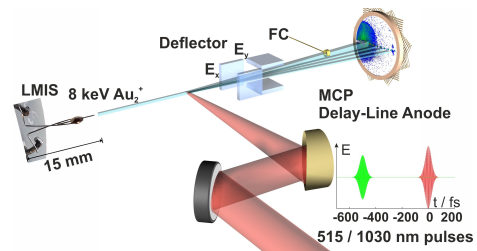


Figure 2: Femtosecond laser pulses are focused onto a 8 keV ion beam of Au_2^+ emitted from the LMIS, blocked by a Faraday Cup (FC). The dissociation fragments are detected by a time- and position-sensitive detector. In the inset the time-delayed two-color electric field is shown [2].

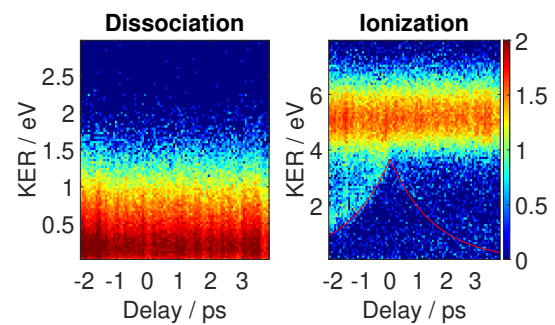


Figure 3: Temporal evolution of the KER distributions resulting from dissociation and ionization of Au_2^+ . The red curve indicates the margin of the transition from dissociation to ionization.

References

- [1] F. Machalett, P. Seidel, Focused Ion Beams and Some Selected Applications, EAP, Wiley (2019)
- [2] B. Ying, *et al.*, J. Phys. B: At. Mol. Opt. Phys. **54** (2021)

*f.machalett@gsi.de

Real-Time Observation of Temperature-Induced Nanofaceting on Sapphire Surfaces

Denise J. Erb¹, Jan Perlich², Stephan V. Roth², Ralf Röhlsberger^{2,3,4}, and Kai Schlage²

¹Helmholtz-Zentrum Dresden-Rossendorf HZDR, Dresden, Germany; ²DESY, Hamburg, Germany; ³Helmholtz Institute Jena, Jena, Germany; ⁴Friedrich-Schiller-Universität Jena, Germany

Upon high-temperature annealing, the crystalline surface of sapphire (α -Al₂O₃) transforms from a planar morphology to one with a nanoscale ripple pattern. This spontaneous crystal reconstruction of sapphire surfaces (M-plane) is employed for nanopatterning and nanofabrication in various fields of research including, among others, magnetism, superconductivity, and optoelectronics. However, the high sample temperature required to induce this surface reconstruction made in situ studies of the process seem unfeasible. The kinetics of ripple pattern formation therefore remained uncertain, and thus production of templates for nanofabrication could not advance beyond a trial-and-error stage. We have developed an approach combining in situ real-time grazing incidence small-angle X-ray scattering experiments (GISAXS) with model-based analysis and with ex situ atomic force microscopy to observe this morphological transition in great detail. Our approach provides time-resolved information about all relevant morphological parameters required to trace the surface topography on the nanometer scale during reconstruction.

Nanopatterned surfaces for application in bottom-up nanofabrication can be obtained from various self-assembly mechanisms, induced for instance by directed material deposition, ion beam irradiation, exposure to chemical reactants, or thermal annealing. A well-known thermally induced selfassembly mechanism is the spontaneous crystal reconstruction of the M-plane {10 $\bar{1}$ 0} surface of α -Al₂O₃ which has a comparatively high surface free energy density and is therefore metastable. While increasing the surface area, a reconstruction into facets of lower surface free energy density reduces the total surface free energy and is thus predicted to occur spontaneously upon high-temperature annealing when diffusive mass transport on the surface is enabled. The initially planar M-plane {10 $\bar{1}$ 0} surface of α -Al₂O₃ then reconstructs into a rippled morphology with facets of R-plane {1 $\bar{1}$ 02} and S-plane {10 $\bar{1}$ 1} orientation, where the facet ridges run parallel to the [1 $\bar{2}$ 10] direction. The facet ridges have a larger contribution to the surface free energy than a planar surface, so their number is decreased by coarsening of the ripple morphology to further minimize the total surface free energy.

In situ studies, necessary to understand the actual kinetics of structure formation especially during the early phase of annealing, seemed to be hardly feasible so far:

As the process takes place at high temperatures above 1000°C and the resulting surface features are nanoscopic in size, a contact-less method with subnanometer resolution is needed. Because the structure formation sets in spontaneously and inhomogeneously on the surface, its in situ observation also requires a method that averages over a significant portion of the surface area with adequate speed.

To approach these challenges in studying the α -Al₂O₃ surface faceting process, we combine an in situ real-time grazing incidence small-angle X-ray scattering observation with modeling and ex situ atomic force microscopy. The reciprocal space information gained from the GISAXS experiment can then be compared with a GISAXS model and with structure formation theory and be related to real space information obtained from *ex-situ* atomic force microscopy. This provides a comprehensive description of the nanopatterning process in M-plane α -Al₂O₃, which can advance the predictability of annealing outcome and thus help to efficiently customize nanopatterned α -Al₂O₃ - templates for improved nanofabrication routines.

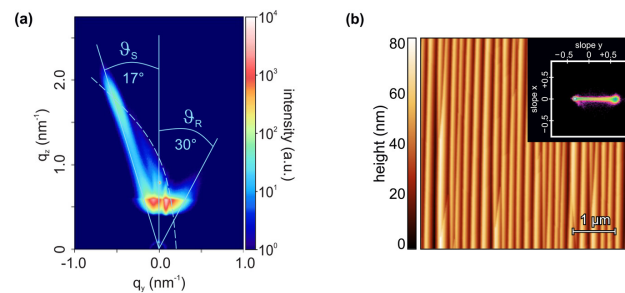


Figure 1: (a) GISAXS intensity map of a α -Al₂O₃ sample annealed at 1420 °C for 1380 min. (b) AFM topography image of a reconstructed α -Al₂O₃ surface in equilibrium after 2880 min of annealing at 1600°C. The inset shows the two-dimensional slope histogram of the surface.

This work was financed by Deutsches Elektronen-Synchrotron and Helmholtz-Zentrum Dresden- Rossendorf as an in-house research project without third-party funding contributions.

References

- [1] D. Erb *et al.*, ACS Appl. Mater. Interfaces **14**, 31373 (2022)

Progress Report of the Negative Ions Laser Photodetachment Project

Oliver Forstner^{*1,2}, Vadim Gadelshin³, Kurt Stiebing⁴, and Klaus Wendt³

¹Helmholtz Institute Jena; ²Institut für Optik und Quantenelektronik, Friedrich–Schiller–Universität Jena; ³Institut für Physik, Johannes Gutenberg–Universität Mainz; ⁴Institut für Kernphysik, Goethe–Universität Frankfurt

The negative ions laser photodetachment project aims to use the element selectivity of photodetachment to suppress isobars in high sensitive mass spectrometry. A dedicated ion beam cooler will be used to efficiently deplete the unwanted isobars. The required electron affinities of negative atomic and molecular ions will be gathered by the help of electrostatic storage rings like FLSR at the Goethe–University Frankfurt.

The funding period of the subproject 05K19SJ1 of the BMBF funded joint project 05K2019 – LISEL@DREAMS has been extended until end of 2022. A new funding 05K2022 – ELISE@IBC with a three year funding period starting from 1st of October 2022. The LISEL@DREAMS setup at Jena progressed further. The ion beam cooler has been nearly finished and awaits commissioning. A dedicated single cathode sputter ion source for producing atomic and molecular negative ion beams has been acquired and the corresponding beam line has been installed. A 90° double focusing sector magnet has been delivered by Danfysik and was installed in the second half of 2022. The status of the LISEL setup at the University of Jena is depicted in Fig. 1.

At the setup at low–energy electrostatic storage ring FLSR at the Goethe–University Frankfurt first successful photodetachment experiments has been performed. A beam of O^- has been successfully stored and the region around the threshold could be scanned by tuning the laser



Figure 1: The LISEL setup at the University of Jena. On the left the ion source cage with the extraction lens. In the middle the double focusing sector field magnet. On the right the LISEL cooler inside the high voltage cage.

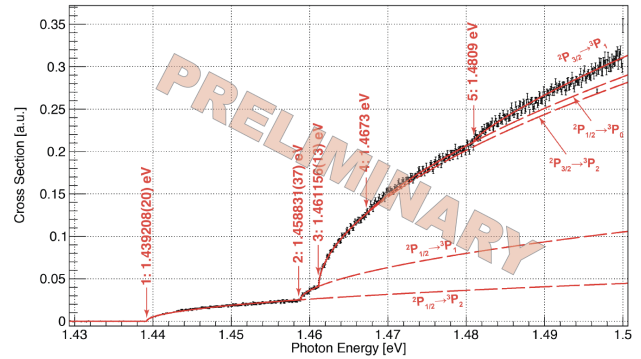


Figure 2: Photodetachment spectrum of O^- stored at FLSR at 20 keV. For each threshold the fit to the Wigner law is shown and the corresponding levels of the negative ion and the neutral atom are given.

wavelength. The fine structure splittings of the O^- and the neutral oxygen could be determined with high statistics. A typical photodetachment spectrum gathered at FLSR is shown in Fig. 2. The electron affinity of O^- (detachment of the fine structure ground state of the anion to the fine structure ground state of the neutral) is the third threshold in the spectrum. It is obscured by two lower energetic thresholds resulting from the excited $2P_{1/2}$ level in the anion.

In the project ELISE@IBC the photodetachment scheme will be extended to the rare earth elements. To achieve this, a tuneable laser system in the infrared region will be developed together with the industry partner Hübner Photonics. A research group at the TU Dresden has been included as a new project partner. Their contribution to the project will be to identify molecular systems suitable for mass spectrometry of rare earth elements. The near goal is to establish high sensitive mass spectrometry of holmium isotopes.

This project is supported by funding from the German Ministry of Science BMBF, joint project 05K2019 – LISEL@DREAMS and joint project 05K2022 – ELISE@IBC.

References

- [1] O. Forstner *et al.*, The ILIAS project for selective isobar suppression by laser photodetachment, Nucl. Instr. and Meth. **B 361**, 217–221 (2015).
- [2] O. Forstner *et al.*, Opportunities for negative ions studies at the Frankfurt Low–energy Storage Ring (FLSR), Hyp. Int. **241**, 53 (2020).

^{*}o.forstner@hi-jena.gsi.de

THEORY

Optimally chirped laser pulses for increased narrowband photon yield from Inverse Compton Scattering sources

M. A. Valialshchikov^{*1} and D. Seipt¹

¹HI Jena, Fröbelstieg 3, 07743 Jena, Germany

Inverse Compton scattering is a promising source of X-ray and gamma radiation. For temporally pulsed lasers the resulting spectra are broadband which severely limits practical applications. Using chirped pulses is one of the ways to compensate that broadening. We show for laser pulses chirped in the spectral domain that there is an optimal chirp parameter at which the photon spectrum has the highest peak. We use catastrophe theory to find this optimal value analytically.

The scattering of intense laser pulses on high-energy electron beams is a promising source of X-ray and gamma radiation. Such sources have a range of applications, including medicine, ultrafast radiography and nuclear physics. Small intensities of an incident laser pulse lead to meager photon yields. Increasing laser pulse intensity helps to boost photon yield but also leads to the appearance of nonlinear effects. In addition, for temporally pulsed lasers this also leads to the so-called spectral ponderomotive broadening. There are different approaches aimed at compensating or avoiding this broadening that are usually connected with the modification of the incident pulse or scattering geometry. Among these approaches is laser pulse chirping, i.e. when the laser frequency changes with its phase.

It was previously shown that using laser pulses linearly chirped in the time domain leads to more narrowband spectra [1]. In our work we moved towards a more realistic experimental scenario and considered laser pulses linearly chirped in the spectral domain [2]. The laser spectrum is here modelled as follows,

$$\tilde{A}(\omega) = \sqrt{2\pi}a_0\tau \exp\left(-\frac{\tau^2}{2}(\omega - \omega_0)^2(1 - i\beta)\right), \quad (1)$$

where a_0 is the laser amplitude, ω_0 is the central laser frequency, and τ is the Fourier-limited pulse duration (i.e. with vanishing spectral phase). The second order spectral phase parameter β controls the amount of linear chirp. In addition to temporally chirping the pulse, increasing β also stretches the effective duration and reduces the peak amplitude in the time domain, $a_{\text{eff}}(\beta) < a_0$, $\tau_{\text{eff}}(\beta) > \tau$, but with $a_{\text{eff}}^2\tau_{\text{eff}} = \text{const.}$ [2]. These are the new effects compared to [1].

After the calculation of electron's trajectories $\mathbf{r}(t)$, $\mathbf{u}(t)$, and with \mathbf{n} as the direction of observation, the differential photon number is given by

$$\frac{d^2N}{d\omega d\Omega} = \frac{\omega e^2}{4\pi^2} \left| \int_{-\infty}^{\infty} \frac{dt}{\gamma} \mathbf{n} \times [\mathbf{n} \times \mathbf{u}] e^{i\omega(t - \mathbf{n} \cdot \mathbf{r})} \right|^2. \quad (2)$$

^{*}maksim.valialshchikov@uni-jena.de

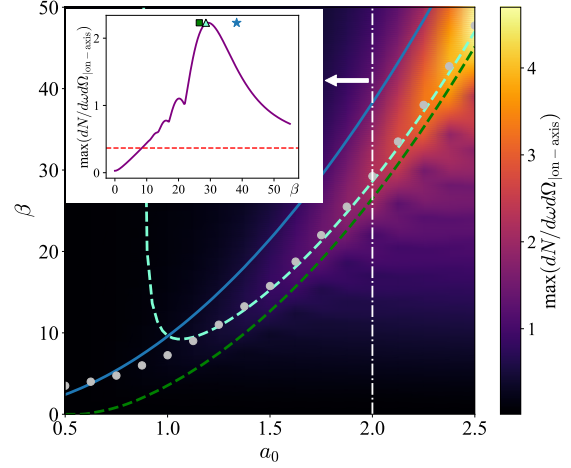


Figure 1: Peak of the differential photon number (colormap) as a function of laser amplitude a_0 and chirp parameter β for $\tau = 4\pi$. Grey dots show the optimal β at which the peak has the highest value for a fixed a_0 . Curves are different analytical predictions for optimal β based on catastrophe theory. (Inset) Slice of the colormap at $a_0 = 2$, triangle, square and star symbols stand for different analytical predictions of optimal β , red dashed line shows the limit $\beta \gg 1$ for given a_0, τ . Figure adapted from Ref. [2].

Figure 1 shows the optimization landscape of our problem. In particular, it can be seen that for each fixed spectral amplitude a_0 there exists an optimal value of linear chirp β at which the backscattered spectra has the highest peak. Grey dots correspond to numerically found optimal value; the curves correspond to different analytical predictions based on catastrophe theory. The basis of these predictions is the fact that the value of the integral in (2) is maximised if its phase becomes stationary to higher orders [1, 2]. In particular, the dashed cyan curve, which is derived from the location of the maximum of the universal Pearcey diffraction pattern near a cusp catastrophe (including prefactor corrections [2]), is in a very good agreement with simulations for $a_0 > 1$.

The code to reproduce the results from the article can be found in [3].

References

- [1] V. Yu. Kharin, D. Seipt, and S. G. Rykovanov, Phys. Rev. Lett. **120.4**, 044802 (2018).
- [2] M. A. Valialshchikov, D. Seipt, V. Yu. Kharin and S. G. Rykovanov, Phys. Rev. A **106.3**, L031501 (2022).
- [3] <https://github.com/maxbalrog/optimal-chirp>

Calculations of multipole transitions in Sn II for kilonova analysis

A.I. Bondarev^{*1,2}, J. H. Gillanders³, C. Cheung⁴, M. S. Safronova^{4,5}, and S. Fritzsche^{1,2,6}

¹Helmholtz Institute Jena, Germany; ²GSI Helmholtzzentrum für Schwerionenforschung, Darmstadt, Germany;

³University of Rome “Tor Vergata”, Rome, Italy; ⁴University of Delaware, Newark, USA; ⁵Joint Quantum In-

stitute NIST and UMD, College Park, USA; ⁶Friedrich Schiller University, Jena, Germany

We use the method that combines linearized coupled-cluster and configuration interaction approaches for calculating energy levels and multipole transition probabilities in singly-ionized tin ions. We show that our calculated energies agree very well with the experimental data. We present probabilities of magnetic dipole and electric quadrupole transitions and use them for the analysis of the AT2017gfo kilonova emission spectra. This study demonstrates the importance and utility of accurate atomic data for forbidden transitions in the examination of future kilonova events.

Recent observations of the kilonova (KN) AT2017gfo [1, 2], an astronomical transient associated with the gravitational wave signal from the binary neutron star merger GW170817 [3], provided much needed data for studying the origin of heavy elements in the universe [4]. The analysis of the AT2017gfo light curves strongly supports that the source of electromagnetic emission was radioactive decay of elements synthesized by the rapid neutron capture process (*r*-process) in plasma ejected from the merger site during or after the collision [5]. However, in order to gain more insight into the composition of the ejecta, a spectroscopic line identification of particular elements is essential.

In the present contribution, we report calculations of low-lying energy levels and multipole (E1, M1, E2) transition probabilities in Sn II using a method that combines linearized coupled-cluster and configuration interaction approaches [6]. We use the atomic data to analyze the AT2017gfo spectra and show that forbidden transitions in Sn II could lead to detectable features in the kilonova emission spectra.

In our atomic computations, we use the method that combines configuration interaction with a linearized coupled-cluster approach [7]. In this method, the coupled-cluster approach is used to construct an effective Hamiltonian H_{eff} that includes core-core and core-valence correlations. The configuration interaction calculation is then done for valence electrons using the effective Hamiltonian rather than the usual bare Hamiltonian to incorporate core correlations. For our astrophysical analysis, we follow the same method outlined by Gillanders *et al.* [8] for their study of [Pt] and [Au] emission.

In Figure 1, we present comparisons between the E1, M1 and E2 synthetic emission spectra for Sn II and the late-time spectra of AT2017gfo (taken from Refs. [1, 2]). We see that the M1 23512 Å feature is comparably as strong as some of the emission features present in the observed data.

The [Sn II] transition at $\lambda = 23512 \text{ Å}$ is expected to

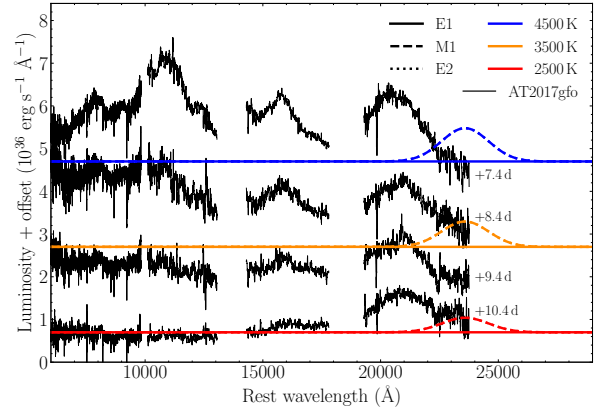


Figure 1: Sn II E1, M1 and E2 synthetic emission spectra compared with the observed late-time (+7.4 – 10.4 day) emission spectra of AT2017gfo. Both the observed and synthetic spectra have been offset for clarity. The synthetic spectra presented span a range of temperatures ($T \in [2500, 3500, 4500] \text{ K}$), and are plotted as red, orange and blue curves, respectively. The Sn II E1, M1 and E2 emission spectra are plotted as solid, dashed and dotted lines, respectively.

be the only detectable Sn II line across a range of plausible ejecta temperatures. However, a modest mass of Sn II ($M_{\text{Sn II}} = 10^{-3} M_{\odot}$) is sufficient to produce a line strength on par with the emission features observed in the late-time spectra of AT2017gfo. Although this feature is too red to be responsible for the observed emission feature at $\sim 2.1 \mu\text{m}$ in the AT2017gfo spectra, it can be used as a probe to infer the presence of Sn II in future KN events. Such predictions for the expected locations of prominent emission features are important for future analyses of new kilonova events, to better constrain their composition profiles.

References

- [1] E. Pian *et al.*, Nature **551**, 67 (2017).
- [2] S.J. Smartt *et al.*, Nature **551**, 75 (2017).
- [3] B.P. Abbott *et al.*, Phys. Rev. Lett. **119**, 161101 (2017).
- [4] D. M. Siegel, Nat. Rev. Phys. **4**, 306 (2022).
- [5] S. Rosswog *et al.*, Astron. Astrophys. **615**, A132 (2018).
- [6] A. I. Bondarev *et al.*, Eur. Phys. J. D *accepted* (2023).
- [7] M. S. Safronova *et al.*, Phys. Rev. A **80**, 012516 (2009).
- [8] J. H. Gillanders *et al.*, Mon. Not. R. Astron. Soc. **506**, 3560 (2021).

*a.bondarev@hi-jena.gsi.de

Radiative recombination of highly-charged ions with polarized electrons

A.V. Maierova^{*1,2}, S. Fritzsche^{1,2,3}, A. Surzhykov^{4,5,6}, and Th. Stöhlker^{1,2,3}

¹Helmholtz Institute Jena, Germany; ²GSI Helmholtzzentrum für Schwerionenforschung GmbH, Darmstadt, Germany;

³Friedrich-Schiller-Universität Jena, Germany; ⁴PTB, Braunschweig, Germany; ⁵Technische Universität Braunschweig, Germany; ⁶Laboratory for Emerging Nanometrology Braunschweig, Germany

We present a theoretical study of the radiative recombination (RR) of arbitrary (longitudinally and transversely) polarized electrons into a bound state of initially bare heavy ions. In order to investigate how the spin polarization of incident electrons may affect the linear polarization of emitted photons, we apply the density matrix approach and solutions of relativistic Dirac equation. We obtain simple analytical expressions for the dependencies of the differential cross section and the polarization Stokes parameters of RR photons on the components of the incident electrons polarization vector, which allow to analyze the polarization transfer. Based on these expressions, we show that the linear polarization of RR photons is very sensitive to the spin state of an electron target.

Spin-polarized heavy ion beams are highly relevant for future investigations of the relativistic, QED and parity-violation phenomena in a high-Z domain and for the search of new physics beyond the Standard Model [1, 2]. The present challenge of storage-ring physics is the production and preservation of such polarized beams. The radiative recombination of free (or quasi-free) electrons is a suitable tool for both the production of spin-polarized ion beams [3] and control the polarization state of ions [4].

In this work, the general theory for the spin-polarization transfer between incident electrons and the emitted x-rays, which accounts for arbitrary (longitudinal and/or transversal) polarization of electron beam, was developed. Within the framework of the density matrix formalism, we investigate the dependence of Stokes parameters on three projections of electron polarization vector: $P_1(P_x, P_y, P_z)$, $P_2(P_x, P_y, P_z)$. Simple analytical expressions, which allow to understand how the degree and direction of linear polarization of RR photons depend on the spin state of captured electron, are obtained. The RR differential cross section takes a form:

$$\frac{d\sigma}{d\Omega} = \sqrt{2} \Re_{00}(1, 1) + 2P_y \text{Im} \Re_{11}(1, 1),$$

whereas the Stokes parameters of emitted photons are given by:

$$P_1 = \frac{\sqrt{2} \Re_{00}(1, -1) - iP_y (\Re_{1-1}(1, -1) + \Re_{11}(1, -1))}{\sqrt{2} \Re_{00}(1, 1) + 2P_y \text{Im} \Re_{11}(1, 1)}$$

$$P_2 = \frac{i \sqrt{2} P_z \Re_{10}(1, -1) + P_x (\Re_{1-1}(1, -1) - \Re_{11}(1, -1))}{\sqrt{2} \Re_{00}(1, 1) + 2P_y \text{Im} \Re_{11}(1, 1)}.$$

*A.Maierova@gsi.de

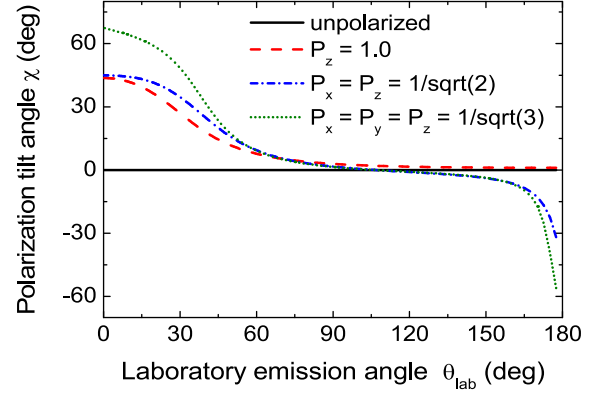


Figure 1: Tilt polarization angle χ as function of photon emission angle θ_{lab} in the laboratory frame and for different polarization states of incident electrons. Calculations have been performed for the radiative capture of polarized electrons into the ground state of (initially) bare uranium projectile U^{92+} with energy $T_p = 400$ MeV/u.

Here tensors $\Re_{kq}(\lambda, \lambda')$ are constructed from the (products of) transition matrix elements. For more details see [5]. The Stokes parameters are very convenient for the theoretical analysis of RR measurements. From the experimental viewpoint, however, it is more practical to visualize the linear polarization of light in terms of the polarization ellipse. The relative length of the principal axis of the ellipse defines the degree of linear polarization of light $P_L = \sqrt{P_1^2 + P_2^2}$, while the orientation of this axis with respect to the reaction plane is described by the tilt angle χ : $\cos 2\chi = P_1/P_L$, $\sin 2\chi = P_2/P_L$.

As seen from Fig. 1, the tilt angle of the linear polarization of RR photons is strongly influenced by the polarization of incident electrons. The developed theory opens up opportunities for the spin diagnostics of ion beams by means of the analysis of the linear polarization of recombination photon.

References

- [1] A. Surzhykov *et al.*, Phys. Rev. A **68**, 022710 (2003).
- [2] D. Budker *et al.*, Annalen der Physik **532**, 2000204 (2020).
- [3] A. Bondarevskaya *et al.*, Phys. Rev. A **90**, 064701 (2014).
- [4] S. Tashenov *et al.*, Phys. Rev. Lett. **97**, 223202 (2006).
- [5] A.V. Maierova *et al.*, Phys. Rev. A **107**, 042814 (2023).

Generalized description of the spatio-temporal biphoton state in spontaneous parametric down-conversion

Baghdasar Baghdasaryan^{*1,3}, Fabian Steinlechner^{3,4}, and Stephan Fritzsche^{1,3,4}

¹Helmholtz Institute Jena, Germany; ²Fraunhofer Institute for Applied Optics and Precision Engineering IOF, Germany; ³Theoretisch-Physikalisches Institut, Friedrich-Schiller-Universität Jena, Germany.; ⁴Abbe Center of Photonics

Spontaneous parametric down-conversion (SPDC) is a commonly used technique in quantum applications that utilize photonic entanglement. The efficiency of photon pair generation is often quantified using a $\text{sinc}(L\Delta k/2)$ function, where L represents the length of the nonlinear medium, and Δk denotes the phase mismatch between the pump and down-converted fields. The *sinc* behavior of the phase mismatch is often approximated by a Gaussian function $\exp(-\alpha x^2)$ in theoretical investigations, in order to derive analytical expressions for the SPDC process. However, different values of the optimization factor α have been proposed in the literature, leading to varied theoretical predictions for the same experimental setup. In this paper, we present a choice of α that maximizes the validity of the Gaussian approximation.

In spontaneous parametric down-conversion (SPDC), a nonlinear quadratic crystal is pumped by a strong laser beam, in order to convert high-energy photons into photon pairs. The photon pair generated in SPDC can be entangled in various degrees of freedom, which has been used in many quantum based applications.

The quantum theory of down-converted pairs is a well-established concept that plays a crucial role in modeling SPDC experiments. The biphoton state in the can be written as

$$|\Psi\rangle = N \iint d\mathbf{q}_s d\mathbf{q}_i V(\mathbf{q}_s + \mathbf{q}_i) \text{sinc}\left(\frac{L|\mathbf{q}_s - \mathbf{q}_i|^2}{4k_p}\right) \times \hat{a}_s^\dagger(\mathbf{q}_s) \hat{a}_i^\dagger(\mathbf{q}_i) |vac\rangle, \quad (1)$$

where N is the normalization factor, $V(\mathbf{q}_p)$ is the spatial distribution of the pump beam, L is the length of the nonlinear crystal, $\mathbf{q}_{s,i}$ are the transverse components of wave vectors of down-converted fields (signal and idler), and $\hat{a}_{s,i}^\dagger(\mathbf{q}_{s,i})$ are the corresponding creation operators.

Expression (1) can be simplified if we approximate the *sinc* function with a Gaussian function $\text{sinc}(x^2) \approx \exp(-x^2)$. Similar to expression (1), the approximated Gaussian state is written as

$$|\Psi_G\rangle = N_G \iint d\mathbf{q}_s d\mathbf{q}_i V(\mathbf{q}_s + \mathbf{q}_i) \exp\left(-\alpha \frac{L|\mathbf{q}_s - \mathbf{q}_i|^2}{4k_p}\right) \times \hat{a}_s^\dagger(\mathbf{q}_s) \hat{a}_i^\dagger(\mathbf{q}_i) |vac\rangle \quad (2)$$

This is called Gaussian approximation, which has been shown to be very useful, since many analytical expressions have been derived within this approximation [1].

However, the calculations within the Gaussian approximation are not exact and show a small deviation from experimentally measured values. The value of α is typically chosen to minimize the error between the exact and approximate expressions for the biphoton state or some other relevant quantity. In the literature, a unique choice of α , which minimizes the error of the approximation, is lacking.

In order to solve this problem, we have looked in the work [2] at the states themselves, instead of comparing just the *sinc* and Gaussian functions. We used the distance measure fidelity, in order to find the particular α that minimizes the distance between the real and approximated state.

The fidelity of the two state can be calculated analytically, giving

$$\langle\Psi|\Psi_G\rangle = 2\sqrt{\frac{\alpha}{\pi}} \arccot \alpha. \quad (3)$$

The first notable aspect of fidelity is that it is independent of the characteristics of the pump laser and the nonlinear crystal. The fidelity depends only on the optimization factor α . The maximum value of fidelity occurs when $\alpha = 0.718$, corresponding to $\langle\Psi|\Psi_G\rangle_{max} = 0.9$.

We can improve the Gaussian approximation by considering instead of just a Gaussian, a more general *cosine*-Gaussian approximation

$$\text{sinc}\left(\frac{L|\mathbf{q}_s - \mathbf{q}_i|^2}{4k_p}\right) \approx \exp\left(-\alpha \frac{L|\mathbf{q}_s - \mathbf{q}_i|^2}{4k_p}\right) \times \cos\left(\beta \frac{L|\mathbf{q}_s - \mathbf{q}_i|^2}{4k_p}\right). \quad (4)$$

The cosine function can be rewritten by using Euler's formula to bring us back to the simple Gaussian-like function with the optimization factor $\alpha - i\beta$. This approximations delivers maximal fidelity $\langle\Psi|\Psi_{CG}\rangle_{max} \approx 0.94$ for the optimization factors $\alpha = 0.39$ and $\beta = 0.49$.

In summery, the Gaussian-like phase-matching functions turn out to deliver very good approximations to *sinc*-like states. We recommend the *cosine*-Gaussian approximation with $\alpha = 0.39$ and $\beta = 0.49$ for most experiments dealing with spatial biphoton state.

References

- [1] C. K. Law and J. H. Eberly, Phys. Rev. Lett. **92**, 127903 (2004).
- [2] B. Baghdasaryan *et al.*, Phys. Rev. A **106**, 063714 (2022).

* baghdasar.baghdasaryan@uni-jena.de

Analytic formula of the critical intensity for high-order harmonic generation

B. Minneker^{*1,2,3} and S. Fritzsche^{1,2,3}

¹Theoretisch-Physikalisches Institut, Friedrich-Schiller-Universität, Jena, Germany; ²Helmholtz Institute Jena, Germany; ³GSI Helmholtzzentrum für Schwerionenforschung GmbH, Darmstadt, Germany

The efficient generation of high-order harmonic radiation is a challenging task since the early days of strong-field physics. An essential requirement to achieve efficient high-order harmonic generation inside a gas medium is the phase matching of the high-order harmonic radiation and the incident laser pulse. The dominant contribution to the wave-vector mismatch Δk is associated with the ionization probability of the medium. A critical intensity is defined, which achieves perfect phase-matching within the peak of a laser pulse while other contributions nullify. An analytical formula for the critical intensity of commonly used noble gases is presented and compared to numerical computations.

To achieve efficient high-order harmonic generation (HHG), the wave-vector mismatch between the harmonic radiation and the incident laser pulse needs to vanish [1]. This wave-vector mismatch consists of four separate terms within the free-focus regime. For specific experimental setups, two of these contributions nullify. The two residual contributions can be combined into a dispersion mismatch, which is associated with the relative number of ionized target atoms. Subsequently, the *critical ionization probability* follows from the respective dispersion mismatch via [2]

$$\eta_c = \left(1 + \frac{2\pi r_e N_{atm} c_0^2}{\omega^2 \Delta \delta}\right)^{-1},$$

with the classical electron radius r_e , the speed of light c , the frequency of the incident laser ω , and the difference between the refractive indices of the laser pulse and the q -th high-order harmonic under standard conditions. For many systems, the ionization probability is computed within the ADK theory that describes strong-field tunnel ionization [3]. The critical intensity within the ADK theory is then derived from the ionization probability as shown in Ref. [2] and reads

$$I_c^{(0)} = \left[\frac{g_0}{F_0} W_0 \left(-\frac{1}{g_0} \left(\frac{D_0}{\tau} \right)^{1/g_0} \right) \right]^{-2} \quad \text{for } g_0 < 0,$$

$$I_c^{(0)} = \left[\frac{g_0}{F_0} W_{-1} \left(-\frac{1}{g_0} \left(\frac{D_0}{\tau} \right)^{1/g_0} \right) \right]^{-2} \quad \text{for } g_0 > 0,$$

$$D_0 = 2\sqrt{2 \ln(2)} \frac{|\ln(1 - \eta_c)|}{\kappa_0},$$

with the characteristic atomic species-dependent param-

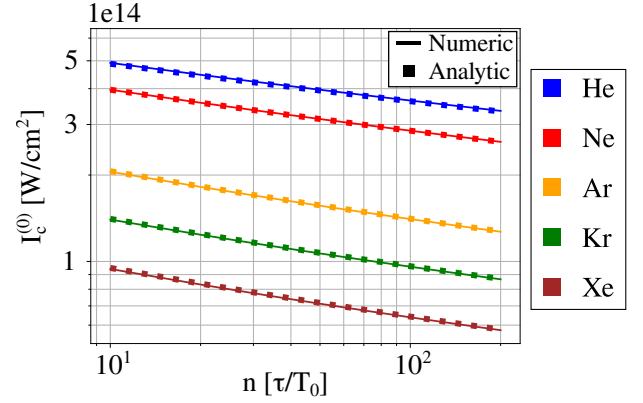


Figure 1: The critical intensity $I_c^{(0)}$, computed as a function of the pulse duration $\tau = nT_0$ which is measured in multiples of the optical period n . The ionization rates are computed within the ADK model for a wavelength of $\lambda = 1000$ nm in neutrally charged noble gases (color) [2].

ters κ_0, g_0, F_0 that are given by

$$\kappa_0 = 3^{g_0+1} \frac{|C_{n^* \ell^*}|^2 G_{\ell 0} I_p}{2\ell + 1},$$

$$g_0 = 2n^* - 2, \quad F_0 = \frac{2}{3} (2I_p)^{3/2}.$$

Here, each noble gas has an individual set of parameters that is predominantly determined by the ionization potential I_p of the respective atom. More details are presented in Ref. [2, 3]. The critical intensities (vertical axis) are illustrated in Fig. 1 for a linearly polarized Gaussian laser pulse with a set of commonly utilized noble gases. The full-width at half-maximum (FWHM) pulse duration $\tau = nT_0$ (horizontal axis) is represented by the number of optical cycles n . The presented formula of the critical intensity is highly accurate with an error of less than 1% and improves the computation time by 5 to 6 orders of magnitude.

References

- [1] R. Weissenbilder *et al.*, Nature Reviews Physics **4**, 713 (2022).
- [2] B. Minneker *et al.*, Photonics **10**, 24 (2022).
- [3] M. V. Ammosov *et al.*, Soviet Journal of Experimental and Theoretical Physics **64**, 1191 (1986).

*bjoern.minneker@uni-jena.de

Nondipole strong-field approximation for above threshold ionization in few-cycle pulse

D.F. Dar^{*1,2,3}, B. Minneker^{1,2,3}, and S. Fritzsche^{1,2,3}

¹HI Jena, Fröbelstieg 3, 07743 Jena, Germany; ²TPI, FSU Jena; ³GSI, Darmstadt

The ionization of atoms and molecules under strong laser fields has been studied both theoretically and experimentally. In particular, the strong-field approximation (SFA) has been used for theoretical studies. However, the SFA, which was derived for plane-wave beams, has limitations in predicting nondipole effects despite its effectiveness in explaining ionization processes. In this work, we extended the SFA that can handle the intricate temporal structure of short laser pulses. This extension enables better prediction of peak shifts and provides greater control over the laser field in inducing above-threshold ionization. Our findings indicate that the extension of SFA shows better agreement with experimental investigations than previous theoretical studies.

The interaction of atoms and molecules with high-intensity laser fields is a topic of significant interest. The time-dependent Schrödinger equation (TDSE) is used to study the complex behavior of atoms in such laser fields. Numerical, classical, and semiclassical methods are used for solving the TDSE, but the strong-field approximation (SFA) is a particularly intuitive and widely used method enabling to solve TDSE analytically.

Recently [2], femtosecond pulsed lasers have been used to examine nondipole-induced peak shifts in the momentum of the photoelectron, which have garnered significant attention in the field. Traditionally, SFA has been applied to laser fields under the dipole approximation. However, with new research [1], SFA has been extended to encompass nondipole scenarios, which has demonstrated its broad applicability.

In this work, we present an extension of the SFA that considers the complex temporal structure of a few-cycle pulse, which allows for the prediction of peak shifts in above-threshold ionization processes. The results demonstrate that the NSFA is a valuable theoretical method for calculating the effects of strong electromagnetic fields on the behavior of electrons. In particular, the NSFA with extension to few-cycle limit is better suited for predicting the peak shifts observed in experimental investigations. Overall, this study highlights the potential of the NSFA for providing enhanced control over the characteristics of laser pulses and better understanding the behavior of atoms in high-intensity laser fields.

This work has been funded by the Deutsche Forschungsgemeinschaft (DFG, German Research Foundation)—440556973 and by the Research School of Advanced Photon Science of HI Jena, Germany.

*danish.dar@uni-jena.de

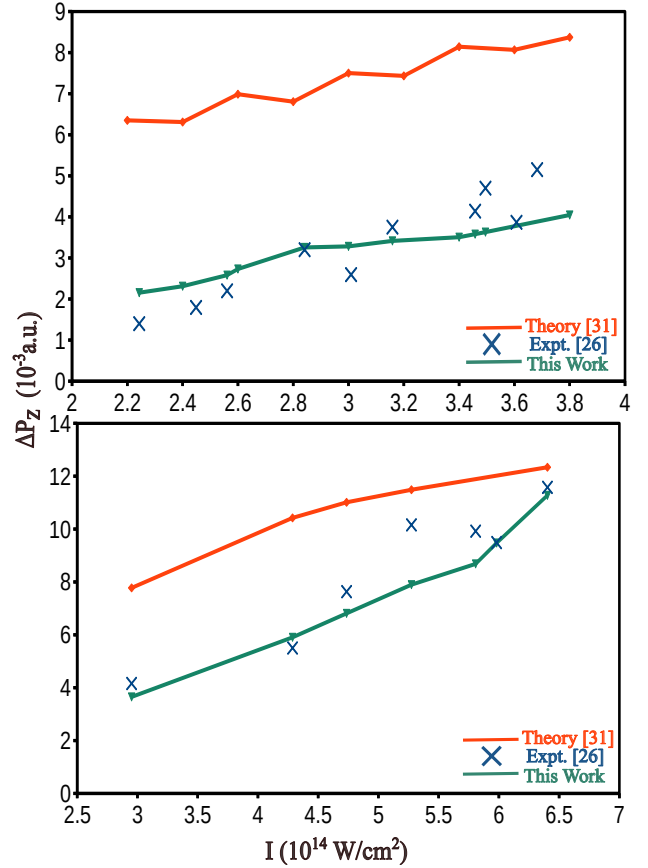


Figure 1: The peak shift ΔP_z of the maxima in ATI spectra are plotted as a function of laser intensity I for a circularly polarized 800 nm, 15 fs laser pulse. Results are shown for two different atomic targets, Ar (top) and Ne (bottom), and are compared to previous experimental (blue-crosses) and theoretical work: orange (Ref. [1]), blue (Ref. [2]), and green (this work).

References

- [1] B. Böning, W. Paufler, and S. Fritzsche, “Nondipole strong-field approximation for spatially structured laser fields,” *Phys. Rev. A* **99**, 053404 (2019). doi: 10.1103/PhysRevA.99.053404.
- [2] C. T. L. Smeenk, L. Arissian, B. Zhou, A. Mysyrowicz, D. M. Villeneuve, A. Staudte, and P. B. Corkum, “Partitioning of the Linear Photon Momentum in Multiphoton Ionization,” *Phys. Rev. Lett.* **106**, 193002 (2011). doi: 10.1103/PhysRevLett.106.193002.
- [3] D. F. Dar, B. Minneker, and S. Fritzsche, “Nondipole strong-field approximation for above threshold ionization in few-cycle pulse,” *Phys. Rev. A* (Accepted).

Partial-wave representation of the strong-field approximation — length versus velocity gauge

F. Liu^{*1,2,3} and S. Fritzsche^{1,2,3}

¹Helmholtz Institute Jena, Fröbelstieg 3, 07743 Jena, Germany; ²Theoretisch-Physikalisches Institut, Friedrich-Schiller-Universität Jena, 07743 Jena, Germany; ³GSI Helmholtzzentrum für Schwerionenforschung GmbH, 64291 Darmstadt, Germany

The strong-field approximation (SFA) is a commonly used model for ionization processes, which can be applied in both length gauge and velocity gauge. Recently, a reformulation of the SFA in terms of partial waves and spherical tensor operators was presented in Ref. [1], which supports a simple implementation and allows for the comparison of different treatments of the active (photo)electron and the laser pulses in velocity gauge. In this study, we extend this reformulation to rewrite the SFA in length gauge. Additionally, we compare the angular distributions (ADs) of above threshold ionization (ATI) in length and velocity gauge exposed to elliptical polarization laser pulses. By using the partial-wave representation of SFA, we calculate the ADs and find significant differences between the two gauges. Our results show that the ADs obtained from length gauge are more consistent with experimental results than those from velocity gauge, which highlights the importance of considering the gauge choice when using SFA to model ionization processes.

The strong-field approximation (SFA) is a commonly used theoretical model for studying ionization processes in atoms and molecules. However, several approaches have been suggested in order to overcome certain limitations of the original SFA formulation with regard to the representation of the initial bound and final continuum states of the emitted electron as well as a suitable description of the driving laser pulse. To overcome these limitations, a reformulation of the SFA in terms of partial waves and spherical tensor operators was proposed [1]. This reformulation simplifies the implementation of the SFA and allows for the comparison of different treatments of the active (photo)electron and the laser pulses in velocity gauge.

In this study, we extend the reformulation of the SFA to the length gauge and compare the angular distributions (ADs) of above-threshold ionization (ATI) in both gauges for different atoms exposed to elliptical polarization laser pulses. By using the partial-wave representation of the SFA, we calculate the ADs and find significant differences between the two gauges. Specifically, the ADs obtained from the length gauge are more accurate than those from the velocity gauge. Our results are consistent with previous experimental observations and highlight the importance of choosing the appropriate gauge when using the SFA to model ionization processes.

With this standard decomposition of (almost) all matrix elements in atomic-structure theory and by using the ellip-

tically polarized laser pulse (20), the direct transition amplitude can now be written

$$\begin{aligned} \mathbb{T}_0(\mathbf{p}) &= -i \int_{-\infty}^{\infty} d\tau \langle \chi_{\mathbf{p}+\mathbf{A}(\tau)}(\tau) | V_{\text{le}}(\mathbf{r}, \tau) | \Psi_i(\tau) \rangle \\ &= -i \sqrt{\frac{1}{2\pi}} \sum_{\ell_p=0}^{\infty} \sum_{m_p=-\ell_p}^{\ell_p} \sum_{q=0,\pm 1} \frac{(-1)^q u_q}{\sqrt{(2\ell_p+1)}} \\ &\quad \times Y_{\ell_p m_p}(\vartheta_p, \varphi_p) \langle \ell m, 1(-q) | \ell_p m_p \rangle \\ &\quad \times \int_{-\infty}^{\infty} d\tau E_c(\tau) e^{-i\epsilon_i \tau + iS_V(\tau)} \langle \epsilon_{\mathbf{p}+\mathbf{A}(\tau)} \ell_p | \hat{\mathbf{r}} | n\ell \rangle \\ &\quad - i \sqrt{\frac{1}{2\pi}} \sum_{\ell_p=0}^{\infty} \sum_{m_p=-\ell_p}^{\ell_p} \sum_{q=0,\pm 1} \frac{u_q^*}{\sqrt{(2\ell_p+1)}} \\ &\quad \times Y_{\ell_p m_p}(\vartheta_p, \varphi_p) \langle \ell m, 1q | \ell_p m_p \rangle \\ &\quad \times \int_{-\infty}^{\infty} d\tau E_c^*(\tau) e^{-i\epsilon_i \tau + iS_V(\tau)} \langle \epsilon_{\mathbf{p}+\mathbf{A}(\tau)} \ell_p | \hat{\mathbf{r}} | n\ell \rangle \end{aligned} \quad (1)$$

where we also introduced the complex-valued electric field $E_c(\tau)$ of an elliptically polarized laser pulse, and the reduced matrix elements of $\hat{\mathbf{r}}$ are given by

$$\begin{aligned} \langle \epsilon_{\mathbf{p}+\mathbf{A}(\tau)} \ell_p | \hat{\mathbf{r}} | n\ell \rangle &= \int d\mathbf{r} \frac{P_{\epsilon_{\mathbf{p}+\mathbf{A}(\tau)} \ell_p}(r)}{r} \langle \ell_p | \hat{\mathbf{r}} | \ell \rangle \frac{P_{n\ell}(r)}{r} \\ &= \langle \ell_p | \mathbf{C}^1 | \ell \rangle \int d\mathbf{r} \frac{P_{\epsilon_{\mathbf{p}+\mathbf{A}(\tau)} \ell_p}(r)}{r} r \frac{P_{n\ell}}{r} \\ &= -(2\ell_p+1)^{1/2} \langle \ell_p 0, 1 0 | \ell 0 \rangle \\ &\quad \times \int dr r P_{\epsilon_{\mathbf{p}+\mathbf{A}(\tau)} \ell_p}(r) P_{n\ell} \end{aligned} \quad (2)$$

In conclusion, our study shows that the reformulation of the SFA in terms of partial waves and spherical tensor operators is a useful tool for investigating ionization processes in both length and velocity gauges. Additionally, our findings emphasize the importance of gauge choice in accurately modeling the physics of strong-field ionization.

This work was supported by the Deutsche Forschungsgemeinschaft (DFG, German Research Foundation) under Project No. 440556973.

References

- [1] Birger Böning *et al.*, Phys. Rev. A. **102**, 053108 (2020).

*fang.liu@uni-jena.de

Accurate molecular *ab initio* calculations in support of strong-field attosecond physics experiments

G. Visentin^{*1,2}, B. Ying³, G. G. Paulus³, and S. Fritzsche^{1,2,3}

¹HI Jena, Fröbelstieg 3, 07743 Jena, Germany; ²GSI Helmholtzzentrum für Schwerionenforschung, 64291 Darmstadt, Germany ; ³Theoretisch-Physikalisches Institut, Friedrich-Schiller-Universität Jena, D-07743 Jena, Germany ,

An accurate *ab initio* molecular approach is proposed to model the potential energy curves of Ar_2^+ in the electronic ground and low-lying excited states across a wide interatomic distance range. The approach is targeted at supporting and validating strong-field physics experimental investigations of the attosecond dynamics for diatomic molecules and ions. The theoretical curves reasonably agree with the experimental and theoretical reference data, thus providing a valuable support to the experiments in the investigation of the attosecond dynamics of dissociating diatomics.

Experimental techniques exploiting strong-field processes allow to investigate the attosecond dynamics of molecules, such as their fragmentation into atoms [1]. Such experiments consist of an initial step, where the molecule is ionized, followed by its fragmentation. In turn, fragmentation may occur by means of two competing mechanisms, i.e., dissociation by recollision with the ejected electron [2] or dissociation of the molecular ion [1]. Evaluation of these two mechanisms is a crucial step in the experimental understanding of the molecular dissociation dynamics.

Accurate *ab initio* computations of the potential energy curves (PECs) for the molecular ions may provide a valuable tool in support of the experiments. In this work, we propose an accurate *ab initio* molecular approach to model the PECs of Ar_2^+ in the ground and lowest-lying excited electronic states. The PECs are constructed across a wide interatomic distance range up to the molecular dissociation limit. The approach is based on the relativistic Fock-Space Coupled Cluster (FS-CC) level of theory, with the iterative treatment of the single and double electron excitations (FS-CCSD), as implemented in the DIRAC [3] quantum chemistry package. In Figures 1 and 2 the PECs of the ground electronic state of Ar_2 and the ground and lowest-lying excited states of Ar_2^+ are presented.

The PECs computed with this approach are in good agreement with the available theoretical literature and remarkably support the experimental interpretation and investigation of the molecular dissociation pathways. This computational work is part of a theoretical and experimental collaboration aimed at investigating the attosecond dynamics of Ar_2 upon strong-field ionization.

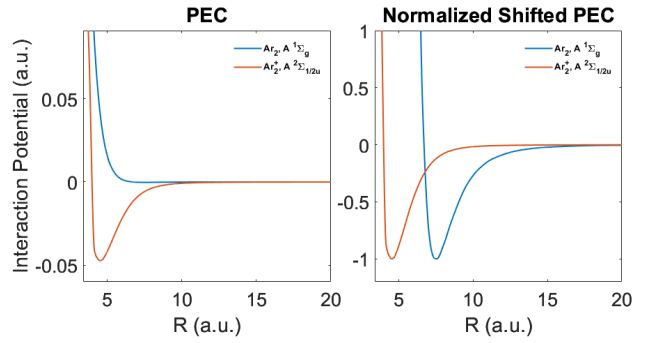


Figure 1: PECs of the electronic ground states of Ar_2 and Ar_2^+ . In the right inset the PECs are shifted by the corresponding asymptotic limit and normalized by the minimum value, in order to compare the equilibrium distances.

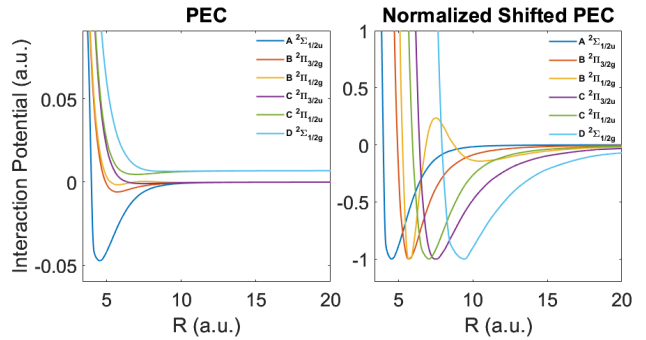


Figure 2: PECs of the electronic ground and the lowest-lying even-parity excited states of Ar_2^+ . In the right inset the PECs are shifted by the corresponding asymptotic limit and normalized by the minimum value, in order to compare the equilibrium distances.

References

- [1] T. Rathje, A.M. Sayler, S. Zeng *et al.*, Phys. Rev. Lett. **111**, 093002 (2013).
- [2] H. Niikura, F. Legaré, R. Hasbani *et al.*, Nature **417**, 917-922 (2002).
- [3] DIRAC, a relativistic *ab initio* electronic structure program, Release DIRAC23 (2023), written by R. Bast, A. S. P. Gomes, T. Saue *et al.*, (see <http://www.diracprogram.org>).

*g.visentin@hi-jena.gsi.de

Spatiotemporal dynamics of positron-hydrogen scattering in one dimension

Li Guang Jiao^{*1,2,3}, Xiao Hu Ji¹, and Stephan Fritzsche^{2,3}

¹College of Physics, Jilin University, Changchun 130012, People's Republic of China; ²Helmholtz-Institut Jena, D-07743 Jena, Germany; ³GSI Helmholtzzentrum für Schwerionenforschung GmbH, D-64291 Darmstadt, Germany

The positron-atom scatterings include a special charge rearrangement process named the positronium (Ps) formation, where the incident positron scatters from the target atom, capture an electron to form a hydrogenlike Ps atom, and then leave the target ion. Most of previous theoretical work utilized the time-independent scattering theories and only focused on the transition amplitudes. In this work, we solve the time-dependent Schrödinger equation, however, in one dimension and focus on the spatiotemporal evolution of quantum dynamics in the positron-H scattering. The present work paves the way towards our future investigation on the laser-assisted positron-atom scattering.

The full-dimensional treatment of the time-dependent positron-H atom scattering requires six space dimensions (three for the positron and the other three for the electron) and one time dimension, which is a formidable task for the present computational resource. In this work, we introduce a one-dimension model for positron-H scattering [1]

$$H = \frac{1}{2}p_1^2 + \frac{1}{2}p_2^2 + V(x_1) - V(x_2) - V(x_1 - x_2),$$

where $V(x) = 1/\sqrt{x^2 + a^2}$ represents the soft-core Coulomb potential, in which $a = 1$ is used for both the initial H ($E_1^H = -0.6698$) and final Ps ($E_1^{Ps} = -0.5882$) atoms. The initial system wave function is given as a product of the positron wave packet (in Gaussian form) and the electron wave function (ψ_1) in the ground state of H atom

$$\Psi(x_1, x_2, t = 0) = \frac{1}{(2\pi\sigma^2)^{1/4}} e^{-\frac{(x_1 - x_0)^2}{4\sigma^2}} e^{ik_0 x_1} \psi_1(x_2).$$

The time-dependent Schrödinger equation is solved by using the split-operator method with fast Fourier transform technique. After a long-enough time propagation, the system wave function can be formally expanded as

$$\begin{aligned} \Psi(x_1, x_2) = & \sum_{n=1}^{\infty} \int_{-\infty}^{+\infty} b_n(k) \psi_n(x_2) \frac{1}{\sqrt{2\pi}} e^{ikx_1} dk \\ & + \sum_{n=1}^{\infty} \int_{-\infty}^{+\infty} c_n(k) \phi_n(x_2 - x_1) \frac{1}{\sqrt{2\pi}} e^{ik\frac{x_1+x_2}{2}} dk, \end{aligned}$$

where $\psi_n(x)$ and $\phi_n(x_2 - x_1)$ are the eigenstates of H and Ps atoms, respectively, and $|b_n(k)|^2$ and $|c_n(k)|^2$ represent the probabilities of target excitations and Ps formations.

Figure 1 displays the time evolution of the spatial probability density distributions of the electron and positron during the scattering. The positron wave packet splits into four

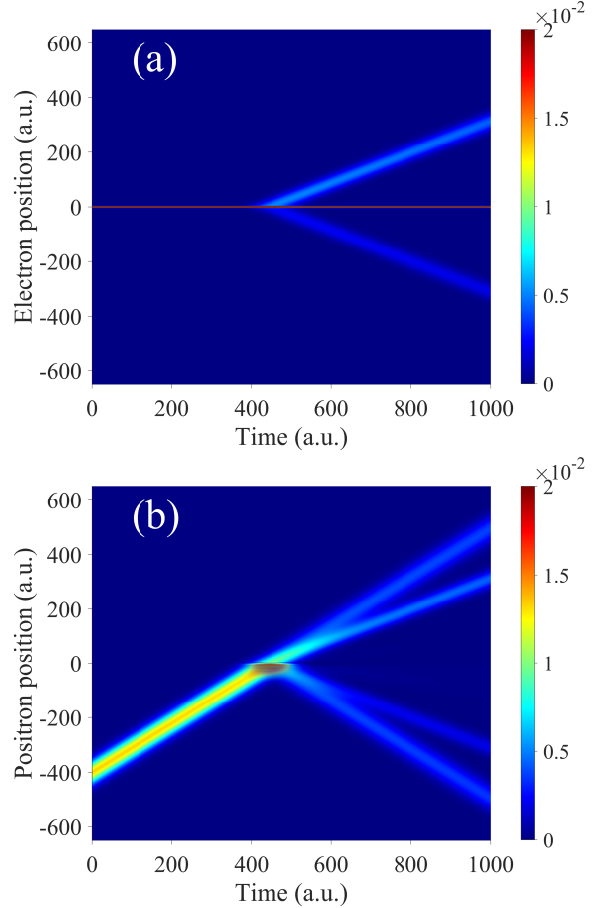


Figure 1: Spatial probability density distributions of the electron (a) and positron (b) as a function of time during the collision. The positron incident energy is 0.4 a.u., and the initial position of the positron is at -400 a.u.

parts with the outer two parts represent, respectively, the forward and backward direct scatterings. The inner two parts share the same moving speeds with the electrons and represent the forward and backward Ps formations. In the scattering region, strong interference fringes are observed which can be understood from the interference between the incident and reflected positron wave packets.

After introducing an intense linearly-polarized laser field, which restricts the motion of electron and positron to the polarization direction, the present model can be reasonably applied to the laser-assisted positron-atom scatterings.

References

- [1] Q. Su and J. H. Eberly, Phys. Rev. A **44**, 5997 (1991).

*lgjiao@jlu.edu.cn

QED approach to valence-hole excitation in closed shell systems

R. N. Soguel^{*1,2,3}, A. V. Volotka⁴, and S. Fritzsche^{1,3}

¹HI Jena, 07743 Jena, Germany; ²TPI, FSU Jena, 07743 Jena, Germany; ³GSI Helmholtzzentrum für Schwerionenforschung GmbH, 64291 Darmstadt, Germany; ⁴School of Physics and Engineering, ITMO University, 197101 St. Petersburg, Russia

An *ab initio* QED approach to treat a valence-hole excitation in closed shell systems is developed in the framework of the two-time-Green function method. The derivation considers a redefinition of the vacuum state and its excitation as a valence-hole pair. The proper two-time Green function, whose spectral representation confirms the poles at valence-hole excitation energies is proposed. An contour integral formula which connects the energy corrections and the Green function is also presented. First-order corrections to the valence-hole excitation energy involving self-energy, vacuum polarization, and one-photon-exchange terms are explicitly derived in the redefined vacuum picture. Reduction to the usual vacuum electron propagators is given that agrees in the Breit approximation with the many-body perturbation theory expressions for the valence-hole excitation energy.

Highly charged ions became a field of interest both from the theoretical and experimental sides. It has the great advantage to provide access to strong-field physics [1] and allow to probe quantum electrodynamics corrections up to the second-order in α (the fine structure constant) [2] although being a challenging task. Intensive experimental investigations have been carried over the years in a variety of system, ranging from H-like, He-like, Be-like, and Li-like to B-like and F-like ions (see [1] for a recent review of both experimental and theoretical sides). Increasing experimental precision pushes theoretical predictions to their limits and enforces an accurate description of complex electron dynamics. Over the years, many approximated methods have been devised to access higher-order corrections, however, *ab initio* calculations remain the holy grail in the quest for many-electron atoms in the frame of bound-state QED (BSQED).

Dealing with many-electron ions is a difficult task due to the numerical complexity involved as well as to derive formal BSQED expression. That is why *ab initio* calculations are limited so far to a few-electron ions [3] and ions with single valence (or hole) electron. To facilitate the derivation of the formal expressions for many-electron systems the redefinition of the vacuum state is widely used in the relativistic many-body perturbation theory [4]. However, within the BSQED it is not yet broadly employed. Previously, the vacuum redefinition method was employed within the BSQED mainly for single valence electron states [5] and recently for two-valence electron states [3]. In Ref. [6] we showed that the employment of the redefined vacuum state allows one to keep track of one-electron

gauge-invariant subsets into many-electron Feynman diagrams. Thus, several additional gauge-invariant subsets were identified. Later, we applied it to more sophisticated electron structures generalizing to either N valence electrons or N holes cases [7]. As an example, we presented the complete set of formal expressions for BSQED corrections up to the second-order in α for the single-hole picture [7]. Thus, the situation when both valence electrons and holes are involved in the description of a state has not been considered so far within the vacuum redefinition method.

The aim of the paper [8] is to provide a rigorous *ab initio* derivation of the BSQED perturbation theory for a valence-hole excitation in a closed shell system with the redefined vacuum approach. The two-time Green function formulation of the BSQED theory [5] is employed as a mathematical tool for our derivation. The notion of a redefined vacuum state is used from the very beginning. It is shown that with the appropriate equal times choice conditions a Green function having the proper two-body state normalization in the non-interacting field limit can be constructed. Its spectral representation identifies poles at the valence-hole excitation energies and the integral formula for the energy correction to the binding energy is obtained. The latter expression is expanded to the first order, where one-particle radiative and one-photon exchange corrections are explicitly derived.

The theoretical investigations presented were supported by BMBF grant 05P21SJFAA within the project 05P2021 (ErUM-FSP T05), and by the Russian Science Foundation (Grant No. 22-12-00258). A.V.V. acknowledges financial support from the government of the Russian Federation through the ITMO Fellowship and Professorship Program.

References

- [1] P. Indelicato, J. Phys. B, **52**, 232001 (2019).
- [2] V. A. Yerokhin, P. Indelicato and V. M. Shabaev, Phys. Rev. A **77**, 062510 (2008).
- [3] A. V. Malyshev *et al*, Phys. Rev. Lett. **126**, 183001 (2021).
- [4] W. R. Johnson, Atomic Structure Theory. Lectures on Atomic Physics, Springer-Verlag, Berlin, Heidelberg (2007).
- [5] V. M. Shabaev, Phys. Rep. **356**, 119 (2002).
- [6] R. N. Soguel, A. V. Volotka, E. V. Tryapitsyna, D. A. Glazov and S. Fritzsche, Phys. Rev. A **103**, 042818 (2021).
- [7] R. N. Soguel, A. V. Volotka, D. A. Glazov and S. Fritzsche, Symmetry **13**(6), 1014 (2021).
- [8] R. N. Soguel, A. V. Volotka and S. Fritzsche, Phys. Rev. A **106**, 012802 (2022).

* r.soguel@uni-jena.de

Detecting the oscillating magnetic field using the vector twisted light atom interaction

S. Ramakrishna^{*1,2,3}, R.P. Schmidt^{4,5}, A.A. Peshkov^{4,5}, A. Surzhykov^{4,5,6}, and S. Fritzsche^{1,2,3}

¹HI Jena, Fröbelstieg 3, 07743 Jena, Germany; ²GSI, Darmstadt; ³TPI, FSU Jena; ⁴PTB, Braunschweig; ⁵TU, Braunschweig; ⁶LENA, Braunschweig

We present a new theoretical approach to probe the frequency and strength of the oscillating magnetic field based on the vector twisted light-atom interaction. That is, we study the photoexcitation of ^{87}Rb atoms by vector Bessel beams in the framework of density matrix theory and based on the Liouville-von Neumann equation. In particular, we consider an electric dipole transition [$5s\ ^2S_{1/2}\ (F=1) \rightarrow 5p\ ^2P_{3/2}\ (F=0)$] and analyze the effect of an oscillating magnetic field on the population of excited state. We show that the population of the excited state is sensitive to the position of the atom in the beam cross section. Furthermore, we calculate the population of the excited state in the beam cross section of the vector twisted light beam for various frequencies, and strengths of the oscillating magnetic field. The results of our calculation can therefore be used to determine the frequency and the strength of the oscillating magnetic field.

The detection of frequency and strength of the oscillating magnetic field plays an essential role in experimental techniques such as nuclear magnetic resonance imaging (NMR) and magnetic resonance imaging (MRI). Currently, atomic magnetometers are a promising candidate for measuring the frequency and strength of oscillating magnetic fields. The atomic magnetometers can be helpful in the implementation of low- to moderate magnetic field (1-1000 G) MRI and NMR experimental techniques [1]. In addition, this can be helpful in reducing the role of superconducting magnets which may also lower the cost of such experimental techniques. The traditional atomic magnetometers designed to detect the oscillating magnetic field works on the principle of nonlinear magneto-optical rotation (NMOR). In this scheme, the detection of the oscillating magnetic field is carried out predominantly in the time domain [2].

In a recent experiment, F. Castellucci *et al.* [3] used the vector twisted light atom interaction process to detect the 3D alignment of the magnetic field. The vector twisted light beams are linear combinations of two circularly polarized twisted light beam. These beams possess polarization singularities in addition to the phase singularity. Also, the interaction of vector twisted light beams with atoms can be helpful in many areas like quantum memories, quantum metrology, quantum communication and many more.

In this work, we develop a theoretical model to detect the frequency and strength of the oscillating magnetic field using the interaction of vector Bessel beams and cold ^{87}Rb atoms in the presence of magnetic field. That is, we consider a constant and an oscillating magnetic field which are

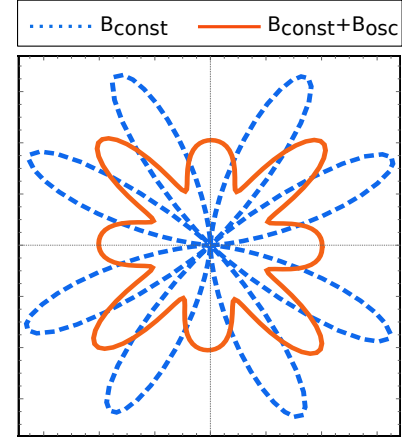


Figure 1: The time averaged excited state population of the ^{87}Rb atoms in the beam cross section of the vector Bessel beam is plotted for two different cases. The blue dotted lines show the plot for constant magnetic field only. The orange solid line shows the plot when the oscillating magnetic field is present in addition to the constant magnetic field. The strength of both constant and oscillating magnetic field is chosen to be 1 G and the frequency of the oscillating magnetic field is 10 kHz.

perpendicular to each other. In particular, we study the photoexcitation process in ^{87}Rb atoms driven by vector Bessel beam. We consider an electric dipole transition [$5s\ ^2S_{1/2}\ (F=1) \rightarrow 5p\ ^2P_{3/2}\ (F=0)$] and analyze the excited state population in the ^{87}Rb atoms. To perform this analysis, we use the Liouville-von Neumann equation in the density matrix formalism.

We observe that the population of the excited state is sensitive to the position of the target atom in the beam cross section of the vector Bessel beam. Furthermore, we calculate the time averaged excited state population in the beam cross section; see Fig. 1. This plot changes significantly with the frequency and strength of the oscillating magnetic field. Thus, this result can be used to detect the frequency and strength of the oscillating magnetic field in the spatial rather than in time domain.

The authors acknowledge funding from Research School of Advanced Photon Science (RS-APS) of Helmholtz Institute Jena, Germany.

References

- [1] I. M. Savukov *et al.*, L. Magn. Reson. **185**, 214 (2007).
- [2] M. P. Ledbetter *et al.*, Phys. Rev. A. **75**, 023405 (2007).
- [3] F. Castellucci *et al.*, Phys. Rev. Lett. **127**, 233202 (2021).

* shreyas.ramakrishna@uni-jena.de

p-Wave resonances in exponential cosine screened Coulomb potential

Yuan Cheng Wang^{*1,3,4}, Li Guang Jiao^{†2,3,4}, and Stephan Fritzsche^{3,4}

¹College of Physical Science and Technology, Shenyang Normal University, Shenyang 110034, China; ²College of Physics, Jilin University, Changchun 130012, China; ³Helmholtz-Institut Jena, D-07743 Jena, Germany; ⁴GSI Helmholtzzentrum für Schwerionenforschung GmbH, D-64291 Darmstadt, Germany

The p-wave resonances in the exponential cosine screened Coulomb potential are studied using the uniform complex-scaling generalized pseudospectral method. It is found that the resonance will be disturbed by an adjacent resonance when they have same position.

The exponential cosine screened Coulomb potential (ECSCP) has been extensively employed in modeling the strongly-coupled dense quantum plasmas. Different approaches have been developed in the literature to investigate the resonance states of one-electron atoms under ECSCP [1, 2]. In this work, we apply the uniform complex-scaling generalized pseudospectral (UCS-GPS) method [3] to predict the resonance energies with high accuracy.

The non-relativistic radial Schrödinger equation for the one-electron system under ECSCP is given by

$$\left[-\frac{1}{2\mu} \frac{d^2}{dr^2} + \frac{l(l+1)}{2\mu r^2} + V(\lambda, r) \right] \psi_{nl}(r) = E_{nl}(\lambda) \psi_{nl}(r),$$

where the potential reads

$$V(\lambda, r) = -\frac{Z}{r} e^{-\lambda r} \cos(\lambda r),$$

in which λ represents the screening parameter.

In the uniform complex-scaling method, the radial coordinates in the Hamiltonian are rotated by an angle θ , i.e., $r \rightarrow r e^{i\theta}$. The system eigenenergies are then rotated into the complex energy plane, where the bound state energies do not change, the continua are rotated down by an angle 2θ , and the resonance pole can be exposed from the continuum by acquiring a complex energy

$$E_{\text{res}} = E_r + iE_i = E_r - i\frac{\Gamma}{2},$$

where E_r and Γ are the resonance position and width, respectively.

Figure 1 shows the variation of eigenenergies for the np states with $n = 2 - 10$ along with changing the screening parameter. Each bound state with negative energy transforms into a shape resonance located above the threshold at the critical screening parameter with increasing λ . It is surprisingly found that there exists specific values of screening parameter at which two adjacent resonances go across with each other, with the lower-lying resonance is slightly disturbed by the higher-lying one.

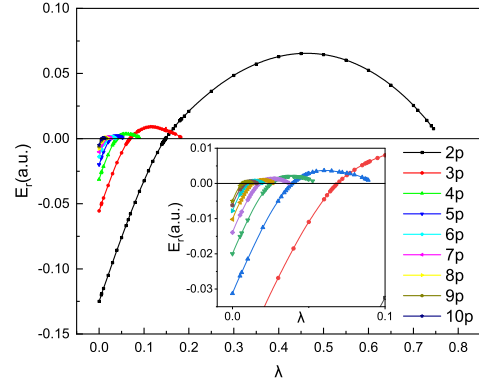


Figure 1: p-wave resonance positions and bound state energies for states with $n=2-10$.

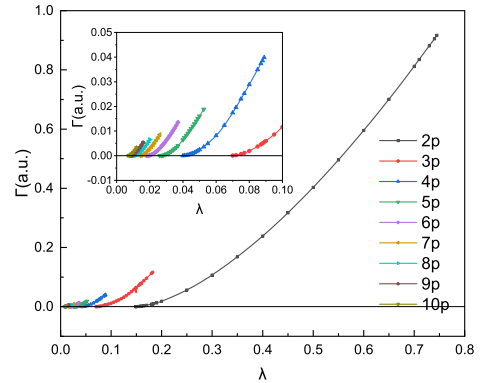


Figure 2: p-wave resonance width for states with $n=2-10$.

Figure 2 displays the resonance width Γ for the same states as those in Fig. 1. All resonance widths increase monotonically as λ is increased from the corresponding critical screening parameters. So far we are not able to trace the complete trajectories of the resonances due to the restriction of rotational angle in the UCS-GPS method.

References

- [1] I. Nasser, M. S. Abdelmonem, and A. Abdel-Hady, Phys. Scr. **84**, 045001 (2011).
- [2] H. Bahlouli, M. S. Abdelmonem, and S. M. Al-Marzouq, Chem. Phys. **393**, 153 (2012).
- [3] L. G. Jiao *et al.*, Eur. Phys. J. D **75**, 313 (2021).

*rickywangyc@aliyun.com

†lgjiao@jlu.edu.cn

Novel signatures of radiation reaction in electron–laser side scattering

P. Sikorski*¹ and D. Seipt¹

¹HI Jena, Fröbelstieg 3, 07743 Jena, Germany

We have studied signatures of radiation reaction in 90 degree scattering between the electron beam and laser. It is shown that the angular distribution of the electrons after the interaction with the laser can be controlled by tailoring the shape of the laser pulse. This is a novel manifestation of radiation reaction in addition to the well-known radiative energy loss.

The phenomenon of radiation reaction describes the fact that accelerated charged particles emit radiation which carries away energy and momentum and, hence, the radiation emission must act back onto the motion of the particles. A correct treatment of particle dynamics thus must include the back-reaction of the radiation on the motion of the particles [1].

In this work we consider the 90 degree scattering of an electron beam and a plane-wave laser pulse. We find, analytically and by computer simulations, that radiation reaction effects cause a deflection of the electrons up-stream or down-stream the laser, the direction of which can be controlled by varying the shape of the laser pulse. Without radiation reaction effect there cannot be any deflection of the electrons due to the Lawson-Woodward theorem.

Classical radiation reaction can be described by the Landau-Lifshitz equation [2],

$$\frac{du^\mu}{d\tau} = -\frac{e}{m} F^{\mu\nu} u_\nu + \frac{e^4}{6\pi m} \left[-\frac{m}{e} (\partial_\alpha F^{\mu\nu}) u_\nu u^\alpha + F^{\mu\nu} F_{\nu\alpha} u^\alpha + (F^{\nu\alpha} u_\alpha)^2 u^\mu \right], \quad (1)$$

where u is the four-velocity, $F^{\mu\nu}$ is the electromagnetic field strength tensor, and τ is proper time. The Landau-Lifshitz equation can be solved exactly analytically if the external field is a plane electromagnetic wave [3].

In our interaction scenario the electron beam initially propagates along the y -axis, and the laser beam propagates along the negative x -axis and is linearly polarized along the y -axis, i.e. $eF_{\mu\nu} = ma_0 f'(\phi)(k_\mu \varepsilon_\nu - k_\nu \varepsilon_\mu)$ with a_0 the normalized vector potential. Employing the analytical solutions we find the electron deflection angle as

$$\tan \theta = \frac{u_x}{u_y} \simeq -\frac{2}{3} \frac{\alpha a_0^3}{a_S} H_1, \quad (2)$$

where $a_S = 329677$ is the normalized Schwinger vector potential. From this we can deduce the important findings: (i) the deflection angle is independent of the initial electron energy (ii) a_0 must be large enough and (iii) the function $H_1(\phi) = \int_{-\infty}^{\infty} f'(\phi) I(\phi) d\phi$, with $I(\phi) = \int_{-\infty}^{\phi} f'(\psi)^2 d\psi$,

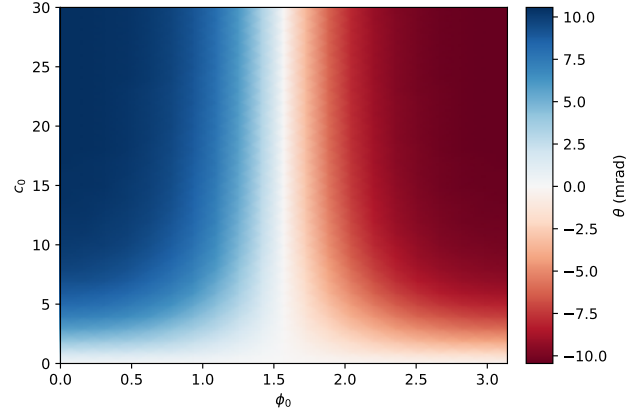


Figure 1: Analytic results for the electron scattering angle as function of c_0 and ϕ_0 for $a_0 = 30$ and $\gamma_0 = 200$.

must not be small. Especially the latter shows how the temporal shape of the laser electric field $f'(\phi)$ determines the sign and value of the electron scattering angle. In order to control the electron beam deflection we have considered several cases where the laser pulse shape can be controlled precisely: (i) few-cycle pulses with carrier-envelope-phase control, (ii) two-color pulses with variable strength of the second harmonic and relative phase, and (iii) addition of a low-frequency (sub-harmonic) component of the form

$$f = \frac{1}{N} \cos^4 \left(\frac{\phi}{2L} \right) \left[\cos(\phi) + c_0 \cos \left(\frac{\phi + \phi_0}{2L} \right) \right], \quad (3)$$

where L is the pulse duration, and ϕ_0 (c_0) is the relative phase (amplitude) of the subharmonic. As can be seen in Fig. 1, by changing ϕ_0 and c_0 we can obtain either positive or negative scattering angles on the order of 10 mrad.

In addition to the analytical results we have performed Monte Carlo simulations of the interaction using the particle-in-cell code SMILEI [4]. The centroid of the Monte-Carlo results agrees reasonably well with the analytics. In order to assess the experimentally observability of this novel signal of radiation reaction we will next perform full-scale 3D simulations of the interaction.

References

- [1] J. D. Jackson, Classical Electrodynamics, Wiley, NY (1999).
- [2] L. D. Landau and E. M. Lifschits. Course of Theoretical Physics, vol. 2, (1975).
- [3] A. Di Piazza, Lett. Math. Phys. **83**, 305–313 (2008).
- [4] J. Derouillat *et al.*, Phys. Commun. **222**, 351-373 (2018).

*philipp.sikorski@uni-jena.de

Linear polarization and angular distribution of the Lyman- α_1 line following electron-impact excitation of H-like ions

Z. W. Wu^{*1,2,3}, Z. M. He¹, C. Z. Dong¹, and S. Fritzsche^{2,3,4}

¹Northwest Normal University, Lanzhou, P. R. China; ²Helmholtz-Institut Jena, Germany; ³GSI Helmholtzzentrum für Schwerionenforschung GmbH, Darmstadt, Germany; ⁴Friedrich-Schiller-Universität Jena, Germany

The linear polarization and angular distribution of the Lyman- α_1 line following electron-impact excitation of highly charged H-like ions were studied within the framework of the density matrix theory. A good consistency was obtained when compared with other available results. In particular, the effect of the Breit interaction on the linear polarization and angular distribution of the Lyman- α_1 line was discussed in detail.

Electron-impact excitation (EIE) of atoms and ions is one of the fundamental processes in astrophysical and laboratory plasmas, which is thus an important mechanism of inducing line emissions. During the past decades, the angular and polarization properties of characteristic lines following EIE of atoms and ions have been attracting a lot of attention. In light of the work of Reed *et al.* [1], we studied EIE of H-like Ti^{21+} , Mo^{41+} , Ba^{55+} , and Au^{78+} ions from their ground state level $1s_{1/2}$ to the excited level $2p_{3/2}$ as well as the subsequent Lyman- α_1 decay using the multi-configurational Dirac-Fock (MCDHF) method and the relativistic distorted-wave theory. The present calculations were performed without (NB) and with (B) the Breit interaction included, respectively.

It was found that the present results for partial EIE cross sections and linear polarization of the Lyman- α_1 line with only the Coulomb interaction included are different from those of Reed *et al.* [1]. In contrast, the present results agree well with those from the relativistic convergent close-coupling method [2]. As an example, we explored the linear polarization and angular distribution of the Lyman- α_1 line of H-like Ti^{21+} , Mo^{41+} , Ba^{55+} , and Au^{78+} ions [3]. Special attention was paid to the effect of the Breit interaction on both of them. The findings show that the Breit interaction makes the Lyman- α_1 line less linearly polarized for all the impact energies considered, and such an effect becomes more prominent with increasing impact energy and atomic number Z , respectively, as shown in Figure 1. For Au^{78+} ions, the Lyman- α_1 polarization behavior is altered qualitatively at the impact energy of about 4.2 times the excitation threshold due to the Breit interaction.

In addition, for high- Z Au^{78+} ions, the Lyman- α_1 photons are predominantly radiated under $\theta = 90^\circ$, i.e., perpendicularly to the impact electron beam, even at high impact energies for the NB case, as shown in Figure 2. However, the contribution of the Breit interaction causes a qualitative change in its angular emission pattern at the impact energy of about 5.0 times the excitation threshold, i.e., from a perpendicularly dominated emission pattern to a forward- and backward-dominated one.

* zhongwen.wu@nwnu.edu.cn

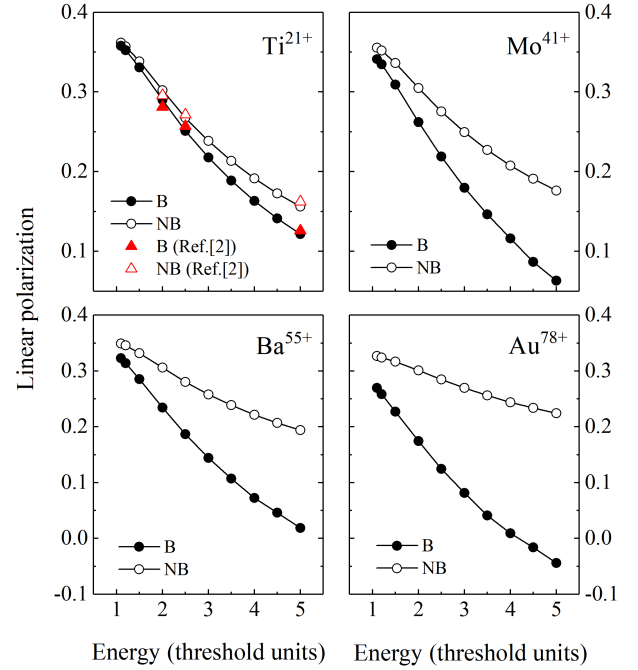


Figure 1: Linear polarization of the Lyman- α_1 line of Ti^{21+} , Mo^{41+} , Ba^{55+} , and Au^{78+} ions as a function of impact energy in units of their respective excitation thresholds, compared with the RCCC results of Ti^{21+} ions [2]. Results are given for both the NB and B cases.

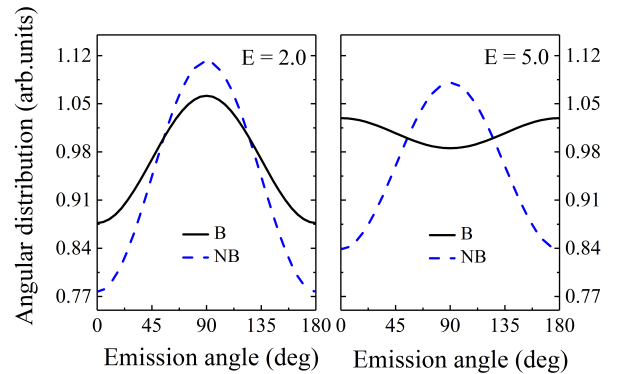


Figure 2: Angular distribution of Lyman- α_1 line radiated from Au^{78+} ions for two impact energies, i.e., 2.0 and 5.0 times the excitation thresholds. Results are shown for both the NB and B cases.

References

- [1] K. J. Reed *et al.*, Phys. Rev. A **48**, 3644 (1993).
- [2] C. J. Bostock *et al.*, Can. J. Phys. **89**, 503 (2011).
- [3] Z. W. Wu *et al.*, Phys. Rev. A **105**, 062813 (2022).

Improvement of the Locally Constant Field Approximation

N. Larin^{*1} and D. Seipt¹

¹HI Jena, Fröbelstieg 3, 07743 Jena, Germany

We propose a method of how to eliminate a divergence of the nonlinear Compton scattering in the locally constant field approximation (LCFA). In contrast to the exact strong field QED result (SFQED), LCFA manifests a soft-photon divergence in the limit of small light-front momenta. We derive a regularizing term by imposing an additional condition on the LCFA expressions in this limit, which ensures reasonable behavior in the problematic region. The advantage of the suggested approach is that it allows a numerically efficient implementation in the simulation codes.

The locally constant field approximation is a powerful tool for investigating the QED precesses within the strong external electromagnetic field of an arbitrary configuration [1]. Exploiting the concept of probability rate, it is possible, relatively simple, to find particles energy spectra [2] and their angular distributions [3]. Nowadays, because of the numerical efficiency, LCFA is widely implemented in the different numerical simulation codes [3,4]. The general idea behind the LCFA is that complicated external background can be treated locally as a constant crossed field, while certain conditions are hold. Namely, the main demand is to field be sufficiently strong ($a_0 = eE/m\omega \gg 1$), so one can make assumptions about the particles energies and formations length of the process. As long as this condition is fulfilled, it is possible to approximate the exact probability distribution as an incoherent sum of local probability rates ($R = dP/d\varphi$) within the constant crossed field, calculated in all points along the classical trajectory of the particle.

It is important to emphasize that the condition on the field strength is necessary, but not sufficient. For nonlinear Compton scattering (NCS) it was shown that LCFA fails even for the large field intensities [5]. And the reason is that for small light-front momenta $s = \kappa \cdot k / \kappa \cdot p$ the formation phase within the constant crossed field scales as $\sim 1/a_0 s^{1/3}$. Therefore, the spatial and temporal inhomogeneities of the external field are essential for the formation of soft photons, and the field can not be treated anymore as a constant and crossed even locally.

Unlike the LCFA, the exact SFQED result for the NCS within the plane wave background always stays finite [5]. So, the main idea of our method is to introduce the regularizing term s_* , which should provide the correct value in the small s limit. To derive the explicit expression for this term, we superimpose an additional condition. To wit, we demand that the limits of regularized LCFA and exact SFQED expression coincide, when $s \rightarrow 0$.

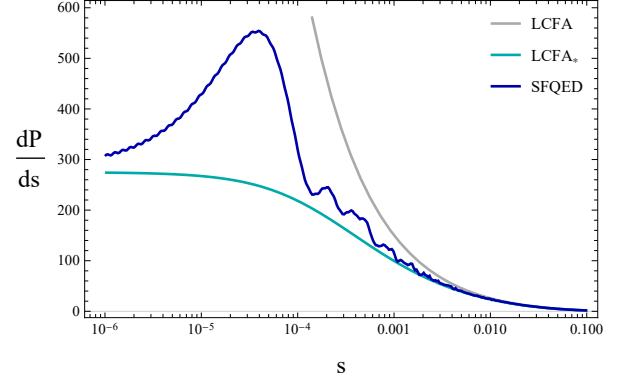


Figure 1: Comparison of the LCFA, LCFA_{*} and the exact SFQED result within the plane wave background for $a_0 = 10$ and $\gamma = 2000$.

$$\left. \frac{dR_{\text{LCFA}_*}}{ds} \right|_{s \rightarrow 0} \sim \frac{\alpha}{b} \left(\frac{\chi(\varphi)}{s_*} \right)^{2/3} \simeq \left. \frac{dR_{\text{exact}}}{ds} \right|_{s \rightarrow 0}. \quad (1)$$

To distinguish regular LCFA from the regularized one, we use the abbreviation LCFA_{*}. The Eq. (1) can be easily resolved analytically with respect to s_* , if we assume $s_* \ll 1$ for large a_0 . This assumption is justified by the fact that LCFA itself works perfectly for $s \sim 1$.

In Fig.1 we plotted comparison of NCS spectra obtained in LCFA, LCFA_{*} and also exact SFQED result. We considered the short pulsed plane wave with the envelope $g(\varphi) = \cos^2(\varphi/4\tau) \Theta(2\pi\tau - |\varphi|)$, linear polarization and duration $\tau = 4$. From Fig.1 we can see that LCFA_{*} manifests adequate behavior for small s and in principle should coincide with the exact SFQED result in the limit $s \rightarrow 0$. While LCFA always overestimates spectrum, LCFA_{*} underestimates it. Similarly to the LCFA, LCFA_{*} lacking the complicated harmonic structure due to neglecting the interference between emission in different points of a pulse. Nevertheless, LCFA_{*} can be considered as the extended version of LCFA, since it eliminates the divergence and allows for simple numerical implementations.

References

- [1] A. Di Piazza *et al.*, Phys. Rev. A **99**, 022125 (2019).
- [2] A. Ilderton *et al.*, Phys. Rev. A **99**, 042121 (2019).
- [3] T. G. Blackburn *et al.*, Phys. Rev. A **101**, 012505 (2020).
- [4] A. Gonoskov *et al.*, Phys. Rev. E **92**, 023305 (2015).
- [5] A. Di Piazza *et al.*, Phys. Rev. A **98**, 012134 (2018).

^{*}nikita.larin@uni-jena.de

All-optical quantum vacuum signals in two-beam collisions

Holger Gies^{1,2}, Felix Karbstein^{*1,2}, and Leonhard Klar^{1,2}

¹Helmholtz Institute Jena, Germany; ²Theoretisch-Physikalisches Institut, FSU Jena, Germany

Quantum field theory predicts the vacuum to resemble a polarizable medium. This gives rise to effective nonlinear interactions between electromagnetic fields and light-by-light scattering phenomena. We study the collision of two optical laser pulses in a pump-probe setup using beams with circular and elliptic cross section and estimate the number of discernible signal photons induced by quantum vacuum nonlinearities. Our central goal is to optimize the quantum vacuum signal discernible from the background of photons constituting the driving laser beams. We show that widening the focus typically improves the signal to background separation in the far field relatively to the case where both beams are maximally focused.

In Ref. [1], we study the prospects of inducing a discernible quantum vacuum signal in a two-beam pump-probe setup with optical ultrashort petawatt laser pulses. For a schematic illustration of the considered scenario, see Fig. 1. A key parameter to enhance the signal is the choice of optimal beam waists. Typically, laser beams focused as tightly as possible are considered in order to maximize the field strength in quantum vacuum experiments. While this does generically maximize the scattering amplitudes, it does not necessarily optimize the signal-to-background ratio which is the relevant quantity to identify the most prospective quantum vacuum signal for experiment. A crucial idea in this context is that the specific use of larger beam waists can scatter the quantum signal into lower-noise regions [2]. This can be traced back to the fact that the signal amplitude decreases only with a power law for increasing waists, whereas the background decreases exponentially in the relevant spacetime regions. In addition to studying beams with circular cross section, we also allow the probe pulse to have an elliptic focus cross section such as pioneered in the context of vacuum birefringence [3]. We discuss the advantages of the circularly or elliptically focused probe beam settings for variable probe beam waists and determine the respective number of discernible signal photons mediated by quantum vacuum nonlinearities.

For our quantitative predictions we focus on laser pulses in the optical regime featuring the same photon energy of $\omega_0 = 1.55$ eV, a pulse energy of $W = 25$ J and a pulse duration of $\tau_{\text{FWHM}} = 25$ fs. Considering collision angles in the range $100^\circ \leq \vartheta_{\text{col}} \leq 160^\circ$, we find a decisive dependence of the detectable signal strength in terms of *discernible* photons on the beam waist of the probe beam both for circular and elliptical beam cross section. For a mostly

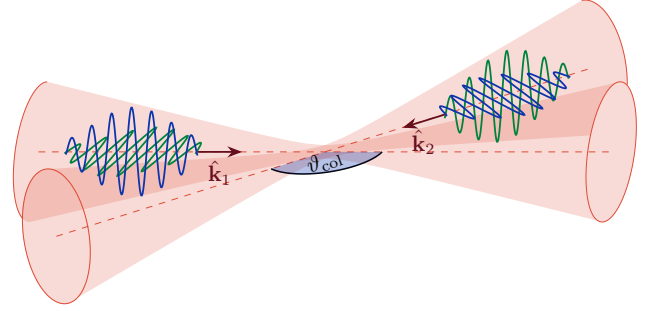


Figure 1: Illustration of the considered scenario. The red shades illustrate the forward/backward cones of two laser pulses colliding under an angle of ϑ_{col} . The wiggly curves are snapshots of the associated electric and magnetic fields.

analytically accessible and efficient theoretical modeling, the laser pulses are considered in the infinite Rayleigh range approximation. This allows for a controlled determination and analysis of discernible signals and their angular emission regimes in the considered parameter ranges.

The essential mechanisms become already visible for the simpler case of a probe beam with circular cross section. Namely, the maximization of the discernible signal requires a compromise between increasing the intensity in the interaction region and decreasing the background in the far field where the signals are to be detected. In the considered range of collision angles, we observe that the optimal beam waist is about $\sim 5 \dots 7$ times bigger than the one achievable in the diffraction limit. Our results are in line with those found for counter-propagating beams [2]. For the largest collision angle studied in Ref. [1] elliptical cross sections come with further means to increase the signal: suitable choices of the ellipticity can increase the intensity in the collision region while maintaining the background suppression in the detection region; see also Ref. [3].

This work has been funded by the DFG under Grant Nos. 392856280, 416607684, and 416611371 within the Research Unit FOR2783/2.

References

- [1] H. Gies, F. Karbstein and L. Klar, Phys. Rev. D **106**, 116005 (2022).
- [2] E. A. Mosman and F. Karbstein, Phys. Rev. D **104**, 013006 (2021).
- [3] F. Karbstein, H. Gies, M. Reuter and M. Zepf, Phys. Rev. D **92** 071301 (2015).

*f.karbstein@hi-jena.gsi.de

Direct accessibility of the fundamental constants governing light-by-light scattering

Felix Karbstein^{*1,2}, Daniel Ullmann^{1,3}, Elena A. Mosman^{1,2}, and Matt Zepf^{1,3}

¹Helmholtz Institute Jena, Germany; ²Theoretisch-Physikalisches Institut, FSU Jena, Germany; ³Institut für Optik und Quantenelektronik, FSU Jena, Germany

Quantum field theory predicts the vacuum to exhibit a non-linear response to strong electromagnetic fields. This fundamental tenet has remained experimentally challenging and is yet to be tested in the laboratory. We present proof of concept and detailed theoretical analysis of an experimental setup for precision measurements of the quantum vacuum signal generated by the collision of a brilliant x-ray probe with a high-intensity pump laser. Our proof-of-concept measurements show that the background can be efficiently suppressed by many orders of magnitude. This should facilitate a detection of both polarization components of non-linear vacuum response and provide direct access to the low-energy constants governing light-by-light scattering.

Vacuum fluctuations induce non-linear interactions of electromagnetic fields. This implies light-by-light scattering and violations of the superposition principle which predicts light rays to traverse each other without interacting. Within the Standard Model the leading effect is governed by quantum electrodynamics (QED), where a virtual electron-positron pair can couple electromagnetic fields. Macroscopic electromagnetic fields available in the laboratory fulfill $\{|\vec{E}|, c|\vec{B}|\} \ll E_S$, with $E_S = m^2 c^3 / (e\hbar) \simeq 1.3 \times 10^{18}$ V/m set by QED parameters: the electron mass m and elementary charge e . If these fields vary on scales much larger than $\lambda_C = \hbar / (mc) \simeq 3.8 \times 10^{-13}$ m, their leading interactions are governed by $(c = \hbar = 1)$ [1]

$$\mathcal{L}_{\text{int}} \simeq \frac{m^4}{1440\pi^2} \left[a \left(\frac{\vec{B}^2 - \vec{E}^2}{E_S^2} \right)^2 + b \left(\frac{2\vec{B} \cdot \vec{E}}{E_S^2} \right)^2 \right]. \quad (1)$$

The constants a and b control the strength of the four-field couplings. QED predicts these to have a series expansion in $\alpha = e^2 / (4\pi) \simeq 1/137$ and read [1, 2]

$$a = 4 \left(1 + \frac{40}{9} \frac{\alpha}{\pi} + \dots \right), \quad b = 7 \left(1 + \frac{1315}{252} \frac{\alpha}{\pi} + \dots \right). \quad (2)$$

A famous prediction of Eq. (1) is vacuum birefringence: linearly polarized probe light traversing a pump field can obtain a \perp -polarized component and become elliptical. Progress in laser technology has resulted in realistic concepts to detect this effect in head-on laser pulse collisions for the first time. In this scenario, typically the number of \perp -polarized photons N_{\perp} , a subset of the total signal $N_{\perp} + N_{\parallel}$, constitutes the observable. The scaling

$$N_{\parallel, \perp} \sim c_{\parallel, \perp} \left(\frac{I}{I_S} \frac{\omega}{m} \right)^2 N, \quad (3)$$

*f.karbstein@hi-jena.gsi.de

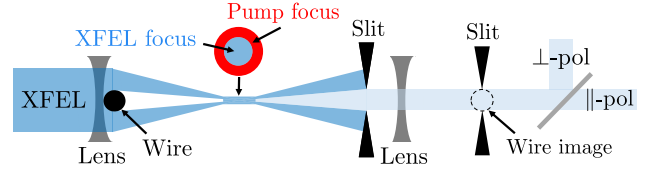


Figure 1: Schematic layout of an experiment to measure a and b . The XFEL is focused to a spot with a wire creating a central shadow in the beam on both sides of the focus while retaining a central intensity peak in the focus. X-ray optics image the wire to a matched aperture plane. The interaction with the pump results in a signal scattered into the central shadow. The \perp , \parallel -polarized components are directed to separate detectors using a crystal polarizer.

with the pump intensity I and the probe photon energy ω (number N) suggests the use of an XFEL as probe and a tightly focused high-intensity laser as pump for this experiment; $I_S = E_S^2$. The coefficients $c_{\parallel} = [a + b + (a - b) \cos(2\phi)]^2$ and $c_{\perp} = [(a - b) \sin(2\phi)]^2$ depend on a , b and the relative polarisation ϕ of pump and probe; the ratio c_{\perp}/c_{\parallel} depends on ϕ and $(a + b)/(a - b)$.

Detecting both $N_{\parallel, \perp}$ allows a and b to be inferred. As these depend on the driving fields in the same way, a simultaneous detection provides access to the ratio

$$\frac{N_{\perp}}{N_{\parallel}} \Big|_{\phi=\frac{\pi}{4}} \simeq \left(\frac{a - b}{a + b} \right)^2 = \frac{9}{121} \left(1 + \frac{260}{99} \frac{\alpha}{\pi} + \dots \right). \quad (4)$$

This observable does not depend on intensity and thus is insensitive to fluctuations in experimental parameters such as spatio-temporal jitter or intensity fluctuations that typically limit the achievable precision in experiments requiring the overlap of pump and probe foci.

In Ref. [3], we combine the results of a first-principles calculation and a proof-of-concept experiment to show that the dark field scheme devised by us (see Fig. 1) is capable of determining both a and b . Such a measurement could, e.g., be performed at the Helmholtz International Beamline for Extreme Fields (HIBEF) at the European XFEL.

This work has been funded by the DFG under Grant Nos. 416607684; 416702141; 416708866 within the Research Unit FOR2783/1.

References

- [1] W. Heisenberg and H. Euler, Z. Phys. **98**, 714 (1936).
- [2] V. Ritus, J. Exp. Theor. Phys. **42**, 774 (1975).
- [3] F. Karbstein, D. Ullmann, E. A. Mosman and M. Zepf, Phys. Rev. Lett. **129**, 061802 (2022).

Large N external-field quantum electrodynamics

Felix Karbstein^{*1,2}

¹Helmholtz Institute Jena, Germany; ²Theoretisch-Physikalisches Institut, FSU Jena, Germany

We advocate the study of external-field quantum electrodynamics with N charged particle flavors. Our main focus is on the Heisenberg-Euler effective action for this theory in the large N limit which receives contributions from all loop orders. In this case all contributions beyond one loop stem from one-particle reducible diagrams. We show that specifically in constant electromagnetic fields the large N Heisenberg-Euler effective action can be determined explicitly at any desired loop order and study the strong field behavior of the theory.

In Ref. [1] we study quantum electrodynamics (QED) with N charged particle flavors of equal charge e and mass m in the presence of a prescribed external electromagnetic field \bar{A} . This theory resembles standard QED but features N generations of electrons and positrons coupling to the electromagnetic field via the charge e . Throughout this work we choose this coupling such that the combination Ne^2 does not change with N . This choice implies $e \sim N^{-1/2}$. To arrive at a meaningful deformation of standard external-field QED we moreover demand $\bar{A} \sim N^{1/2}$, which guarantees that $e\bar{A} \sim N^0$ [3]. Without this additional assumption, the considered theory would generically be dominated by physics at zero field because $e\bar{A} \sim N^{-1} \rightarrow 0$ for sufficiently large values of $N \gg 1$.

This generalization of standard external-field QED constitutes an interesting deformation of the original theory. The flavor number N in particular provides a new parameter allowing to organize Feynman diagrams contributing to a given quantity by classifying them in terms of their scaling with N . Reference [1] focuses on the emergence and structure of the Heisenberg-Euler effective action [2] for this theory in the large N limit, characterized by $N \rightarrow \infty$ while keeping $Ne^2 = \text{const.}$ and $e\bar{A} = \text{const.}$ fixed.

The microscopic Lagrangian of external-field QED with N fermion generations can be cast into the form,

$$\mathcal{L} = \bar{\psi}(i\mathcal{D}[\bar{A} + q] - m)\psi - \frac{1}{4}\bar{F}_{\mu\nu}\bar{F}^{\mu\nu} - \frac{1}{4}Q_{\mu\nu}Q^{\mu\nu}, \quad (1)$$

with gauge covariant derivative $D_\mu[A] = \partial_\mu - ieA_\mu$, $\mathcal{D} = \gamma^\mu D_\mu$ and gamma matrices γ^μ . Here, the scalings $e^2 \sim N^{-1}$ and $e\bar{F} \sim e\bar{A} \sim N^0$ and the notation $\bar{\psi}(\cdot)\psi = \sum_{i=1}^N \bar{\psi}^{(i)}(\cdot)\psi^{(i)}$, where i labels the fermion flavors, are implicitly understood. In the present context $\psi^{(i)}$ and q denote quantized spinor and gauge fields, and \bar{A} is the four-potential of the prescribed non-quantized external field. The associated field strength tensors are $\bar{F}^{\mu\nu} = \partial^\mu \bar{A}^\nu - \partial^\nu \bar{A}^\mu$ and $Q^{\mu\nu} = \partial^\mu q^\nu - \partial^\nu q^\mu$. For

$N = 1$ and $\bar{A} \rightarrow 0$ the Lagrangian of standard QED at zero field is recovered.

The Feynman rules of N flavor external-field QED resemble those of standard QED. As conventionally done in studies of standard QED subjected to a prescribed classical field, the action of the external field \bar{A} on the dynamics of the theory can be fully encoded in dressed fermion propagators. The resulting fermion propagator accounts for the dressing of the fermion line to all orders in the classical field $e\bar{A} \sim N^0$. At the same time, each fermion loop comes with an overall factor of N as quantum fluctuations generically encompass all degenerate fermion flavors. On the other hand a coupling to the quantum photon field is mediated by the elementary charge and thus comes with a factor of $e \sim N^{-1/2}$. This directly implies a factor of N^{-1} for each internal photon line. In turn, the one-loop Heisenberg-Euler effective action [2] scales as $\Gamma_{\text{HE}}^{1\text{-loop}} \sim N$, and all higher-loop one-particle irreducible contributions are parameterically suppressed relatively to this contribution by at least one power of N^{-1} .

A distinct difference between external-field and standard zero-field QED is the emergence of finite physical tadpole contributions: due to the dressing in the external field, e.g., a tadpole formed by a fermion loop contracted with a single photon line constitutes a viable, generically non-vanishing building block to a Feynman diagram describing a given process. Upon connection to another fermion line this particular tadpole contribution scales as $NN^{-1} = N^0$, and thus can be attached to any given diagram without changing its scaling with N . Precisely this property and the fact that they even persist to contribute in homogeneous constant electromagnetic fields makes such tadpole contributions constituent building blocks of the Heisenberg-Euler effective action in the large N limit which follows from the Lagrangian (1) upon integrating out the quantum fields as

$$e^{i\Gamma_{\text{HE}}[\bar{A}]} = \int \mathcal{D}q \int \mathcal{D}\bar{\psi} \int \mathcal{D}\psi e^{i\int \mathcal{L}}. \quad (2)$$

Reference [1] in particular lays the foundations for a future non-perturbative first-principles study of the large N Heisenberg-Euler effective action in arbitrarily strong constant electromagnetic fields.

This work has been funded by the DFG under Grant No. 416607684 within the Research Unit FOR2783/1.

References

- [1] F. Karbstein, JHEP **01**, 057 (2022).
- [2] W. Heisenberg and H. Euler, Z. Phys. **98**, 714 (1936).
- [3] F. Karbstein, Phys. Rev. Lett. **122**, 211602 (2019).

^{*}f.karbstein@hi-jena.gsi.de

Quantum vacuum processes in the extremely intense light of relativistic plasma mirror sources

Antonin Sainte-Marie¹, Luca Fedeli¹, Neïl Zaïm¹, Felix Karbstein^{*2,3}, and Henri Vincenti¹

¹Lasers, Interaction and Dynamics Laboratory, Université Paris-Saclay, CEA, CNRS, LIDYL, Gif-sur-Yvette, France;

²Helmholtz Institute Jena, Germany; ³Theoretisch-Physikalisches Institut, FSU Jena, Germany

The advent of petawatt-class laser systems allows generating electromagnetic fields of unprecedented strength in a controlled environment, driving increasingly more efforts to probe yet unobserved processes through their interaction with the quantum vacuum. In recent years plasma mirrors have emerged as a promising technology enabling the conversion of intense infrared laser pulses into coherently focused Doppler harmonic beams lying in the X-UV range. We present predictions on the quantum vacuum signatures produced when such beams are tightly focused, specifically light-by-light scattering phenomena and electron-positron pair creation. To this end we combine the vacuum emission picture with the model of a plasma-mirror-generated perfectly focused beam built from PIC-generated harmonics spectra.

Macroscopic electromagnetic fields are remarkably well described by Maxwell's theory of classical electrodynamics which allows conceiving a vacuum state in which all properties of the field derive from laws devoid of reference to any other physical system. Quantum field theory however reveals that all fundamental degrees of freedom come in the form of fields permeating all space and whose rest state can never be strictly assigned, so that an inert vacuum can in principle not exist nor a single field be in perfect isolation. Instead, each field constantly interacts with all the other ones through real or virtual states. As laser technology is making steady progress towards unprecedented intensities, the interaction of light with the quantum vacuum emerges as a prospective and promising probe for fundamental physics. Since the strongest macroscopic fields achievable to date, provided by femtosecond multi petawatt-class lasers focused near diffraction-limit, reach peak field strengths well below the critical electric field $E_S = m^2 c^3 / (e \hbar) \simeq 1.3 \times 10^{18} \text{ V/m}$ set by the electron mass m and charge e , the direct detection of nonperturbative quantum vacuum processes such as pair creation seems to be precluded in a foreseeable future. On the other hand, research efforts devoted to all-optical signatures of quantum vacuum nonlinearity have pointed out the yet elusive nature of this process together with the exciting possibility to attain a discernible signal in several field configurations.

In recent years, however, alternative paths have been breached to much stronger macroscopic fields. Among them, coherent harmonic focusing suggests to leverage on the Doppler frequency upshift of a high-power infrared laser pulse upon reflection off a curved relativistic plasma mirror, to compress its energy down to consider-

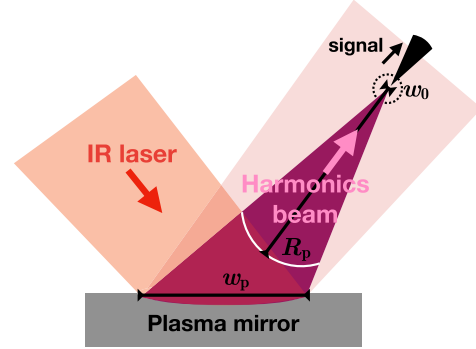


Figure 1: Schematic representation of a coherent harmonic focusing configuration. The driving intense infrared laser impinges on the plasma mirror surface with waist w_p and is reflected as a focused harmonics beam with curvature radius R_p and waist at focus w_0 . The resulting strong electromagnetic fields result in a nonlinear quantum vacuum response encoded in signal photons which are predominantly scattered into the forward cone of the harmonics beam.

ably smaller spatio-temporal volumes than those achievable with the original laser wavelength; cf., e.g., [3]. Extensive theoretical and numerical studies recently proposed realistic paths to implement such curved relativistic plasma mirrors with several techniques regarding the focusing of the harmonic beam. These studies robustly predict focused intensities ranging from 10^{24} W/cm^2 to more than 10^{28} W/cm^2 with multi-petawatt class laser systems. Despite these remarkable figures, such plasma-mirror-based configurations have been comparatively little studied as sources for quantum vacuum experiments.

In Ref. [2] a large scale state-of-the-art numerical tools able to realistically simulate such field configurations along the lines of Ref. [3] was developed. This allows for quantitative predictions of the quantum vacuum signals driven by the extremely intense fields generated by coherently focusing harmonics with plasma mirrors. One of the studied experimental scenarios is depicted schematically in Fig. 1.

FK has been funded by the DFG under Grant No. 416607684 within the Research Unit FOR2783/1.

References

- [1] A. Blinne, H. Gies, F. Karbstein, C. Kohlfürst and M. Zepf, Phys. Rev. D **99**, 016006 (2019).
- [2] A. Sainte-Marie, L. Fedeli, N. Zaïm, F. Karbstein and H. Vincenti, New J. Phys. **24**, 065005 (2022).
- [3] F. Karbstein, A. Blinne, H. Gies and M. Zepf, Phys. Rev. Lett. **123**, 091802 (2019).

*f.karbstein@hi-jena.gsi.de

Pauli-Term-Induced Fixed Points in d -dimensional QED

Holger Gies^{*1,2}, Kevin K.K. Tam^{2,3}, and Jobst Ziebell²

¹HI Jena, 07743 Jena, Germany; ²TPI, FSU Jena, 07743 Jena, Germany; ³MPS Photonics, 07745 Jena, Germany

We explore the fixed-point structure of QED-like theories upon the inclusion of a Pauli spin-field coupling. We concentrate on the fate of UV-stable fixed points recently discovered in $d = 4$ spacetime dimensions upon generalizations to lower as well as higher dimensions for an arbitrary number of fermion flavors N_f . As an overall trend, we observe that going away from $d = 4$ dimensions and increasing the flavor number tends to destabilize the non-Gaussian fixed points discovered in four spacetime dimensions. A notable exception is a non-Gaussian fixed point at finite Pauli spin-field coupling but vanishing gauge coupling, which also remains stable down to $d = 3$ dimensions, as is relevant for effective theories of layered condensed-matter systems. As an application, we construct renormalization group trajectories that emanate from the non-Gaussian fixed point and approach a long-range regime in the conventional QED₃ universality class that is governed by the interacting (quasi) fixed point in the gauge coupling.

The Pauli term, denoting the coupling between the electron spin and the electromagnetic field, plays an interesting role in quantum electrodynamics (QED): it parameterizes the famous anomalous magnetic moment of the electron [1] which has been measured and computed to an extraordinary precision; and from a Wilsonian viewpoint, it corresponds to a perturbatively nonrenormalizable dimension-5 operator and thus has the least possible finite distance to the set of renormalizable operators in QED theory space.

The latter property makes the Pauli term a candidate for a relevant interaction in a coupling regime where nonperturbative interactions set in. In fact, a recent study [2] provides evidence that the observed long-range properties of (pure) QED can be extended to high-energy scales along renormalization group (RG) trajectories that exhibit a sizable Pauli-term contribution. This suggests the existence of an asymptotic-safety scenario that evaded the infamous Landau-pole problem of QED.

This serves as a strong inspiration to study the Pauli term also in $d = 3$, since QED₃ serves as an effective theory for the long-range excitations of various layered condensed-matter systems including graphene and cuprate superconductors. In this context, also the dependence of the renormalization structure of the theory on the number of fermion flavors N_f and the possible existence of a quantum phase transition as a function of N_f is of great interest.

In our work [3], we have studied the renormalization flow of QED upon the inclusion of a Pauli spin-field coupling in general dimensions and flavor numbers, using the

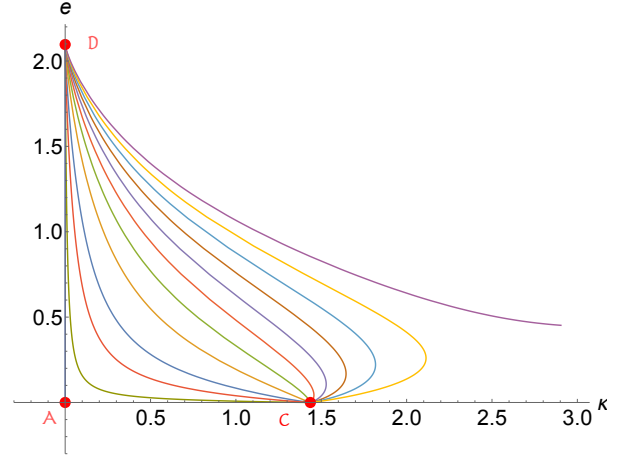


Figure 1: One-parameter family of RG trajectories projected onto the (κ, e) plane for $N_f = 2$ reducible flavor degrees of freedom in $d = 3$ spacetime dimensions. These lead from the fully repulsive UV fixed point C to the IR fixed point D at $\kappa^* = m^* = 0$, thus exhibiting emergent chiral symmetry.

functional RG for a nonperturbative estimate. While the $d = 4$ dimensional case does not extend to higher dimensions and larger flavor number, we observe that it persists for small flavor number in the $d = 3$ dimensional case which is relevant for the layered condensed-matter systems. Most interestingly, we find a UV fixed point C at finite Pauli coupling κ , but zero gauge coupling e , cf. Fig. 1. Among the renormalization group (RG) trajectories that emanate from the fixed point, there are RG flows that cross over to the strong coupling fixed point e^* (D) at zero κ and at vanishing electron mass. This trajectories represent an example of a UV-complete theory that shows an emergent chiral symmetry in the long-range spectrum, the fate of which is ultimately governed by the strong-coupling behavior of QED₃.

This work has been funded by the DFG under 406116891 within RTG 2522/1.

References

- [1] J. S. Schwinger, Phys. Rev. **73**, 416-417 (1948) doi:10.1103/PhysRev.73.416
- [2] H. Gies and J. Ziebell, Eur. Phys. J. C **80**, 607 (2020) doi:10.1140/epjc/s10052-020-8171-8 [arXiv:2005.07586 [hep-th]].
- [3] H. Gies, K. K. K. Tam and J. Ziebell, [arXiv:2210.11927 [hep-th]].

*holger.gies@uni-jena.de

PUBLICATIONS

B. Liu, M. Shi, M. Zepf, B. Lei, and D. Seipt

Accelerating Ions by Crossing Two Ultraintense Lasers in a Near-Critical Relativistically Transparent Plasma

Physical Review Letters **129**, 274801 (2022)

10.1103/PhysRevLett.129.274801

H. Gies, D. Gkiatas, and L. Zambelli

Background effective action with nonlinear massive gauge fixing

Physical Review D **106**, 116013 (2022)

10.1103/PhysRevD.106.116013

B. Baghdasaryan, F. Steinlechner, and S. Fritzsche

Maximizing the validity of the Gaussian approximation for the biphoton state from parametric down-conversion

Physical Review A **106**, 063714 (2022)

10.1103/PhysRevA.106.063714

P. Balla, H. Tuennermann, S. H. Salman, M. Fan, S. Alisauskas, I. Hartl, and C. M. Heyl

Ultrafast serrodyne optical frequency translator

Nature Photonics **17**, 187 (2022)

10.1038/s41566-022-01121-9

K. A. Janulewicz, L. Wegrzynski, T. Fok, A. Bartnik, H. Fiedorowicz, S. Skruszewicz, M. Wünsche, E. Eckner, S. Fuchs, J. Reinhard, J. J. Abel, F. Wiesner, G. G. Paulus, C. Roedel, C. M. Kim, and P. W. Wachulak

Broadband soft X-ray source from a clustered gas target dedicated to high-resolution XCT and X-ray absorption spectroscopy

Optics Express **30**, 47867 (2022)

10.1364/OE.477726

Z. Y. Song, Z. W. Wu, Z. H. Yang, B. L. Zhang, and G. Q. Xiao

Energy-loss enhancement and charge-equilibration time for highly charged xenon ions at near-Bohr velocity in solids

Physical Review A **106**, 062817 (2022)

10.1103/PhysRevA.106.062817

B. Baghdasaryan, C. Sevilla-Gutierrez, F. Steinlechner, and S. Fritzsche

Generalized description of the spatio-temporal biphoton state in spontaneous parametric down-conversion

Physical Review A **106**, 063711 (2022)

10.1103/PhysRevA.106.063711

S. Kühn, C. Cheung, N. S. Oreshkina, R. Steinbruegge, M. Togawa, S. Bernitt, L. Berger, J. Buck, M. Hoesch, J. Seltmann, F. Trinter, C. H. Keitel, M. G. Kozlov, S. G. Porsev, M. F. Gu, F. S. Porter, T. Pfeifer, M. A. Leutenegger, Z. Harman, M. S. Safronova, J. R. C. Lopez-Urrutia, and C. Shah

New Measurement Resolves Key Astrophysical Fe XVII Oscillator Strength Problem

Physical Review Letters **129**, 245001 (2022)

10.1103/PhysRevLett.129.245001

S. Fritzsche

Application of Symmetry-Adapted Atomic Amplitudes

Atoms **10**, 127 (2022)

10.3390/atoms10040127

M. Jolly, S. Voikopoulos, E. Lamour, A. Mery, A. Braeuning-Demian, J.-Y. Chesnel, A. Gumberidze, M. Lestinsky, S. Mace, C. Prigent, J.-M. Ramillon, J. Rangama, P. Rousseau, D. Schury, U. Spillmann, S. Steydli, Th. Stöhlker, M. Trassinelli, and D. Vernhet

Performance of a keV/u Ion Spectrometer for the FISIC Platform

Atoms **10**, 146 (2022)

10.3390/atoms10040146

M. Lestinsky, E. B. Menz, H. Danared, C. Krantz, E. Lindroth, Z. Andelkovic, C. Brandau, A. Braeuning-Demian, S. Fedotova, W. Geithner, F. Herfurth, A. Kalinin, I. Kraus, U. Spillmann, G. Vorobyev, and Th. Stöhlker

First Experiments with CRYRING@ESR

Atoms **10**, 141 (2022)

10.3390/atoms10040141

N. Marsic, W. F. O. Mueller, V. Tympel, Th. Stöhlker, M. Stapelfeld, F. Schmidl, M. Schmelz, V. Zakosarenko, R. Stolz, D. Haider, T. Sieber, M. Schwickert, and H. De Gersem

Influence of Mechanical Deformations on the Performance of a Coaxial Shield for a Cryogenic Current Comparator

Ieee Transactions On Applied Superconductivity **32**, 2500409 (2022)

10.1109/TASC.2022.3206607

R. Steinbruegge, S. Kuehn, F. Nicastro, M. F. Gu, M. Togawa, M. Hoesch, J. Seltmann, I. Sergeev, F. Trinter, S. Bernitt, C. Shah, M. A. Leutenegger, and J. R. C. Lopez-Urrutia

X-Ray Photoabsorption of Density-sensitive Metastable States in Ne vii, Fe xxii, and Fe xxiii

Astrophysical Journal **941**, 188 (2022)

10.3847/1538-4357/ac9c00

S. Strnat, J. Sommerfeldt, V. Yerokhin, W. Middents, Th. Stöhlker, and A. Surzhykov

Circular Polarimetry of Hard X-rays with Rayleigh Scattering

Atoms **10**, 140 (2022)

10.3390/atoms10040140

M. Lenski, T. Heuermann, M. Gebhardt, Z. Wang, C. Gaida, C. Jauregui, and J. Limpert
Inband-pumped, high-power thulium-doped fiber amplifiers for an ultrafast pulsed operation

Optics Express **30**, 44270 (2022)
10.1364/OE.476160

B. Minneker, B. Böning, and S. Fritzsche
Generalized nondipole strong-field approximation of high-order harmonic generation

Physical Review A **106**, 053109 (2022)
10.1103/PhysRevA.106.053109

M. Metternich, H. Nazary, D. Schumacher, C. Brabetz, F. Kroll, F.-E. Brack, M. Ehret, A. Blaze-
vic, U. Schramm, V. Bagnoud, and M. Roth

Analyzing the filamentation of MeV-range proton bunches in a laser-driven ion beamline and optimizing their peak intensity

Physical Review Accelerators And Beams **25**, 111301 (2022)
10.1103/PhysRevAccelBeams.25.111301

P. Pfäfflein, S. Allgeier, S. Bernitt, A. Fleischmann, M. Friedrich, C. Hahn, D. Hengstler, M. O. Herdrich, A. Kalinin, F. M. Kröger, P. Kuntz, M. Lestinsky, B. Loeher, E. B. Menz, T. Over, U. Spillmann, G. Weber, B. Zhu, C. Enss, and Th. Stöhlker

Integration of maXs-type microcalorimeter detectors for high-resolution x-ray spectroscopy into the experimental environment at the CRYRING@ESR electron cooler

Physica Scripta **97**, 114005 (2022)
10.1088/1402-4896/ac93be

D. Schwickert, M. Ruberti, P. Koloenc, A. Przystawik, S. Skruszewicz, M. Sumfleth, M. Braune, L. Bocklage, L. Carretero, M. K. Czwalińska, D. Diaman, S. Duesterer, M. Kuhlmann, S. Palutke, R. Röhlberger, J. Roensch-Schulenburg, S. Toleikis, S. Usenko, J. Viefhaus, A. Vorobiov, M. Martins, D. Kip, V. Averbukh, J. P. Marangos, and T. Laarmann

Charge-induced chemical dynamics in glycine probed with time-resolved Auger electron spectroscopy

Structural Dynamics-us **9**, 064301 (2022)
10.1063/4.0000165

F. Liu, S. Li, Z. Chen, B. Böning, and S. Fritzsche
Nonsequential double ionization of Ne with elliptically polarized laser pulses

Physical Review A **106**, 043120 (2022)
10.1103/PhysRevA.106.043120

R. Weissenbilder, S. Carlstrom, L. Rego, C. Guo, C. M. Heyl, P. Smorenburg, E. Constant, C. L. Arnold, and A. L'Huillier

How to optimize high-order harmonic generation in gases

Nature Reviews Physics **4**, 713 (2022)
10.1038/s42254-022-00522-7

B. Böning and S. Fritzsche

Steering the longitudinal photoelectron momentum in the above-threshold ionization with two not-quite-collinear laser beams

Physical Review A **106**, 043102 (2022)

10.1103/PhysRevA.106.043102

S. Fritzsche and J. Hofbrucker

Biharmonic (ω , 2ω) ionization of atoms by elliptically-polarized light. Carving the photoelectron angular distributions

New Journal Of Physics **24**, 103031 (2022)

10.1088/1367-2630/ac9803

V. Shumakova, V. F. Pecile, J. Fellingner, M. Leskowschek, P. E. C. Aldia, A. S. Mayer, L. W. Perner, S. Salman, M. Fan, P. Balla, S. Schilt, C. M. Heyl, I. Hartl, G. Porat, and O. H. Heckl

Spectrally tunable high-power Yb: fiber chirped-pulse amplifier

Photonics Research **10**, 2309 (2022)

10.1364/PRJ.465883

L. Yue, R. Hollinger, C. B. Uzundal, B. Nebgen, Z. Gan, E. Najafidehaghani, A. George, C. Spielmann, D. Kartashov, A. Turchanin, D. Y. Qiu, M. B. Gaarde, and M. Zuerch

Signatures of Multiband Effects in High-Harmonic Generation in Monolayer MoS₂

Physical Review Letters **129**, 147401 (2022)

10.1103/PhysRevLett.129.147401

L. Hoffmann, S. Jamnuch, C. P. Schwartz, T. Helk, S. L. Raj, H. Mizuno, R. Mincigrucci, L. Foglia, E. Principi, R. J. Saykally, W. S. Drisdell, S. Fatehi, T. A. Pascal, and M. Zuerch

Saturable Absorption of Free-Electron Laser Radiation by Graphite near the Carbon K-Edge

Journal Of Physical Chemistry Letters , 8963 (2022)

10.1021/acs.jpcllett.2c01020

J. j. Abel, F. Wiesner, J. Nathanael, J. Reinhard, M. Wünsche, G. Schmidl, A. Gawlik, U. Huebner, J. Plentz, C. Roedel, G. G. Paulus, and S. Fuchs

Absolute EUV reflectivity measurements using a broadband high-harmonic source and an in situ single exposure reference scheme

Optics Express **30**, 35671 (2022)

10.1364/OE.463216

J. Wang, M. Zepf, Y. Leng, R. Li, and S. G. Rykovanov

Self-torqued harmonics and attosecond pulses driven by time-delayed relativistic vortex lasers

Physical Review A **106**, 033515 (2022)

10.1103/PhysRevA.106.033515

S. Fritzsche and B. Böning

Strong-Field Ionization Amplitudes for Atomic Many-Electron Targets

Atoms **10**, 70 (2022)

10.3390/atoms10030070

- M. A. Valialshchikov, D. Seipt, V. Y. Kharin, and S. G. Rykovanov
Towards high photon density for Compton scattering by spectral chirp
Physical Review A **106**, L031501 (2022)
 10.1103/PhysRevA.106.L031501
- F. Wiesner, S. Skruszewicz, C. Roedel, J. J. Abel, J. Reinhard, M. Wünsche, J. Nathanael, M. Gruenewald, U. Huebner, G. G. Paulus, and S. Fuchs
Characterization of encapsulated graphene layers using extreme ultraviolet coherence tomography
Optics Express **30**, 32267 (2022)
 10.1364/OE.464378
- K. P. Heeg, L. Bocklage, C. Strohm, C. Ott, D. Lentrodt, J. Haber, H.-C. Wille, R. Rueffer, J. Gollwitzer, C. F. Adolff, K. Schlage, I. Sergeev, O. Leupold, G. Meier, C. H. Keitel, R. Röhlsberger, T. Pfeifer, and J. Evers
Reply to: On yoctosecond science
Nature **608**, E18 (2022)
 10.1038/s41586-022-04871-2
- S. Roeder, Y. Zobus, C. Brabetz, and V. Bagnoud
How the laser beam size conditions the temporal contrast in pulse stretchers of chirped-pulse amplification lasers
High Power Laser Science And Engineering **10**, e34 (2022)
 10.1017/hpl.2022.18
- S. Ringleb, M. Kiffer, N. Stallkamp, s. Kumar, J. Hofbrucker, B. Reich, B. Arndt, G. Brenner, M. Ruiz-Lopez, S. Duester, M. Vogel, K. Tiedtke, W. Quint, Th. Stöhlker, and G. G. Paulus
High-intensity laser experiments with highly charged ions in a Penning trap
Physica Scripta **97**, 084002 (2022)
 10.1088/1402-4896/ac7a69
- J. Hofbrucker, S. Ramakrishna, A. V. Volotka, and S. Fritzsche
Polarization effects in the total rate of biharmonic $\omega+3\omega$ ionization of atoms
Physical Review A **106**, 013118 (2022)
 10.1103/PhysRevA.106.013118
- S. Schippers, A. Hamann, A. Perry-Sassmannshausen, T. Buhr, A. Muller, M. Martins, S. Reinwardt, F. Trinter, and S. Fritzsche
Multiple photodetachment of oxygen anions via K-shell excitation and ionization: Direct double-detachment processes and subsequent deexcitation cascades
Physical Review A **106**, 013114 (2022)
 10.1103/PhysRevA.106.013114
- C. Liu, L. Mueller-Botticher, C. Liu, J. Popp, D. Fischer, and D. Cialla-May
Raman-based detection of ciprofloxacin and its degradation in pharmaceutical formulations
Talanta **250**, 123719 (2022)
 10.1016/j.talanta.2022.123719

- P. Gierschke, C. Grebing, M. Abdelaal, M. Lenski, J. Buldt, Z. Wang, T. Heuermann, M. Müller, M. Gebhardt, J. Rothhardt, and J. Limpert
Nonlinear pulse compression to 51-W average power GW-class 35-fs pulses at 2- μ m wavelength in a gas-filled multi-pass cell
Optics Letters **47**, 3511 (2022)
 10.1364/OL.462647
- Y. Hikosaka and S. Fritzsche
Coster-Kronig and super Coster-Kronig transitions from the Xe 4s core-hole state
Physical Chemistry Chemical Physics **24**, 17535 (2022)
 10.1039/d2cp02149h
- S. Fritzsche and B. Böning
Lorentz-force shifts in strong-field ionization with mid-infrared laser fields
Physical Review Research **4**, 033031 (2022)
 10.1103/PhysRevResearch.4.033031
- R. N. Soguel, A. V. Volotka, and S. Fritzsche
QED approach to valence-hole excitation in closed-shell systems
Physical Review A **106**, 012802 (2022)
 10.1103/PhysRevA.106.012802
- Z. Yang, Z. He, G. Xiong, K. Yao, Y. Yang, B. Wei, Y. Zou, Z. Wu, Z. Tian, Y. Ma, C. Wu, X. Gao, and Z. Hu
Apparent change of the 3C/3D line intensity ratio in neonlike ions
Optics Express **30**, 25326458597 (2022)
 10.1364/OE.458597
- E. Escoto, A.-L. Viotti, S. Alisauskas, H. Tunnermann, I. Hartl, and C. M. Heyl
Temporal quality of post-compressed pulses at large compression factors
Journal Of The Optical Society Of America B-optical Physics **39**, 1694 (2022)
 10.1364/JOSAB.453901
- S. Hosseini, A. M. Ilyasu, T. Akilan, A. S. Salama, E. Eftekhari-Zadeh, and K. Hirota
Accurate Flow Regime Classification and Void Fraction Measurement in Two-Phase Flowmeters Using Frequency-Domain Feature Extraction and Neural Networks
Separations **9**, 160 (2022)
 10.3390/separations9070160
- H. Stark, C. Grebing, J. Buldt, A. Klenke, and J. Limpert
Divided-pulse nonlinear compression in a multipass cell
Journal Of Physics-photonics **4**, 035001 (2022)
 10.1088/2515-7647/ac66ab
- D. J. Erb, J. Perlich, S. V. Roth, R. Röhlberger, and K. Schlage
Real-Time Observation of Temperature-Induced Surface Nanofaceting in M-Plane α -Al₂O₃
Acs Applied Materials & Interfaces , (2022)
 10.1021/acsaami.1c22029

- Z. W. Wu, Z. M. He, Z. Q. Tian, C. Z. Dong, and S. Fritzsche
Angular and polarization properties of the Lyman-alpha(1) line $2p(3/2) \rightarrow 1s(1/2)$ following electron-impact excitation of hydrogenlike ions
Physical Review A **105**, 062813 (2022)
 10.1103/PhysRevA.105.062813
- T. Aidukas, L. Loetgering, and A. R. Harvey
Addressing phase-curvature in Fourier ptychography
Optics Express **30**, 22421458657 (2022)
 10.1364/OE.458657
- T. Sailer, V. Debierre, Z. Harman, F. Heisse, C. Konig, J. Morgner, B. Tu, A. V. Volotka, C. H. Keitel, K. Blaum, and S. Sturm
Measurement of the bound-electron g-factor difference in coupled ions
Nature **606**, 479 (2022)
 10.1038/s41586-022-04807-w
- T. Heuermann, Z. Wang, M. Lenski, M. Gebhardt, C. Gaida, M. Abdelaal, J. Buldt, M. Müller, A. Klenke, and J. Limpert
Ultrafast Tm-doped fiber laser system delivering 1.65-mJ, sub-100-fs pulses at a 100-kHz repetition rate
Optics Letters **47**, 3095 (2022)
 10.1364/OL.459385
- D. Schwickert, M. Ruberti, P. Kolorenc, S. Usenko, A. Przystawik, K. Baev, I. Baev, M. Braune, L. Bocklage, M. K. Czwalińska, S. Deinert, S. Duesterer, A. Hans, G. Hartmann, C. Haunhorst, M. Kuhlmann, S. Palutke, R. Röhlberger, J. Roensch-Schulenburg, P. Schmidt, S. Toleikis, J. Viefhaus, M. Martins, A. Knie, D. Kip, V. Averbukh, J. P. Marangos, and T. Laarmann
Electronic quantum coherence in glycine molecules probed with ultrashort x-ray pulses in real time
Science Advances **8**, eabn6848 (2022)
 10.1126/sciadv.abn6848
- E. Eftekhari-Zadeh, A. S. Bensalama, G. H. Roshani, A. S. Salama, C. Spielmann, and A. M. Ilyasu
Enhanced Gamma-Ray Attenuation-Based Detection System Using an Artificial Neural Network
Photonics **9**, 382 (2022)
 10.3390/photonics9060382
- S. Fritzsche
Photon Emission from Hollow Ions Near Surfaces
Atoms **10**, 37 (2022)
 10.3390/atoms10020037
- A. Klenke, C. Jauregui, A. Steinkopff, C. Aleshire, and J. Limpert
High-power multicore fiber laser systems
Progress In Quantum Electronics **84**, 100412 (2022)
 10.1016/j.pquantelec.2022.100412

S. Schippers, S. Stock, T. Buhr, A. Perry-Sassmannshausen, S. Reinwardt, M. Martins, A. Müller, and S. Fritzsche

Near K-edge Photoionization and Photoabsorption of Singly, Doubly, and Triply Charged Silicon Ions

Astrophysical Journal **931**, 100 (2022)

10.3847/1538-4357/ac6874

B. Zhu, A. Gumberidze, T. Over, G. Weber, Z. Andelkovic, A. Braeuning-Demian, R. J. Chen, D. Dmytriiev, O. Forstner, C. Hahn, F. Herfurth, M. O. Herdrich, P.-M. Hillenbrand, A. Kalinin, F. M. Kroger, M. Lestinsky, Y. A. Litvinov, E. B. Menz, W. Middents, T. Morgenroth, N. Petridis, P. Pfafflein, M. S. Sanjari, R. S. Sidhu, U. Spillmann, R. Schuch, S. Schippers, S. Trotsenko, L. Varga, G. Vorobyev, and Th. Stöhlker

X-ray emission associated with radiative recombination for Pb82+ions at threshold energies

Physical Review A **105**, 052804 (2022)

10.1103/PhysRevA.105.052804

A. Steinkopff, C. Aleshire, A. Klenke, C. Jauregui, and J. Limpert

Mitigation of thermally-induced performance limitations in coherently-combined multi-core fiber amplifiers

Optics Express **30**, 16896 (2022)

10.1364/OE.451690

P. Martin, H. Ahmed, D. Doria, A. Alejo, R. Clarke, S. Ferguson, J. Fernandez-Tobias, R. R. Freeman, J. Fuchs, A. Green, J. S. Green, D. Gwynne, F. Hanton, J. Jarrett, D. Jung, K. F. Kakolee, A. G. Krygier, C. L. S. Lewis, A. McIlvenny, P. McKenna, J. T. Morrison, Z. Najmudin, K. Naughton, G. Nersisyan, P. Norreys, M. Notley, M. Roth, J. A. Ruiz, C. Scullion, M. Zepf, S. Zhai, M. Borghesi, and S. Kar

Absolute calibration of Fujifilm BAS-TR image plate response to laser driven protons up to 40 MeV

Review Of Scientific Instruments **93**, 053303 (2022)

10.1063/5.0089402

B. Marx-Glowna, B. Grabiger, R. Löttsch, I. Uschmann, A. T. Schmitt, K. S. Schulze, A. Last, T. Roth, S. Antipov, H.-P. Schlenvoigt, I. Sergueev, O. Leupold, R. Röhlberger, and G. G. Paulus

Scanning high-sensitive x-ray polarization microscopy

New Journal Of Physics **24**, 053051 (2022)

10.1088/1367-2630/ac6e80

W. Eschen, L. Loetgering, V. Schuster, R. Klas, A. Kirsche, L. Berthold, M. Steinert, T. Pertsch, H. Gross, M. Krause, J. Limpert, and J. Rothhardt

Material-specific high-resolution table-top extreme ultraviolet microscopy

Light-science & Applications **11**, 117 (2022)

10.1038/s41377-022-00797-6

J. B. Ohland, U. Eisenbarth, B. Zielbauer, Y. Zobus, D. Posor, J. Hornung, D. Reemts, and V. Bagnoud

Ultra-compact post-compressor on-shot wavefront measurement for beam correction at PHELIX

High Power Laser Science And Engineering **10**, e18 (2022)

10.1017/hpl.2022.9

A. de Beurs, L. Loetgering, M. Herczog, M. Du, K. S. E. Eikema, and S. Witte

aPIE: an angle calibration algorithm for reflection ptychography

Optics Letters **47**, 1949 (2022)

10.1364/OL.453655

C. Aleshire, A. Steinkopff, A. Klenke, C. Jauregui, S. Kühn, J. Nold, N. Haarlammert, T. Schreiber, and J. Limpert

High-energy Q-switched 16-core tapered rod-type fiber laser system

Optics Letters **47**, 1725 (2022)

10.1364/OL.454287

K. S. Schulze, B. Grabiger, R. Löttsch, B. Marx-Glowna, A. T. Schmitt, A. L. Garcia, W. Hippler, L. Huang, F. Karbstein, Z. Konopkova, H.-P. Schlenvoigt, J.-P. Schwinkendorf, C. Strohm, T. Toncian, I. Uschmann, H.-C. Wille, U. Zastrau, R. Röhlsberger, Th. Stöhlker, T. E. Cowan, and G. G. Paulus

Towards perfectly linearly polarized x-rays

Physical Review Research **4**, 013220 (2022)

10.1103/PhysRevResearch.4.013220

S. Haedrich, E. Shestaev, M. Tschernajew, F. Stutzki, N. Walther, F. Just, M. Kienel, I. Seres, P. Jojart, Z. Bengery, B. Gilicze, Z. Varallyay, A. Borzsonyi, M. Müller, C. Grebing, A. Klenke, D. Hoff, G. G. Paulus, T. Eidam, and J. Limpert

Carrier-envelope phase stable few-cycle laser system delivering more than 100 W, 1 mJ, sub-2-cycle pulses

Optics Letters **47**, 1537 (2022)

10.1364/OL.450991

S. Ramakrishna, J. Hofbrucker, and S. Fritzsche

Photoexcitation of atoms by cylindrically polarized Laguerre-Gaussian beams

Physical Review A **105**, 033103 (2022)

10.1103/PhysRevA.105.033103

V. P. Kosheleva, A. V. Volotka, D. A. Glazov, D. V. Zinenko, and S. Fritzsche

g Factor of Lithiumlike Silicon and Calcium: Resolving the Disagreement between Theory and Experiment

Physical Review Letters **128**, 103001 (2022)

10.1103/PhysRevLett.128.103001

M. Zimmer, S. Scheuren, A. Kleinschmidt, N. Mitura, A. Tebartz, G. Schaumann, T. Abel, T. Ebert, M. Hesse, S. Zaechter, S. C. Vogel, O. Merle, R.-J. Ahlers, S. D. Pinto, M. Peschke, T. Kroell, V. Bagnoud, C. Roedel, and M. Roth

Demonstration of non-destructive and isotope-sensitive material analysis using a short-pulsed laser-driven epi-thermal neutron source

Nature Communications **13**, 1173 (2022)

10.1038/s41467-022-28756-0

S. Fritzsche

Level Structure and Properties of Open f-Shell Elements

Atoms **10**, 7 (2022)

10.3390/atoms10010007

J. Stierhof, S. Kuehn, M. Winter, P. Micke, R. Steinbruegge, C. Shah, N. Hell, M. Bissinger, M. Hirsch, R. Ballhausen, M. Lang, C. Graefe, S. Wipf, R. Cumbee, G. L. Betancourt-Martinez, S. Park, J. Niskanen, M. Chung, F. S. Porter, Th. Stöhlker, T. Pfeifer, G. V. Brown, S. Bernitt, P. Hansmann, J. Wilms, J. R. Crespo Lopez-Urrutia, and M. A. Leutenegger

A new benchmark of soft X-ray transition energies of Ne, CO₂, and SF₆: paving a pathway towards ppm accuracy (vol 76, pg 1, 2022)

European Physical Journal D **76**, 52 (2022)

10.1140/epjd/s10053-022-00379-6

J. Stierhof, S. Kuehn, M. Winter, P. Micke, R. Steinbruegge, C. Shah, N. Hell, M. Bissinger, M. Hirsch, R. Ballhausen, M. Lang, C. Graefe, S. Wipf, R. Cumbee, G. L. Betancourt-Martinez, S. Park, J. Niskanen, M. Chung, F. S. Porter, Th. Stöhlker, T. Pfeifer, G. V. Brown, S. Bernitt, P. Hansmann, J. Wilms, J. R. C. Lopez-Urrutia, and M. A. Leutenegger

A new benchmark of soft X-ray transition energies of Ne, CO₂, and SF₆: paving a pathway towards ppm accuracy

European Physical Journal D **76**, 38 (2022)

10.1140/epjd/s10053-022-00355-0

U. T. Sanli, T. Messer, M. Weigand, L. Lotgering, G. Schutz, M. Wegener, C. Kern, and K. Keskinbora

High-Resolution Kinoform X-Ray Optics Printed via 405 nm 3D Laser Lithography

Advanced Materials Technologies **7**, 2101695 (2022)

10.1002/admt.202101695

A.-L. Viotti, M. Seidel, E. Escoto, S. Rajhans, W. P. Leemans, I. Hartl, and C. M. Heyl

Multi-pass cells for post-compression of ultrashort laser pulses

Optica **9**, 197 (2022)

10.1364/OPTICA.449225

C. Mahnke, Y. Hua, Y. Ma, S. Salman, T. Lamb, S. Schulz, C. M. Heyl, H. Cankaya, and I. Hartl

Long-term stable, synchronizable, low-noise picosecond Ho: fiber NALM oscillator for Ho:YLF amplifier seeding

Optics Letters **47**, 822 (2022)

10.1364/OL.447353

P.-M. Hillenbrand, S. Hagmann, Y. S. Kozhedub, E. P. Benis, C. Brandau, R. J. Chen, D. Dmytriiev, O. Forstner, J. Glorius, R. E. Grisenti, A. Gumberidze, M. Lestinsky, Y. A. Litvinov, E. B. Menz, T. Morgenroth, S. Nanos, N. Petridis, P. Pfäfflein, H. Rothard, M. S. Sanjari, R. S. Sidhu, U. Spillmann, S. Trotsenko, I. I. Tupitsyn, L. Varga, and Th. Stöhlker

Single and double K-shell vacancy production in slow Xe-54+,Xe-53+-Xe collisions

Physical Review A **105**, 022810 (2022)

10.1103/PhysRevA.105.022810

A. Volotka, D. Samoilenko, S. Fritzsche, V. G. Serbo, and A. Surzhykov

Polarization of Photons Scattered by Ultra-Relativistic Ion Beams

Annalen Der Physik **534**, 2100252 (2022)

10.1002/andp.202100252

L. Doyle, P. Khademi, P. Hilz, A. Saevert, G. Schaefer, J. Schreiber, and M. Zepf

Experimental estimates of the photon background in a potential light-by-light scattering study

New Journal Of Physics **24**, 025003 (2022)

10.1088/1367-2630/ac4ad3

J. Fan, J. Hofbrucker, A. V. Volotka, and S. Fritzsche

Relativistic calculations of two-color two-photon K-shell ionization

European Physical Journal D **76**, 18 (2022)

10.1140/epjd/s10053-021-00334-x

S. Fuchs, J. J. Abel, J. Nathanael, J. Reinhard, F. Wiesner, M. Wünsche, S. Skruszewicz, C. Roedel, D. Born, H. Schmidt, and G. G. Paulus

Photon counting of extreme ultraviolet high harmonics using a superconducting nanowire single-photon detector

Applied Physics B-lasers And Optics **128**, 26 (2022)

10.1007/s00340-022-07754-6

S. Keppler, N. Elkina, G. A. Becker, J. Hein, M. Hornung, M. Mausezahl, C. Rödel, I. Tamer, M. Zepf, and M. C. Kaluza

Intensity scaling limitations of laser-driven proton acceleration in the TNSA-regime

Physical Review Research **4**, 013065 (2022)

10.1103/PhysRevResearch.4.013065

L. Loetgering, S. Witte, and J. Rothhardt

Advances in laboratory-scale ptychography using high harmonic sources [Invited]

Optics Express **30**, 4133 (2022)

10.1364/OE.443622

M. Seidel, F. Pressacco, O. Akcaalan, T. Binhammer, J. Darvill, N. Ekanayake, M. Frede, U. Grosse-Wortmann, M. Heber, C. M. Heyl, D. Kutnyakhov, C. Li, C. Mohr, J. Mueller, O. Puncken, H. Redlin, N. Schirmel, S. Schulz, A. Swiderski, H. Tavakol, H. Tuennermann, C. Vidoli, L. Wenthaus, N. Wind, L. Winkelmann, B. Manschwetus, and I. Hartl

Ultrafast MHz-Rate Burst-Mode Pump-Probe Laser for the FLASH FEL Facility Based on Nonlinear Compression of ps-Level Pulses from an Yb-Amplifier Chain

Laser & Photonics Reviews **16**, 2100268 (2022)

10.1002/lpor.202100268

A. Klenke, A. Steinkopff, C. Aleshire, C. Jauregui, S. Kühn, J. Nold, C. Hupel, S. Hein, S. Schulze, N. Haarlammert, T. Schreiber, A. Tuennermann, and J. Limpert

500 W rod-type 4 x 4 multicore ultrafast fiber laser

Optics Letters **47**, 345 (2022)

10.1364/OL.445302

F. Karbstein

Large N external-field quantum electrodynamics

Journal Of High Energy Physics , 057 (2022)

10.1007/JHEP01(2022)057

P. Palmeri, J. Deprince, M. A. Bautista, S. Fritzsche, J. A. Garcia, T. R. Kallman, C. Mendoza, and P. Quinet

Plasma environment effects on K lines of astrophysical interest

Astronomy & Astrophysics **657**, A61 (2022)

10.1051/0004-6361/202141550

C. Wu, L. Li, M. Yeung, S. Wu, S. Cousens, S. Tietze, B. Dromey, C. Zhou, S. Ruan, and M. Zepf

Proposal for complete characterization of attosecond pulses from relativistic plasmas

Optics Express **30**, 389444043 (2022)

10.1364/OE.444043

E. Eftekhari-Zadeh, M. S. Bluemcke, Z. Samsonova, R. Löttsch, I. Uschmann, M. Zapf, C. Ronning, O. N. Rosmej, D. Kartashov, and C. Spielmann

Laser energy absorption and x-ray generation in nanowire arrays irradiated by relativistically intense ultra-high contrast femtosecond laser pulses

Physics Of Plasmas **29**, 013301 (2022)

10.1063/5.0064364

C. M. Heyl, M. Seidel, E. Escoto, A. Schoenberg, S. Carlstroem, G. Arisholm, T. Lang, and I. Hartl

High-energy bow tie multi-pass cells for nonlinear spectral broadening applications

Journal Of Physics-photonics **4**, 014002 (2022)

10.1088/2515-7647/ac483a

F. C. Salgado, N. Cavanagh, M. Tamburini, D. W. Storey, R. Beyer, P. H. Bucksbaum, Z. Chen, A. Di Piazza, E. Gerstmayr, H. Harsh, E. Isele, A. R. Junghans, C. H. Keitel, S. Kuschel, C. F. Nielsen, D. A. Reis, C. Roedel, G. Sarri, A. Seidel, C. Schneider, U. I. Uggerhoj, J. Wulff, V. Yakimenko, C. Zepf, S. Meuren, and M. Zepf

Single particle detection system for strong-field QED experiments

New Journal Of Physics **24**, 015002 (2022)

10.1088/1367-2630/ac4283

L. Stoyanov, G. Maleshkov, I. Stefanov, G. G. Paulus, and A. Dreischuh

Focal beam structuring by triple mixing of optical vortex lattices

Optical And Quantum Electronics **54**, 34 (2022)

10.1007/s11082-021-03399-5

W. Middents, G. Weber, U. Spillmann, T. Krings, M. Vockert, A. Volotka, A. Surzhykov, and Th. Stöhlker

Possible Polarization Measurements in Elastic Scattering at the Gamma Factory Utilizing a 2D Sensitive Strip Detector as Dedicated Compton Polarimeter

Annalen Der Physik **534**, 2100285 (2022)

10.1002/andp.202100285

N. Dimitrov, M. Zhekova, Y. Zhang, G. G. Paulus, and A. Dreischuh

Background-free femtosecond autocorrelation in collinearly-aligned inverted field geometry using optical vortices

Optics Communications **504**, 127493 (2022)

10.1016/j.optcom.2021.127493

F. M. Kröger, G. Weber, S. Hirlaender, R. Alemany-Fernandez, M. W. Krasny, Th. Stöhlker, I. Y. Tolstikhina, and V. P. Shevelko

Charge-State Distributions of Highly Charged Lead Ions at Relativistic Collision Energies

Annalen Der Physik **534**, 2100245 (2022)

10.1002/andp.202100245

F. Karbstein

Vacuum Birefringence at the Gamma Factory

Annalen Der Physik **534**, 2100137 (2022)

10.1002/andp.202100137

THESES

L. Klar

Quantum vacuum nonlinearities in the all-optical regime

Dissertation

Friedrich-Schiller-Universität Jena; Physikalisch-Astronomische Fakultät, (2022).

V. Kosheleva

QED corrections to the hyperfine splitting and g factor of few-electron ions

Dissertation

Friedrich-Schiller-Universität Jena; Physikalisch-Astronomische Fakultät, (2022).

M. Schwab

Relativistic electron-cyclotron resonances in laser Wakefield acceleration

Dissertation

Friedrich-Schiller-Universität Jena; Physikalisch-Astronomische Fakultät, (2022).

M. Vockert

Die radiative Elektroneneinfang als Quelle stark linear polarisierter Röntgenstrahlung

Dissertation

Friedrich-Schiller-Universität Jena; Physikalisch-Astronomische Fakultät, (2022).

M. Gebhardt

Power scaling of few-cycle short-wavelength infrared laser sources for nonlinear frequency conversion

Dissertation

Friedrich-Schiller-Universität Jena; Physikalisch-Astronomische Fakultät, (2022).